2011

Modeling and Control of Wind Generation and Its HVDC Delivery System

Haiping Yin
University of South Florida, hyin@mail.usf.edu

Modeling and Control of Wind Generation and Its HVDC Delivery System

by

Haiping Yin

A dissertation submitted in partial fulfillment
of the requirements for the degree of
Doctor of Philosophy
Department of Electrical Engineering
College of Engineering
University of South Florida

Major Professor: Lingling Fan, Ph.D.
Kenneth Buckle, Ph.D.
Sanjukta Bhanja, Ph.D.
Yicheng Tu, Ph.D.
Fangxing Li, Ph.D.

Date of Approval:
August 28, 2011

Keywords: DFIG, LCC, Active Power, Power Routing, Reactive Power

DEDICATION

To my husband, my parents, my brother, my friends and my teachers.

ACKNOWLEDGEMENTS

There are many people I would like to express my gratitude to during the dissertation work. It is a pleasure to thank those who made this dissertation possible.

First of all, my deep and sincere gratitude to my advisor Dr. Lingling Fan for her patience, assistance, supervision and support. It is a great honor to have been her first Ph.D. student. She has helped in numerous ways. The door of her office was always open whenever I had problems about the research. I could not have finished my dissertation without her technical advice and guidance. She taught me innumerable lessons and insights on the academic research.

Secondly, I thank the rest of my committee members: Dr. Kenneth Buckle, Dr. Sanjukta Bhanja, Dr. Yicheng Tu and Dr. Fangxing Li, for their encouragement, insightful comments, and hard questions. My sincere thanks also go to Dr. Sanjukta Bhanja for her time and insightful questions during my proposal to Ph.D. candidacy. I also owe my most sincere gratitude to Dr. Zhixin Miao for his valuable help.

Many thanks also to my colleagues from the smart grid power system lab: Yasser Wehbe, Ling Xu, Lakanshan Prageeth Piyasinghe for the stimulating discussions, for the help and all the fun we have together.

Last but not the least, I would like to thank my husband, Yangwei Cai, my parents, Jianhua Yin, Guifang Cao and my brother, Haibo Yin for their love and encouragement.

TABLE OF CONTENTS

LIST OF TABLES

LIST OF FIGURES

ABSTRACT

As the most developed renewable energy source, wind energy attracts the most research attentions. Wind energy is easily captured far away from the places where wind energy is used. Because of this unique characteristic of the wind, the generation and delivery systems of the wind energy need to be well controlled. The objective of this dissertation work is modeling and control of wind generation and its High Voltage Direct-Current (HVDC) delivery system.

First of all, modeling of the Doubly-fed Induction Generator (DFIG)-based wind farm is presented including dynamic models of the wind turbine, shaft system and DFIG. Detailed models of the rectifier and inverter of HVDC are given as well. Furthermore, a control scheme for rotor-side converter (RSC) and grid-side converter (GSC) is studied. A control method for the HVDC delivery system is also presented.

Secondly, wind farms are prone to faults due to the remote locations. Unbalanced fault is the most frequent. Therefore, fault-ride through (FRT) of an ac connected DFIG-based wind farm is discussed in this dissertation. Dynamic responses of the wind farm under unbalanced grid conditions are analyzed including rotor current harmonics, torque pulsation and dc-link voltage ripples. Coordinated control strategy is proposed for DFIG under unbalanced fault.

Thirdly, when a wind farm is connected to remote ac grids through HVDC, active power balance between DFIG-based wind farm and HVDC delivery needs to be obtained. In other words, the power delivered through HVDC should balance the varying wind power extracted from the wind farm. Therefore, control methods of DFIG and HVDC are modified. A coordinated control scheme is proposed to keep the power balance. The transmitted power through HVDC is regulated by adjusting the firing angle of the converter under dif-

ferent wind speeds. Both average and detailed models of the wind farm and HVDC delivery are built in Matlab/Simulink and Matlab/SimPowerSystems. Case studies validate the effectiveness of the proposed control method.

Fourthly, the fast power routing capability of line-commutated converter (LCC)-HVDC is investigated when the wind energy is delivered through LCC-HVDC transmission. Such capability is most desired in future grids with high penetration of wind energy. The proposed technology replaces the traditional LCC-HVDC rectifier power order control by an ac voltage order control. This technology enables the HVDC rectifier ac bus to act as an infinite bus and absorb fluctuating wind power. A study system consisting of an ac system, an LCC-HVDC, and a doubly-fed induction generator (DFIG) based wind farm is built in Matlab/SimPowersystems. Simulation experiments are carried out to demonstrate the proposed HVDC rectifier control in routing fluctuating wind power and load change. Parameters of the proposed voltage order control are also investigated to show their impact on HVDC power routing and ac fault recovery.

Finally, for the wind farm with LCC-HVDC delivery, reactive power needs to be provided for the HVDC. Hence, reactive power capability of the DFIG is discussed because DFIG is capable of providing reactive power to the LCC-HVDC. Since the reactive power is directly related to the voltage, the upper and lower limits of the rectifier ac bus voltage are investigated. Case studies are carried out in Matlab/Simulink to verify the system dynamics when the ac bus voltage is within and out of the limits.

CHAPTER 1

INTRODUCTION

1.1 Background

To date, the most electrical power is generated from fossil fuel. This causes adverse environmental effects: global warming due to CO_2 emission. The environmental issues and possible energy crisis contribute to the interest in clean and renewable energy resources such as solar, wind, tidal, etc. Among the various renewable energy resources, wind energy is the most attractive. By 2012, up to 12% of world's electricity will be supplied by wind power [3]. In the United States, 40,180 MW of wind power had been installed across the country by December 31, 2010 [4]. The newest "20% Wind Energy by 2030" report, published by the U.S. Department of Energy in 2008, analyzes the feasibility of generating 20% of the nation's electricity from wind power by 2030 [5].

With the high penetration of wind energy in power systems, suitable sites need to be found for wind generation plants. Studies [6, 7] show that offshore sites have higher and more stable potential wind capabilities compared with onshore ones. Furthermore, complaints from residents due to the aesthetics disruption and noise pollution are also factors that develop the offshore wind farms. Currently, the largest operational offshore wind farm in the world is Thanet in the United Kingdom, with capability of 300MW [8]. As for the United States, a report "A National Offshore Wind Strategy: Creating an Offshore Wind Energy Industry in the United States" was unveiled by the U.S Department of Energy on February 7, 2011. This plan will accelerate the development of offshore wind farm projects in the United States.

The current state-of-the-art wind generation technology is doubly-fed induction generator (DFIG). A DFIG is an induction machine, with both the stator and the rotor connected to electrical sources. The stator of a DFIG is directly connected to the grid, while the rotor is connected to the grid through back-to-back voltage source converters: rotor-side converter (RSC) and grid-side converter (GSC). The two converters are coupled with a dc-link capacitor. Compared with other wind turbine generator configuration, a DFIG-based wind farm offers noticeable advantages: it can achieve variable speed and constant frequency [9].

Wind farms are required to ride through abnormal grid voltage conditions [10]. Due to its asymmetric configuration, DFIGs suffer adverse impact due to grid unbalance [11, 12]. Unbalanced faults will cause unbalanced current, and torque pulsations [11]. Consequently, oscillations of the stator power will be produced. Moreover, ripples of the dc-link voltage will result in the power oscillations of the power of both RSC and GSC, which causes damage to the dc capacitor between RSC and GSC.

For DFIG-based large offshore wind farms, one key challenge is the transmission of bulk power over long distances. Two alternative transmission methods are available for connecting offshore wind farms to the grid: high-voltage alternating current (HVAC) and high-voltage direct current (HVDC) [13, 14]. Detailed comparison of ac and dc transmission is discussed in [15] considering the transmission costs, technical issues, and reliability. Compared with traditional HVAC, HVDC offers many advantages as follows [13, 16, 15].

1. Power flow is fully defined and controlled.
2. The frequencies of the ac systems at the sending and receiving ends are independent.
3. Cable power losses are lower.
4. Costs are lower for long distance bulk power transmission.

In the application of wind energy transmission, the main disadvantage of HVAC is that the load loss increases significantly with increasing wind farm capability and the distance to load. Generally, HVAC is suitable for medium wind farms with transmission distance less

than 100-150 km [13]. Alternatively, HVDC connection is more preferable for large wind farms with longer transmission lines.

There are two types of HVDC connection methods: voltage source converter (VSC)-HVDC using IGBTs and line-commutated converter (LCC)-HVDC using thyristors. References [17, 18] addressed research in VSC-HVDC. VSC-HVDC is self-commutating, and it does not require an external voltage source. Reactive power can be independently controlled at each ac network, but its power rating is limited within 500MW. Furthermore, the main drawback of VSC-HVDC is the higher losses due to fast switching operations. On the other hand, LCC-HVDC can handle higher power capability compared with VSC-HVDC, and the power losses are lower. However, LCC-HVDC needs a strong grid to ensure normal commutation process. Reactive power absorption is another key issue because the current always lags behind the voltage due to delayed firing angle. Both LCC-HVDC and VSC-HVDC are studied in [13]. For wind farms with bulk power and long transmission distance, LCC-HVDC is preferable. Hence, this dissertation investigates the issues related with LCC-HVDC.

1.2 Problem Identification

This dissertation focuses on the control of wind generation and its HVDC delivery system. The following challenges are studied.

First, wind farms are often located in remote areas. Rural grids are weak and unstable, and prone to faults. National grid codes impose requirements on wind farms for fault-ride through (FRT) capability in order to prevent their disconnection during network faults. In practice, most faults in power system are unbalanced faults. Hence, control of wind farm under unbalanced grid conditions is studied in this dissertation.

Second, for wind energy with HVDC delivery system, active power balance is the key factor to ensure the normal operation of the system. In other words, the active power generated by the wind farm should balance the power taken by LCC-HVDC, local loads and

losses. As the wind speed is ever-changing, the generated electrical power from DFIGs also fluctuates. The corresponding dc power output from the rectifier should follow the change of the electrical power from wind generation to achieve power balance. Any imbalance will cause stress on the wind turbine. Then large fluctuations will be observed in the rotor speed and electromagnetic torque. Therefore, active power balance needs to be studied in the DFIG-based wind generation system with LCC-HVDC connection. Normally, power order control is adopted in the rectifier of LCC-HVDC. However, the power order is always changing due to the fluctuating wind speeds. There will be some delay in the communication links which send the remote power order signal. On the other hand, LCC-HVDC is fast in power routing. Therefore, the traditional power order control is not suitable here. The ac bus voltage order is selected to achieve the fast power routing capability of LCC-HVDC.

Third, a main drawback of the LCC-HVDC is reactive power consumption. For wind farms with LCC-HVDC delivery systems, reactive power must be provided for the HVDC converters to ensure normal operation since the voltage always lags behind the current. Usually, synchronous static compensator (STATCOM) is placed on the point of common coupling (PCC) to provide the reactive power demand of the LCC-HVDC. For variable speed DFIG-based wind farm with back-to-back pulse width modulation (PWM) converters, both the stator and the GSC have the capability of providing reactive power. Hence, a STATCOM may not be necessary. However, when the wind speed increases, the capability to provide reactive power by a DFIG-based wind farm decreases. Meanwhile, there is an increase in reactive power loss in the transformer and ac lines. As a consequence, the reactive power transmitted to the LCC-HVDC could be reduced. Hence, coordination of the DFIG wind farm terminal voltage and HVDC rectifier voltage is necessary to make sure the required reactive power is supplied to the HVDC converters.

1.3 Tasks

The main tasks carried out in this dissertation are as follows:

Task 1 presents the modeling of DFIG-based wind farm and its HVDC delivery system. As for the wind farm, aerodynamic modeling of the wind turbine, dynamic modeling of the DFIG are presented. For the HVDC, detailed model of the converter and ac filters are given. Existing control schemes for RSC and GSC are discussed. Detailed PI controller design procedure is presented. Control parts of the HVDC are also described.

Task 2 studies the FRT of direct connected DFIG-based wind farm. Dynamics of the DFIG are analyzed under unbalanced grid conditions. A novel control technique is proposed for both RSC and GSC. Through simulation studies in Matlab/Simlink, the proposed control method shows higher performance compared with the existing dual-sequence control scheme.

Task 3 studies the active power balance between the wind farm and its HVDC delivery. Since the harvested wind power is always changing due to the varying wind speed, the delivered power through HVDC should be able to track the wind power to keep power balance. Coordinated control strategy of the wind farm and HVDC delivery is proposed for the rectifier of the HVDC. The firing angle of the thyristor is adjusted to change the power extracted from the wind farm, while the frequency and bus voltage is kept constant.

Task 4 investigates the fast power routing capability of HVDC. LCC-HVDC is the power electronic device-based technology which is widely used in wind power transmission. It can route the power order from the wind farm very fast. The well-known power order control could be an obstacle in the power routing of HVDC, because of the delay in process of the power order computation and sending. Therefore, the ac bus voltage order is proposed to achieve the fast power routing capability of LCC-HVDC. The system dynamics are studied under wind speed change and the load change. Furthermore, the ac fault recovery capability of the system is also investigated with the proposed control strategy.

Task 5 analyzes the reactive power coordination of DFIG-based wind farm with LCC-HVDC delivery. Reactive power absorption is a key issue in the wind farm system with

LCC-HVDC delivery, since the voltage of each phasor lags behind the current. Besides the traditional ac filters, DFIG could also provide reactive power to HVDC. Hence, the active/reactive power limits of DFIG should be identified. In addition, the limiting range of the bus voltage is also investigated to ensure normal operation of the system under different wind speeds.

1.4 Approach

Both average and detailed models of the wind farm with its HVDC delivery are studied in this dissertation. Matlab/Simlink and Matlab/SimPowerSystems are adopted for average and detailed models respectively.

Here, Simulink is an environment for time-domain simulation of dynamic systems. The blocks in the library offer advantages for control design. However, the dynamic models are average models based on math equations. All the variables are dc components as all the ac variables in abc reference frame are transferred into *qd* reference frame. Therefore, the high frequency components are ignored. For the DFIG-based wind farm with HVDC delivery, power electronic devices are the key components. Details of the converters cannot be presented in Simulink. Hence, Matlab/SimPowerSystems is also used. Matlab/SimPowerSystems is a toolbox developed by MathWorks especially for modeling and simulating electrical power systems. It provides most of the electrical components commonly used in power systems, such as machines, electrical sources, power electronics, etc. In the distributed resource library, there are blocks for wind generation, which is a good resource for this research. Detailed models of DFIG-based wind farm with HVDC delivery are more easily built in Matlab/SimPowerSystems. All the necessary components are addressed in the model, including transformers, ac filters, pulse generators. Furthermore, the dynamic responses of the detailed converters model are all captured. That is why Matlab/SimPowerSystems is adopted in this research work.

1.5 Outline of the Dissertation

The structure of the dissertation is organized as follows:

Chapter 1 gives a brief introduction of the studied issues including background information, problem identification, tasks, and approach adopted in this dissertation.

Chapter 2 presents a detailed literature survey on wind generators and their delivery systems. The development of wind turbines is reviewed, especially, DFIG-base wind turbine is described. Due to the rural location of wind farms, the FRT of an ac connected DFIG-based wind farm is also addressed. On the other hand, for the delivery system, the configurations of both VSC-HVDC and LCC-HVDC are presented. Also their advantages and disadvantages are compared in detail. Moreover, two key issues, active power balance and reactive power coordination, are investigated in the delivery system.

Chapter 3 studies the modeling of wind generator system and LCC-HVDC delivery including the the aerodynamic modeling of wind turbine, dynamic modeling of the DFIG, modeling of the converters and the ac filters in HVDC.

Chapter 4 discusses the control of wind generator system and LCC-HVDC delivery. Vector control is adopted in the DFIG control. For both the RSC and GSC, PI controllers are used for the outer and inner control loops. Hence, typical parameter design procedure of the PI controller is also given. Furthermore, control of the converters of HVDC is described.

Chapter 5 presents the FRT of DFIG-based wind farm under unbalanced grid conditions. When there is unbalanced fault on the grid, the root cause of the high frequency harmonics in rotor currents, the electromagnetic torque and the dc-link voltage are discussed. A simple control technique for limiting the harmonics of the dc-link voltage and the electromagnetic torque is proposed. Simulation results for a 2MW DFIG in Matlab/Simulink confirms the effectiveness of the proposed control technique.

Chapter 6 studies the active power balance between DFIG-based wind farm and its delivery system. Due to ever-changing characteristics of the wind, the captured wind power through the wind turbine always varies. The delivered power through HVDC should

balance the ac power to obtain normal operation of the system. A coordination control scheme is proposed for the rectifier to adjust the firing angle at different wind speeds. Case studies in Matlab/Simlink and Matlab/SimPowerSystems are also given to show the effectiveness of the proposed control method.

Chapter 7 investigates the fast power routing capability of HVDC in wind energy transmission. Due to the intermittent characteristics of wind, the traditional power order control of the rectifier is not suitable. Voltage control is proposed for the rectifier, therefore the HVDC rectifier ac bus acts as an infinite bus. Simulation studies are carried out in Matlab/SimPowersystems to demonstrate the proposed control in routing fluctuating wind power and load change.

Chapter 8 presents the reactive power coordination between a DFIG-based wind farm and LCC-HVDC. To obtain reactive power coordination, first the DFIG should work within its operating limit while supplying reactive power for LCC-HVDC, a lower limit of the ac bus voltage is identified. In addition, as wind speed increases and in order to ensure reactive power provision from DFIG to LCC-HVDC, the ac bus voltage also has an upper limit. Case studies of an aggregated 200MW wind farm with LCC-HVDC connection is tested in Matlab/Simulink. Simulation results under different ac bus voltages verify the analysis.

Chapter 9 summarizes the main conclusions of this dissertation and provides some suggestions for the future work.

CHAPTER 2

LITERATURE SURVEY OF WIND GENERATORS AND DELIVERY SYSTEMS

2.1 Wind Energy Systems

Wind has become a prominent renewable energy supplier. The development of wind turbines is one of the key drivers. The dominate wind turbines are classified according to their ability of speed control as: fixed-speed wind turbine or variable speed wind turbine.

Wind turbines are built based on the "Danish concept" [9]: a fixed-speed wind turbine using squirrel-cage induction machine (SCIG) is directly connected to a three-phase power grid as shown in Fig. 2.1. The capacitor bank provides reactive power for the SCIG. The soft-starter is used for smoother grid connection. However, fixed-speed wind turbines have many disadvantages: first, the varying wind speed will cause fluctuations in mechanical power which is converted to fluctuating electrical power. Hence, sturdy mechanical design is required in case of wind gusts. Second, the reactive power cannot be controlled [19].

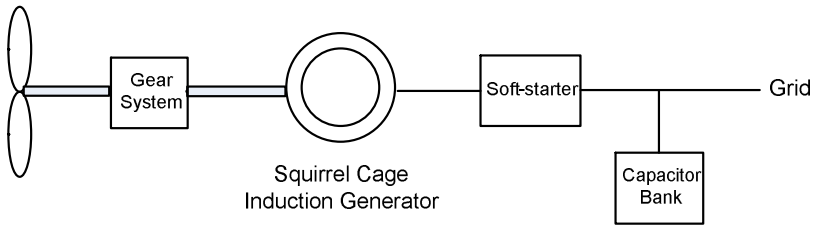

Figure 2.1. Fixed-speed wind generator topology.

There are three types of variable speed wind turbines configurations: limited variable speed using wound rotor induction generators as shown in Fig. 2.2, variable wind speed wind turbine using doubly-fed induction generators as shown in Fig. 2.3 and variable speed

wind turbine based on permanent magnet synchronous generators (PMSG) as shown in Fig. 2.4. The first type of configuration achieves limited variable speed control through the additional rotor resistance; the rotor resistance can be changed to control the slip and in turn the output power. DFIG-based configuration is widely used in current wind turbine systems. The back-to-back converters with partial rating are connected to the rotor circuit and the grid. Both active and reactive power could be controlled through the converters. Details of a DFIG will be introduced in Chapter 3. In the third type, PMSG is connected to a full-scale converter then to the grid. A gearbox may not be necessary in this kind of configuration. Instead, a direct driven generator with a larger diameter is used [20].

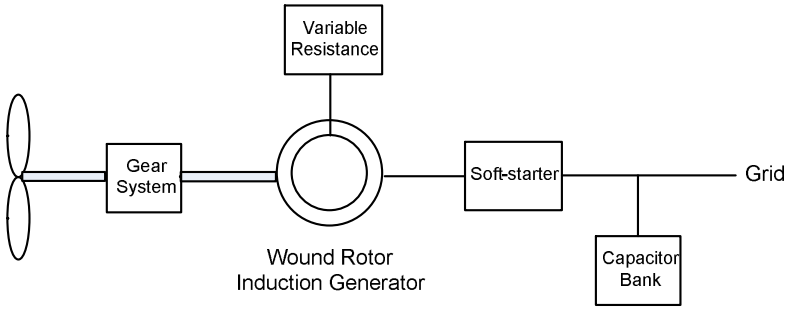

Figure 2.2. Limited variable speed wind turbine topology.

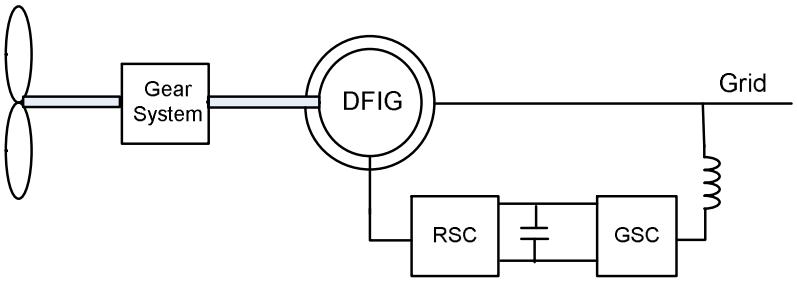

Figure 2.3. DFIG-based wind generator topology.

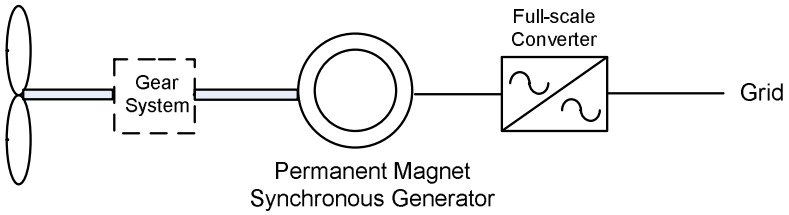

Figure 2.4. Variable wind generator topology with a full scale converter.

2.1.1 Doubly-Fed Induction Generator

Currently, DFIG-based wind generation as shown in Fig. 2.3 is the state-of-the-art wind generator technology [21, 22]. The stator windings of a DFIG are connected directly to the grid while the rotor windings are connected to back-to-back converters with 25%-30% of the generator rating. The stator provides active power to the grid. The power flow direction in the rotor depends on the operation condition. In sub-synchronous operation, the power is fed into the rotor; in super-synchronous operation, the power flows out of the rotor and fed to the grid through the converters. DFIGs offer many advantages [9, 23, 24] including variable speed operation, decoupled active power/reactive power control, maximum wind power capture, etc. Studies in [25, 26] focus on modeling of DFIG-based wind turbines and their impacts on the power systems. In [25], the power converters are modeled as controlled voltage sources to regulate the rotor currents. The model performance is verified in power system simulation tool PSS/E. [26] derives a dynamic model of a DFIG, which is suitable for transient stability study. Vector control is usually adopted for the converter control of DFIG. The active and reactive power could be controlled independently through the RSC. While the GSC keeps the dc-link voltage and supplies reactive power to the grid to keep the terminal voltage in desired range [21, 22, 27, 28].

2.1.2 Fault-Ride Through of an AC-Connected DFIG-Based Wind Farm

For wind farms in remote rural areas, the grid voltage is vulnerable to disturbances. Among the power system disturbances, asymmetric faults are more frequent than sym-

metric faults. To obtain continuous operation of the wind generation system, fault-ride through (FRT) capability needs to be studied during unbalanced grid voltage. Unbalanced grid conditions in DFIGs give rise to high frequency components in rotor currents and torque, which can cause excessive shaft stress and winding losses [29]. Existing control techniques in literature designed to minimize the torque pulsations include (i) RSC compensation by supplying negative sequence voltages to the rotor circuits [30, 31] to suppress the negative sequence components in the rotor currents and ripples in the electromagnetic torque, (ii) GSC compensation by compensating negative sequence currents to the grid [32] to keep the stator currents free of negative sequence components and thus eliminate the negative sequence components in the rotor currents.

Dual control schemes for both the RSC and GSC are proposed in [33, 10, 34, 12] to suppress the dc-link voltage ripples, pulsations in the rotor currents and electromagnetic torque. Negative sequence compensation has been adopted in the above mentioned references. Negative sequence compensation can be realized through current control loops [32, 35, 33, 10, 12] or through direct power control [36, 37]. The cascaded control structure with inner fast current control and outer slower power/voltage control is widely used in converter control and is also used in the commercial DFIG technology [38]. Hence, this control structure is widely adopted in the existing research.

2.2 Wind Energy Delivery Systems

2.2.1 Comparison of AC and DC Delivery

Electrical power could be transmitted through both ac and dc. DC is especially used for very long distance bulk power transmission. For wind energy transmission, dc is more attractive because of the following advantages compared with ac transmission [39]:

1. Lower losses

   The ac resistance of a conductor is higher than dc resistance because of skin effect. Furthermore, there is reactive power consumption in ac transmission system. There-

fore, to transmit the same amount of real power, the power loss in ac lines is much higher than in dc lines.

2. Lower cost

   Typical investment costs for an overhead line transmission with ac and dc is shown in Fig. 2.5 [1]. From Fig. 2.5, there is a break-even-distance at about 600-800 km [1]. For transmission lines above this value, ac cost is less than dc because of the high investment in terminal stations of dc. However, for transmission lines with a length above this level, the cost of dc will be less than ac. For undersea cables, the break-even-distance is much smaller, at about 50km [1]. For offshore wind farms using undersea cables, dc is a wise choice over ac.

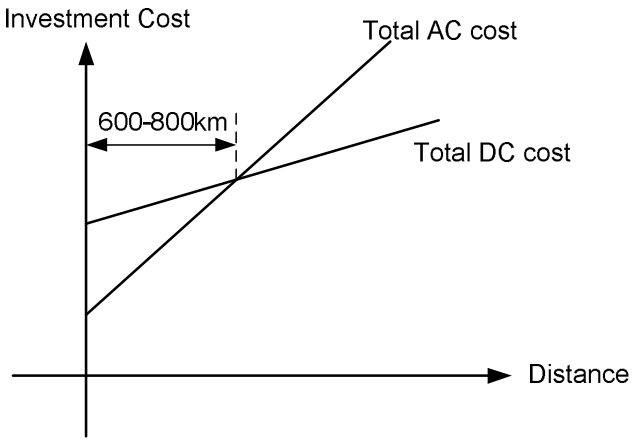

Figure 2.5. Typical investment cost for an ac line and a dc line [1].

3. Better grid connection

   Different areas of the world have different network frequencies. For example, Japan has both 50 Hz and 60 Hz networks. In North America, the power grid is divided into three unsynchronized parts. In such case, HVDC is suitable for connecting unsynchronized ac networks.

2.2.2 HVDC Technology

With the development of the wind energy industry, the majority of wind farms are built in rural areas around the world, requiring long transmission lines to the grid. HVDC delivery has been verified to be more attractive than ac transmission [40, 39] in the connection of offshore wind farms. As introduced in Chapter 1, there are two HVDC connection types: VSC-HVDC using IGBTs, and LCC-HVDC using thyristors.

2.2.2.1 VSC-HVDC

The configuration of a VSC-HVDC consists of two VSC units and a dc-link as shown in Fig. 2.6. The dc capacitors at both ends of the dc line maintain a stable voltage at the converter ends. The current main three topologies for VSC transmission are two-level topology, multilevel diode-clamped topology, and multilevel floating-capacitor topology. They are compared in terms of cost, dc capacitor size and commutation inductance in [41]. An overview of VSC-HVDC is also presented in [42]. VSC-HVDC technology remains competitive in wind energy delivery due to its valuable advantages such as independent control of active and reactive power, no external voltage source for commutation, and fast dynamic response. When VSC-HVDC is used for DFIG-based wind farms, the wind farm side VSC collects the wind energy from the wind farm, while the grid side VSC transmits the collected energy to onshore grid. As an indication of power balance, the dc-voltage is kept constant through wind farm side VSC control [17]. VSCs are able to operate with weak ac grids through independent control of active and reactive power [40]. VSC-HVDC is more feasible for weak ac systems with short circuit ratio (SCR) less than 2.5 since commutation voltage is not needed. Hence, VSC-HVDC is suitable for connecting wind farms to weak ac grids [43]. Interconnection of two weak ac systems through VSC-HVDC is discussed in [44], where a novel power synchronization control is proposed.

The power rating of VSC-HVDC is restricted to about 500MW [13] due to the limit of IGBTs. For large wind energy delivery, VSC-HVDC is less competitive compared with

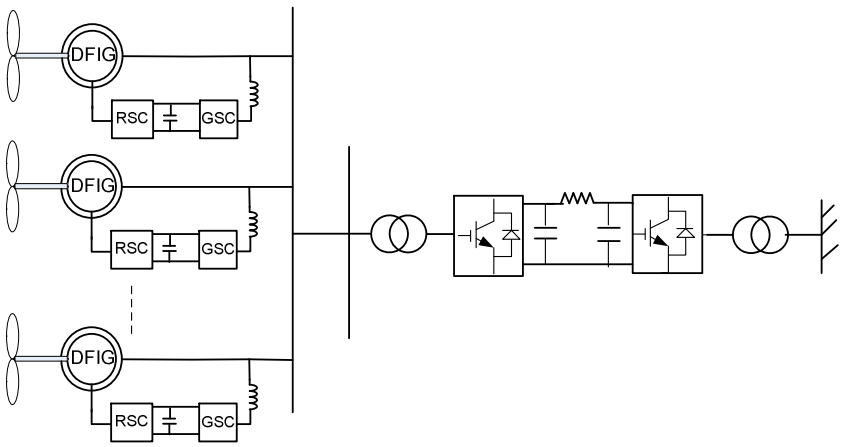

Figure 2.6. Configuration of a DFIG-based wind farm with VSC-HVDC delivery.

LCC-HVDC. On the other hand, the power loss of VSC-HVDC is higher due to the higher frequency switching used for PWM.

2.2.2.2 LCC-HVDC

A single-line schematic diagram of LCC-HVDC for wind farm transmission is illustrated in Fig. 2.7. It includes two valve groups, three-phase two-winding converter transformers, dc cables and ac filters at each end.

For LCC-HVDC, the line-commutated converters cause characteristic harmonic voltages and currents. Hence, ac filters are required at the two ends. The orders of these harmonics depends on the pulse number of the converter configuration. For p-pulse converter, the generated voltage/current harmonics orders will be pk$\pm$1, where k is an integer. For 12-pulse converter, the ac filters are designed typically for 11th and 13th harmonics. Usually, besides the single tuned filters, a high-pass filter branch is also included in the ac filters, and extra shunt capacitors are also needed to provide reactive power. Details of ac filter design for HVDC systems are introduced in [45]. [46] gives the parameters algorithm of ac filters in HVDC transmission systems. C-type filter is specifically presented in [47, 48].

Due to the firing angle and commutation angle of thyristors, the converter voltage in each phase always lags behind its current, hence reactive power supply needs to be guaranteed. Besides ac filters, static synchronous compensator (STATCOM) is another provider of reactive power. When LCC-HVDC is used to deliver wind energy from DFIG-based wind generation, reactive power compensation could also be provided by DFIG through flexible reactive power control of DFIG.

Despite the above mentioned drawbacks, LCC-HVDC is still the preferred option for bulk-power and long-distance dc transmission. First of all, the capability of LCC-HVDC is larger than VSC-HVDC. Secondly, the power loss is lower for long-distance delivery compared with VSC-HVDC.

Extensive literature has been published in research on LCC-HVDC applications in wind energy system. For DFIG-based wind generation systems with LCC-HVDC transmission, coordinated control of HVDC-link and DFIG has been proposed in [49]. Stator flux reference value is provided for DFIG control, and the firing angle of the rectifier at the sending end of HVDC-link is used to regulate the frequency of the local ac system.

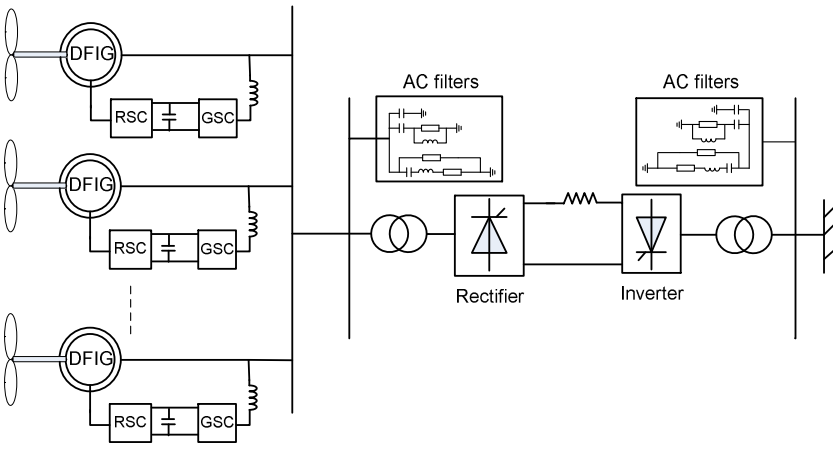

Figure 2.7. Configuration of a DFIG-based wind farm with LCC-HVDC delivery.

In [16, 14], LCC-HVDC system without STATCOM is studied for DFIG-based wind farm system connection. Grid frequency control is used to regulate the HVDC rectifier firing angle/dc-link current, and hence to control the power flow in the system. Tradi-

tionally, LCC-HVDC needs commutation voltage supplied by synchronous compensators. STATCOM is widely used to provide the commutation voltage instead of synchronous compensators because of its lower cost. STATCOM issues in offshore wind farm with LCC-HVDC connection are discussed in [50] in details. With STATCOM, the offshore could be controlled as an infinite source to obtain higher system dynamics. Recently, hybrid HVDC system was proposed by [51]. The hybrid system consists of a thyristor-based rectifier, and a STATCOM with PWM inverter.

2.3 Active Power Balance between Wind Farm and HVDC Delivery System

When a wind farm is connected to a grid through LCC-HVDC, the generated electrical power from the wind farm must balance the active power taken by LCC-HVDC and the dissipation. Any imbalance will cause voltage/frequency variations of the local ac grid[49]. The transmitted power of the HVDC should be able to track the varying power due to different wind speeds. Frequency control is proposed in [49] to adjust the firing angle of the rectifier of HVDC transmission without STATCOM. If the wind speed increases, the decreased firing angle will cause the dc current to increase. Thus more power is delivered through HVDC to keep the power balance.

For the LCC-HVDC transmission system with STATCOM converter, any power imbalance will accumulate on the dc capacitor of the STATCOM, causing the dc-link voltage to fluctuate [50]. Hence, the dc voltage of STATOM could be considered as the indication of power imbalance, which is used to change the dc current order of HVDC converter [13]. Once the dc voltage of STATCOM is kept constant, power balance could be achieved.

2.4 Reactive Power Coordination of Wind Farm with LCC-HVDC Delivery

Newly-established grid codes require wind turbines to have reactive power capability to support grid voltage [52]. On the other hand, as mentioned in the above section, LCC-HVDC needs reactive power because the voltage lags the current in each phase. The general reactive power source for LCC-HVDC is a capacitor bank and STATCOM. When

a DFIG-based wind farm is connected to LCC-HVDC, the stator of DFIG could also provide reactive power to LCC-HVDC, since DFIG can achieve independent active/reactive power control through rotor excitation current. Furthermore, the GSC could also produce reactive power under weak grid conditions. Hence, the reactive power capability of DFIG needs to be investigated considering the DFIG-based wind farm with LCC-HVDC connection. If the reactive power supply from DFIG and shunt capacitor satisfy the LCC-HVDC requirements, STATCOM may not be necessary, thus the cost could be greatly reduced.

The reactive power capability of the wind turbine depends on grid connection type. For DFIG-based wind turbine, the total power fed into the grid is supplied from the stator and GSC. [52, 53, 54] have done some research on the reactive power capability of DFIG. Considering the stator current, rotor current and rotor voltage limits, the actual active and reactive power capability limits could be obtained. [53] concludes that the main factor in limiting the reactive power production is the rotor current; Additional limiting factors such as system losses, speed variation, and filter are considered in [54] to get a more accurate reactive power capability. For the offshore wind farm with HVDC connection[55], the total DFIG-based wind turbine capability limits are obtained considering stator current limit, rotor current limit and steady-state stability limit. Taking into account the total capability limits and steady-state stability limits, the maximum reactive power limit depends on rectifier voltage and the generated active power while the minimum reactive power lies on the rectifier voltage.

2.5 Other Related Study on Wind Farm with HVDC Delivery

Small signal analysis is a useful method for power system analysis, it provides valuable information about the dynamic characteristics for controller design [2]. Some work based on small signal analysis has been done in wind farms with HVDC systems. Dynamic analysis of the rectifier subsystem is presented in [51]. Through the eigenvalue analysis method, the ac current dynamic of the rectifier is investigated and double loop control scheme is designed. [56] also applies small signal analysis to an offshore wind farm with

line-commutated HVDC link. Eigenvalue analysis is performed to design a PID rectifier-current regulator, which is also verified in improving damping of the offshore wind farm.

CHAPTER 3

MODELING OF WIND GENERATION SYSTEM AND LCC-HVDC DELIVERY

This chapter gives the modeling details of the wind energy generation system with LCC-HVDC delivery. The topology of the studied system is shown in Fig. 3.1. Modeling of each part will be introduced in subsequent sections of this chapter.

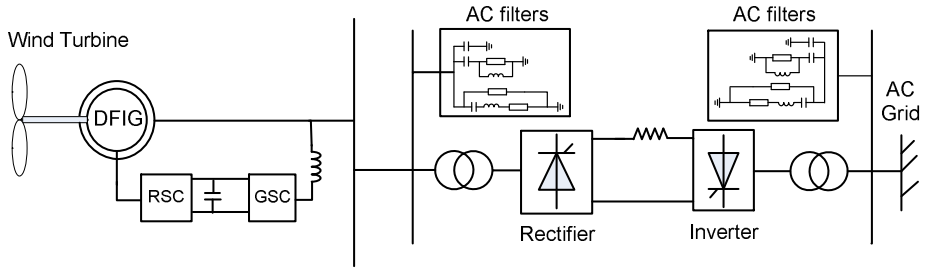

Figure 3.1. System topology.

3.1 DFIG-Based Wind Turbine

3.1.1 Aerodynamic Modeling of Wind Turbine

The wind turbine is an important mechanical device in the wind power generation system. The total wind power swept by the rotor blade of the wind turbine can be expressed as:

$$P_{wind} = \frac{\rho}{2}\pi R^2 V_\omega^3 \tag{3.1}$$

where ρ is the air density, R is the rotor radius of wind turbine, and V_ω is wind speed. The mechanical power of the wind turbine is only part of the total wind power, since it

is impossible to exact all the kinetic energy of the wind. This refers to a term: power coefficient defined as C_p. Hence, the mechanical power is given by:

$$P_m = C_p P_{wind} \tag{3.2}$$

The power coefficient C_p is a nonlinear function of the blade pitch angle θ, and the tip speed ratio λ as:

$$C_p = (0.44 - 0.0167\theta)sin(\frac{\pi(\lambda - 3)}{15 - 0.3\theta}) - 0.00184(\lambda - 3)\theta \tag{3.3}$$

where the tip speed ratio λ is:

$$\lambda = \frac{\omega_m R}{V_\omega} \tag{3.4}$$

where ω_m is the mechanical angular velocity. For the old simple wind turbine, the blade pitch angle is constant. With a fixed pitch angle θ, the relationship between power coefficient C_p and tip speed ratio λ is similar as the curve shown in Fig. 3.2. At the optimal point λ_{opt}, maximum power coefficient C_p is achieved. Assuming a constant wind speed V_ω, the tip speed ratio λ is proportional to mechanical angular velocity ω_m. Thus, the curves of C_p against ω_m are in the similar shape as shown in Fig. 3.2 under different wind speeds but their optimal operation points are different. In the case of variable-speed wind turbine, the maximum power coefficient C_p is achieved through adjusting the rotational speed of the wind turbine. Thereby, the maximum output mechanical power point is reached.

When the wind speed is above rated speed, which means the wind power exceeds the generator rating, pitch angle control is considered a common way to regulate the aerodynamic torque. In such condition, the mechanical power is reduced to the rating (1 pu) through adjusting the pitch angle. When the wind speed is less than the rated speed, the pitch angle is adjusted to the minimum value to get the maximum mechanical power. In both cases, the pitch angle controller senses the speed change to regulate the output power. A typical structure of pitch angle controller is shown in Fig. 3.3. The pitch angle

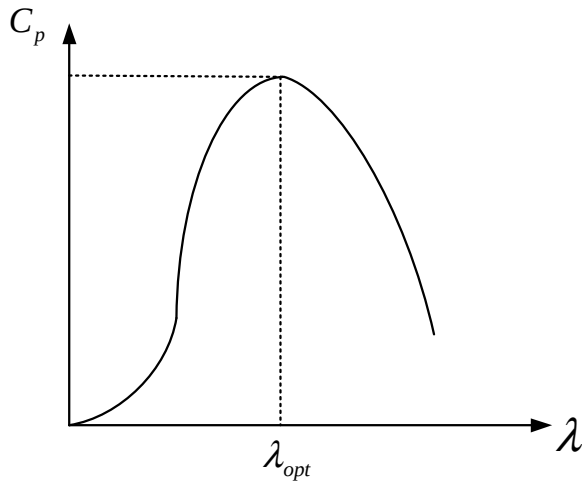

Figure 3.2. Power coefficient curve.

is determined by the input variables: rotor speed, generator power. The actual rotor speed is compared with its reference value, and the error is sent to the PI controller to get the reference value of the pitch angle. On the other hand, the error of the generator power signal is also input into the PI controller to generate the reference pitch angle.

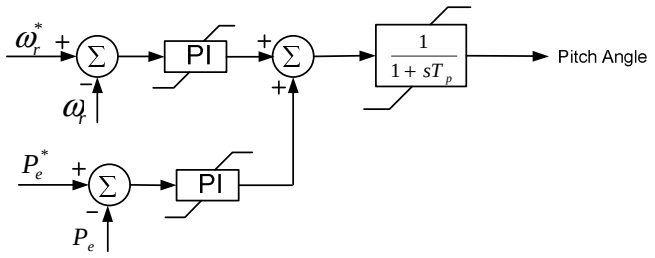

Figure 3.3. Wind turbine pitch angle controller.

The two-mass shaft model is proved sufficient for the stability analysis of DFIG-based wind generation in [57]. The schematic representation of a two-mass shaft is depicted in Fig. 3.4. The two-mass shaft model is described by the following equations:

$$\frac{d\omega_t}{dt} = -\frac{D_t + D_{tg}}{2H_t}\omega_t + \frac{D_{tg}}{2H_t}\omega_r - \frac{1}{2H_t}T_{tg} + \frac{T_m}{2H_t} \tag{3.5}$$

$$\frac{d\omega_r}{dt} = \frac{D_{tg}}{2H_g}\omega_t - \frac{D_t + D_{tg}}{2H_g}\omega_r + \frac{1}{2H_g}T_{tg} + \frac{T_e}{2H_g} \tag{3.6}$$

$$\frac{dT_{tg}}{dt} = K_{tg}\omega_0\omega_t - K_{tg}\omega_0\omega_r \tag{3.7}$$

where D_t and D_g are the damping coefficients of the turbine and generator, D_{tg} is the damping coefficient of the flexible coupling between the two masses, H_t and H_g are the inertia constants for the turbine and the generator, K_{tg} is the shaft stiffness.

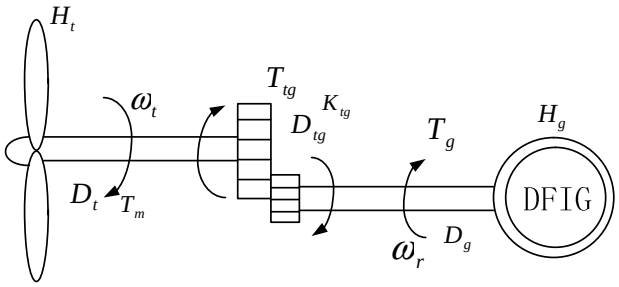

Figure 3.4. Schematic diagram of the shaft.

3.1.2 Dynamic Modeling of the DFIG

The dynamic of the DFIG is expressed through a series differential equations in stationary abc reference frame. All the variables of the equations such as voltage, current, and flux linkage are time-varying variables, which make the computation process complex. In the late 1920s, R. H. Park introduced an approach to reduce the complexity of electrical machine analysis: Park's transformation [58]. In the Park's transformation, the stator variables are transferred to a reference frame rotating at the synchronous speed. The detailed transformation is expressed as:

$$f_{qd0s} = K_s f_{abcs}, \tag{3.8}$$

where

$$(f_{qd0s})^T = \begin{bmatrix} f_{qs} & f_{ds} & f_{0s} \end{bmatrix}, \tag{3.9}$$

$$(f_{abcs})^T = \begin{bmatrix} f_{as} & f_{bs} & f_{cs} \end{bmatrix}, \tag{3.10}$$

$$K_s = \frac{2}{3} \begin{bmatrix} \cos(\theta) & \cos(\theta - \frac{2\pi}{3}) & \cos(\theta + \frac{2\pi}{3}) \\ \sin(\theta) & \sin(\theta - \frac{2\pi}{3}) & \sin(\theta + \frac{2\pi}{3}) \\ \frac{1}{2} & \frac{1}{2} & \frac{1}{2} \end{bmatrix}, \tag{3.11}$$

$$\omega = \frac{d\theta}{dt}. \tag{3.12}$$

In the above equations, f could either be voltage, current or flux linkage. The relationship between the *abc* stationary reference frame and *qd* rotating reference frame can be seen in Fig. 3.5. Fig. 3.6 shows the equivalent circuit of DFIG in *qd* reference frame. The stator

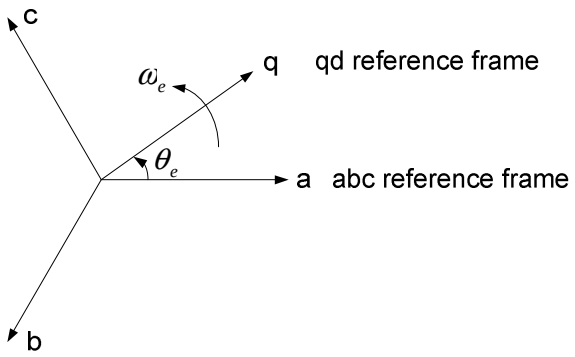

Figure 3.5. Reference frame relationship.

voltage and rotor voltage equations in *qd* reference frame can be obtained as follows:

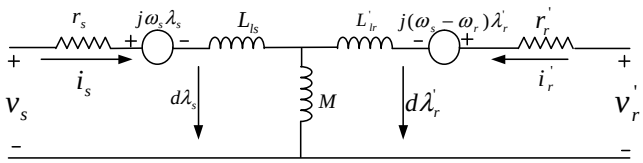

Figure 3.6. The equivalent circuit of DFIG.

$$\begin{bmatrix} v_{qs} \\ v_{ds} \\ v_{0s} \\ v'_{qr} \\ v'_{dr} \\ v'_{0r} \end{bmatrix} = \begin{bmatrix} r_s & 0 & 0 & 0 & 0 & 0 \\ 0 & r_s & 0 & 0 & 0 & 0 \\ 0 & 0 & r_s & 0 & 0 & 0 \\ 0 & 0 & 0 & r'_r & 0 & 0 \\ 0 & 0 & 0 & 0 & r'_r & 0 \\ 0 & 0 & 0 & 0 & 0 & r'_r \end{bmatrix} \begin{bmatrix} i_{qs} \\ i_{ds} \\ i_{0s} \\ i'_{qr} \\ i'_{dr} \\ i'_{0r} \end{bmatrix} + \begin{bmatrix} 0 & \omega & 0 & 0 & 0 & 0 \\ -\omega & 0 & 0 & 0 & 0 & 0 \\ 0 & 0 & 0 & 0 & 0 & 0 \\ 0 & 0 & 0 & 0 & \omega-\omega_r & 0 \\ 0 & 0 & 0 & \omega-\omega_r & 0 & 0 \\ 0 & 0 & 0 & 0 & 0 & 0 \end{bmatrix} \begin{bmatrix} \lambda_{qs} \\ \lambda_{ds} \\ \lambda_{0s} \\ \lambda'_{qr} \\ \lambda'_{dr} \\ \lambda'_{0r} \end{bmatrix} + \begin{bmatrix} \dot{\lambda}_{qs} \\ \dot{\lambda}_{ds} \\ \dot{\lambda}_{0s} \\ \dot{\lambda}'_{qr} \\ \dot{\lambda}'_{dr} \\ \dot{\lambda}'_{0r} \end{bmatrix} \tag{3.13}$$

where v_{qs}, v_{ds} are the q-axis and d-axis stator voltages, v_{qr}, v_{dr} are the q-axis and d-axis rotor voltages, r_s is the stator resistance, r'_r is the rotor resistance, L_{ls} is the stator self inductance, L'_{lr} is the rotor self inductance, M is the mutual inductive reactance, ω is the synchronous rotating speed, and ω_r is the rotor rotating speed. The air-gap flux linkages

are expressed as:

$$\begin{bmatrix} \lambda_{qs} \\ \lambda_{ds} \\ \lambda_{0s} \\ \lambda'_{qr} \\ \lambda'_{dr} \\ \lambda'_{0r} \end{bmatrix} = \begin{bmatrix} L_{ls}+M & 0 & 0 & M & 0 & 0 \\ 0 & L_{ls}+M & 0 & 0 & M & 0 \\ 0 & 0 & L_{ls} & 0 & 0 & 0 \\ M & 0 & 0 & L'_{lr}+M & 0 & 0 \\ 0 & M & 0 & 0 & L'_{lr}+M & 0 \\ 0 & 0 & 0 & 0 & 0 & L'_{lr} \end{bmatrix} \begin{bmatrix} i_{qs} \\ i_{ds} \\ i_{0s} \\ i'_{qr} \\ i'_{dr} \\ i'_{0r} \end{bmatrix} \tag{3.14}$$

In addition, the electromagnetic torque can be described as:

$$T_e = \frac{2}{3}\frac{p}{2}(\lambda_{ds} i_{qs} - \lambda_{qs} i_{ds}) \tag{3.15}$$

where p is the number of poles.

The stator active power fed into the grid can be calculated through the following equation:

$$P_s = v_{qs} i_{qs} + v_{ds} i_{ds} \tag{3.16}$$

While the reactive power that the stator absorbs or feeds into the grid is calculated:

$$Q_s = v_{qs} i_{ds} - v_{ds} i_{qs} \tag{3.17}$$

For GSC, the equivalent circuit in qd reference frame can be obtained from Fig. 3.7, and the grid side voltage is shown as follows:

$$v_g = v_s - \omega_s L_{tg} \frac{di_g}{dt} - j\omega_s L_{tg} i_g \tag{3.18}$$

The voltage and current relationship in qd-axis can be written as:

$$v_{qg} = v_{qs} - \omega_s L_{tg} \frac{di_{qg}}{dt} - \omega_s L_{tg} i_{dg} \tag{3.19}$$

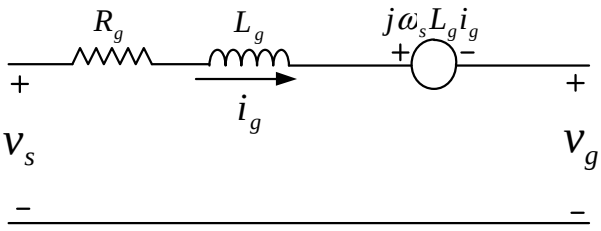

Figure 3.7. The equivalent circuit of GSC.

$$v_{dg} = v_{ds} - \omega_s L_{tg} \frac{di_{dg}}{dt} + \omega_s L_{tg} i_{qg} \tag{3.20}$$

The dynamics of the dc-link between RSC and GSC can be expressed as follows:

$$CV_{dc} \frac{dV_{dc}}{dt} = P_g - P_r = \frac{1}{2}(v_{qg} i_{qg} + v_{dg} i_{dg} - (v_{qr} i_{qr} + v_{dr} i_{dr})) \tag{3.21}$$

where P_g is the active power of the GSC, P_r is the active power of the RSC.

The model of DFIG-based wind farm in Matlab/SimPowerSystems is shown in Fig. 3.8. The dynamics of the wind turbine and drive train are considered. Pitch angle control is also given. Since in *qd* reference frame, the variables are dc signals and hence easier to control. Consequently, all the variables in abc reference frame are transformed into *qd* reference frame. Vector control is adopted for the RSC and GSC, and the required synchronization angle is derived through phasor-locked loop (PLL).

3.2 LCC-HVDC

3.2.1 Rectifier

A typical rectifier model in Matlab/SimPowerSystems is shown in Fig. 3.9. The rectifier is a three-phase, full-wave bridge circuit as shown in Fig. 3.10. The cathodes of valves 1, 3 and 5 are connected together. For the upper row, the valve with the most positive phase-to-neutral voltage conducts. For the lower row, the anodes of valves 2, 4 and 6 are connected together. Therefore, the valve with the most negative phase-to-neutral voltage

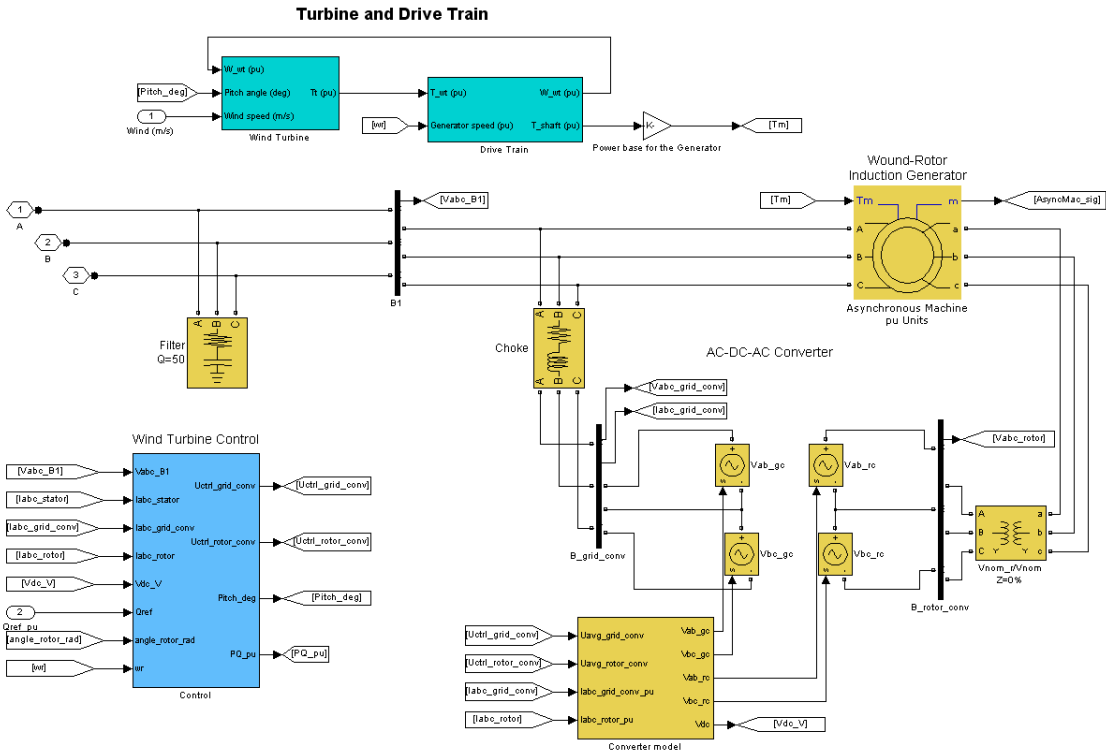

Figure 3.8. DFIG-based wind farm model in Matlab/SimPowerSystems.

conducts. The waveforms of the voltage are illustrated in Fig. 3.11. When ωt is between 0^0 and 60^0, v_{an} is the highest positive phase, v_{bn} is the lowest negative phase. Hence, valve 1 of the upper row and valve 6 of the lower row conduct. For the next 60^0, valve 1 and 2 conduct. Then valve 3 and 2 conduct. From the analysis, it is easy to find that each valve conducts for 120^0. The instantaneous direct voltage is composed of several 60^0 segments. Therefore, the average direct voltage V_{d0} can be calculated by the integration of the instantaneous dc voltage over any 60^0 period as follows:

$$\begin{aligned} V_{d0} &= \frac{3}{\pi}\int_0^{60^0} v_{ab}\, d(\omega t) \\ &= \frac{3}{\pi}\int_0^{60^0} \sqrt{2}V_{ac}\sin(\omega t + 60^0)\, d(\omega t) \\ &= \frac{3\sqrt{6}}{\pi}V_{ac} \end{aligned}$$

where V_{ac} is the rms line-to-neutral voltage. V_{d0} is the "ideal no-load direct voltage."

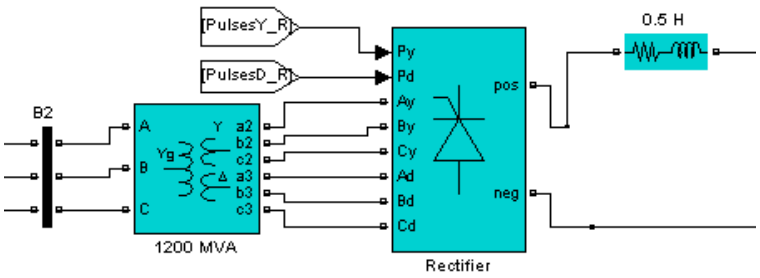

Figure 3.9. Schematic diagram of the rectifier in Matlab/SimPowerSystems.

A simplified rectifier equivalent circuit is shown in Fig. 3.12. For a monopole, 12-pulse rectifier of HVDC-link, considering the firing angle delay and commutation angle, the relationship between the dc and ac voltage is [2]:

$$V_{dr} = V_{d0}\cos\alpha - 2R_{rec}I_{dc} \tag{3.22}$$

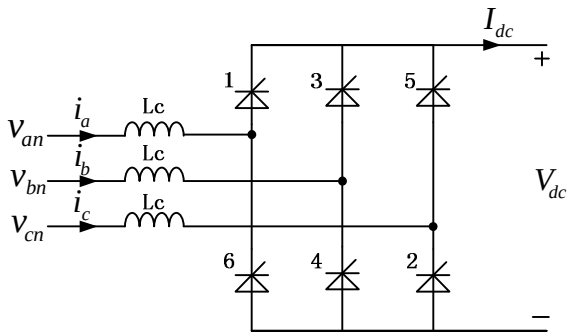

Figure 3.10. Three-phase full-wave bridge rectifier.

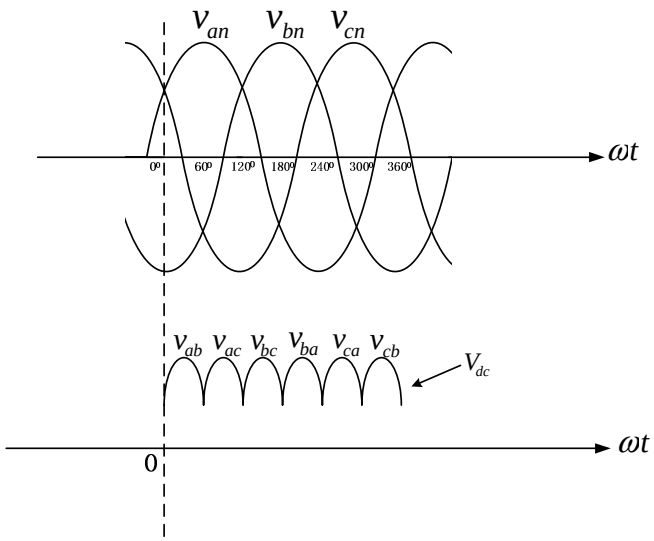

Figure 3.11. Voltage waveforms of the three-phase full-wave bridge rectifier.

where $R_{rec} = \frac{3}{\pi} X_c$ is the commutating reactance per phase, V_{dr} and I_{dc} are the dc voltage and dc current, α is the firing delay angle of the rectifier and is in the range of $0^0 - 90^0$.

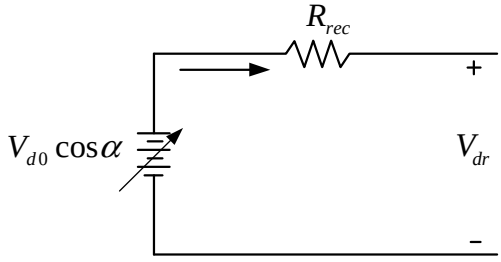

Figure 3.12. The equivalent circuit of the rectifier.

The power relationship is expressed as:

$$P_{dc} = V_{dr} I_{dc} = P_{ac} \tag{3.23}$$

$$Q_{ac} = P_{ac} \tan(\theta) \tag{3.24}$$

where P_{dc} is the dc power, P_{ac} and Q_{ac} are the active and reactive power, θ is the power factor.

3.2.2 Inverter

The inverter operation is similar to the rectifier, the only difference is that the firing angle is in the range of 90^0 and 180^0. Normally β, called the ignition advance angle, is used to describe inverter performance. An inverter model in Matlab/SimPowerSystems is shown in Fig. 3.13 and its equivalent circuit is shown in Fig. 3.14.

The relationship between the ac and dc quantities are as follows:

$$\begin{cases} V_{di} = V_{d0} cos\beta + R_{inv} I_{dc} \\ V_{d0} = \frac{3}{\pi}\sqrt{2} B T V_{ac(L-L)} \end{cases} \tag{3.25}$$

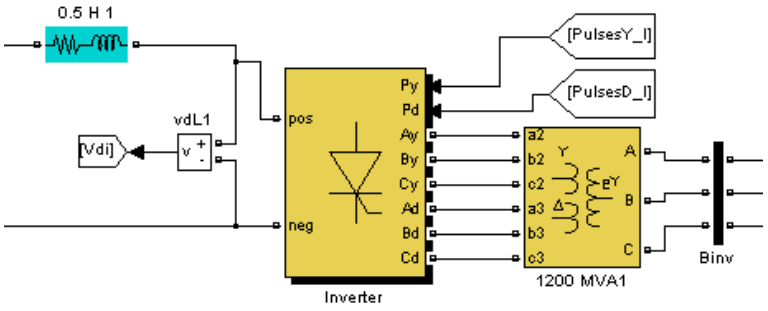

Figure 3.13. Schematic diagram of the inverter in Matlab/SimPowerSystems.

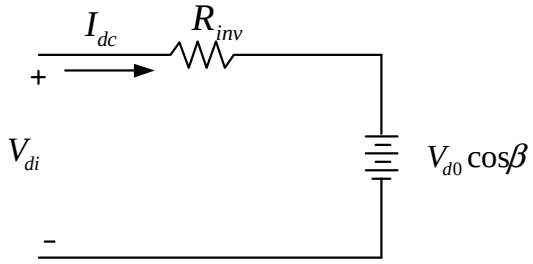

Figure 3.14. The equivalent circuit of the inverter.

where β is the firing advance angle of the inverter in the range of 90^0 and 180^0; $R_{inv} = \frac{3}{\pi}X_c$ is the commutating reactance per phase, B is the number of bridges in series, T is the transformer ration, and V_{acL-L} is the line-to-line rms value of the ac voltage.

Ignore the power losses, then the ac power is equal to the dc power:

$$P_{ac} = P_{dc} \tag{3.26}$$

3.2.3 AC Filters

LCC converters generate low order harmonic currents and harmonic voltages, which will be injected into power system. The harmonic orders depend on the pulse number. A converter with p pulse generates harmonic orders $pq \pm 1$, q is an integer. For 12-pulse converter, the ac harmonic orders will be $12q \pm 1$ (i.e., 11th, 13th, 23th, 25th...). Also, their amplitudes decrease with harmonic order. Some undesirable effects may occur if the harmonics enter the ac power system, such as telephone interference, overheating of capacitors and generators, higher losses, etc.[59, 60, 61]. Normally, filters are adopted on the ac side to reduce the harmonics. Furthermore, they can also supply reactive power at the fundamental frequency. A typical filter system contains single tuned filter, high-pass filter and C-type filter.

3.2.3.1 Single Tuned Filter

A single tuned filter is a kind of band-pass filter tuned at a single frequency. Fig. 3.15 shows a block diagram of the single tuned filter. The values of the capacitor, inductance and resistance are determined by the tuned frequency, reactive power at nominal voltage and quality factor [45, 46]. The reactive power Q_c at fundamental frequency f_1 is calculated as follows: $Q_c = \frac{n^2}{n^2-1}\frac{V^2}{X_c}$, where n is the harmonic order, V is the nominal line-line voltage, X_c is the capacitor reactance at fundamental frequency. Then the value of the capacitor is: $C = \frac{Q_c(n^2-1)}{\omega n^2 V^2}$

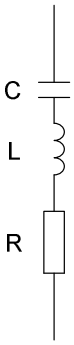

Figure 3.15. Single tuned filter.

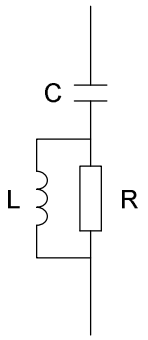

Figure 3.16. High-pass filter.

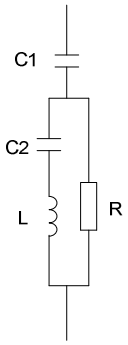

Figure 3.17. C-type filter.

The quality factor Q is a measurement of the tuning frequency. Q is the quality factor of the reactance at the tuning frequency: $Q = \frac{nX_L}{R} = \frac{X_c}{nR}$. Then the value of the resistance is: $R = \frac{1}{\omega C n Q}$. In addition, the value of the inductance is: $L = \frac{1}{\omega^2 n^2 C}$.

A Double tuned filter is also used in the ac filters for HVDC, which is a kind of single tuned filter. The only difference is that the double tuned filter tuned at two different harmonic orders.

3.2.3.2 High-Pass Filter

The high-pass filter is used to filter out the high frequency harmonics. As seen in Fig. 3.16, the resistance R and inductance L are connected in parallel. The quality factor of the high-pass filter is the quality factor of the parallel RL circuit at the tuning frequency:

$$Q = \frac{R}{L \cdot 2\pi f_n} \tag{3.27}$$

where f_n is the tuning frequency. The values of capacitor, inductance and resistance can be calculated as follows [45]:

$$\begin{cases} C = \frac{Q_c(n^2-1)}{\omega n^2 V^2} \\ L = \frac{V^2}{(n^2-1)\omega Q_c} \\ R = Q \cdot 2\pi L f_n \end{cases} \tag{3.28}$$

3.2.3.3 C-Type Filter

A C-type filter is a kind of high-pass filter as shown in Fig. 3.17, where the inductance L is replaced with a series LC circuit. It is capable not only of filtering out low order harmonics, but also of providing reactive power. The quality factor of a C-type filter is the same as the high-pass filter:

$$Q = \frac{R}{L \cdot 2\pi f_n} \tag{3.29}$$

R, L values can be calculated in the same way as high-pass filter [47, 48].

$$\begin{cases} L = \frac{V^2}{(n^2-1)\omega Q_c} \\ R = Q \cdot 2\pi L f_n \end{cases} \tag{3.30}$$

The only difference is the capacitors. C_1 is determined by the required reactive power at the nominal voltage, which is derived as follows:

$$C_1 = \frac{Q_c}{\omega V^2} \tag{3.31}$$

The series of C_1 and C_2 is an equivalent C, which could be found as follows:

$$\begin{cases} C = \frac{Q_c(n^2-1)}{\omega n^2 V^2} \\ \frac{1}{C} = \frac{1}{C_1} + \frac{1}{C_2} \end{cases} \tag{3.32}$$

Then C_2 can be calculated from C and C_1.

3.2.3.4 Example

This paragraph gives an example to explain the function of the ac filters and their parameter design for a real system. For the thyristor-based HVDC link given in the demo of Matlab/SimPowerSystems, it is a 1000MW HVDC system used to transmit power from a 500KV, 60Hz system to a 345KV, 50Hz system. For a rated 1000MW LCC-HVDC, the required reactive power at the ac side is about 50%-60% of the dc power under most normal operations [62]. For the sending end, an ac filter block composed of a capacitor bank, single tuned filter and high-pass filter is designed to give 600 MVar reactive power. The capacitor bank provides 150MVar. The parameters of a single tuned filter to filter out the 11th filter is designed as follows:

The capacitor value is:

$$C = \frac{Q_c(n^2-1)}{\omega n^2 V^2} = \frac{150 * 10^6(11^2-1)}{2\pi * 60 * 11^2(500*10^3)^2} \approx 1.6\mu F \tag{3.33}$$

where this single tuned filter provides 150Mvar reactive power, hence, $Q_c = 150 * 10^6$. It aims to filter out the 11th filter, then $n = 11$. The frequency of the ac side is 60Hz, which means $\omega = 2\pi 60$, and V is the rated ac voltage. Then the capacitor needed for the single tuned filter is about $1.6\mu F$.

The quality factor Q of the filter is set as 100. Then the parameters of the resistance and inductance can be calculated as:

$$\begin{cases} R = \frac{1}{\omega C n Q} = \frac{1}{2\pi 60 * 1.6 * 10^(-6) * 11 * 100} \approx 1.5\Omega \\ L = \frac{1}{\omega^2 n^2 C} = \frac{1}{(2\pi 60)^2 11^2 * 1.6 * 10^{-6}} \approx 36mH \end{cases} \tag{3.34}$$

A single tuned filter to filter out the 13th harmonic and high-pass filter tuned to the 24th harmonic could also be designed in a similar way.

CHAPTER 4

CONTROL OF WIND GENERATION SYSTEM WITH LCC-HVDC DELIVERY

This chapter describes the basic control scheme for the DFIG-based wind farm and HVDC. The RSC of DFIG is designed to control the active and reactive power, and the GSC aims to keep the dc-link voltage constant. Conventional power control for the HVDC is discussed in this chapter.

4.1 Phasor-Locked Loop (PLL)

Vector control is deployed for both RSC and GSC to obtain independent control of active power, reactive power and keep the dc-link voltage constant [33]. PI controllers are used to control the variable frequency converters. Three phase ac variables need to be transferred into dc variables, since PI controllers deal with dc variables. To express the phasor variables in qd reference frame, abc to qd reference frame transformation is used. The detailed transformation process was introduced in Chapter 3. The angle ρ for the qd reference frame is calculated by PLL [63, 64, 65, 66, 67, 68]. The expression of the system voltage V_s in qd reference frame is:

$$V_{sd} = V_s \cos(\omega_0 t + \theta_0 - \rho) \tag{4.1}$$

$$V_{sq} = V_s \sin(\omega_0 t + \theta_0 - \rho) \tag{4.2}$$

From the above expression, when $\rho(t) = \omega_0 + \theta_0$, $V_{sq} = 0$. The function of PLL is to regulate ρ at $\omega_0 + \theta_0$. The schematic diagram of the PLL is shown in Fig. 4.1 [69]. It is seen that the three phase voltage V_s in abc frame is transformed into qd frame with the

sine and cosine values of the angle ρ. The PI controller forces the q-axis component V_{sq} to its reference value zero through adjusting the rotation speed ω of the qd frame. The angle ρ is the integration of the rotation speed ω.

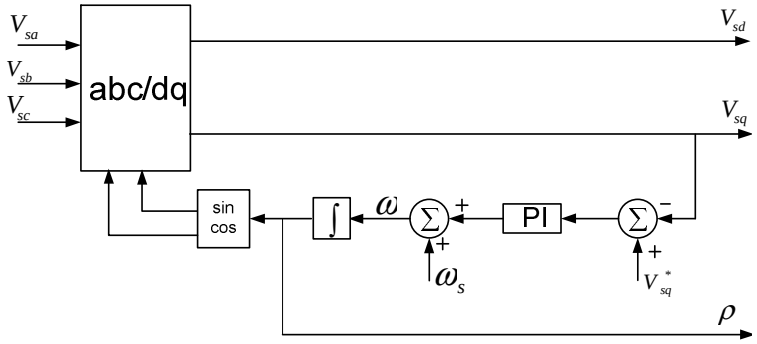

Figure 4.1. Schematic diagram of the phasor-locked loop(PLL).

4.2 Control Scheme for Rotor-Side Converter (RSC)

In most cases, the controller for the RSC contains two cascade control loops the outer loop for power control, the inner loop for current control [33]. The expression of rotor voltage can be obtained from the model of DFIG as described in the previous chapter:

$$v_r = r_r i_r + \frac{d\lambda_r}{dt} + j(\omega - \omega_r)\lambda_r \tag{4.3}$$

Since the rotor flux λ_r can be expressed by rotor current i_r and stator flux λ_s as follows:

$$\lambda_r = L_r \sigma i_r + \frac{L_m}{L_s}\lambda_s \tag{4.4}$$

where $\sigma = (1 - \frac{L_m^2}{L_r L_s})$ Hence, under steady-state, the q-axis and d-axis of the rotor voltage can be expressed by:

$$\begin{cases} v_{qr} = r_r i_{qr} + \sigma L_r \frac{di_{qr}}{dt} - \omega_{slip}\sigma L_r i_{dr} \\ v_{dr} = r_r i_{dr} + \sigma L_r \frac{di_{dr}}{dt} - \omega_{slip}(\sigma L_r i_{qr} + \frac{L_m}{L_s}\lambda_s) \end{cases} \tag{4.5}$$

If we make the following definition:

$$\begin{cases} v_{qr'} = v_{qr} + \omega_{slip}\sigma L_r i_{dr} \\ v_{dr'} = v_{dr} + \omega_{slip}(\sigma L_r i_{qr} + \frac{L_m}{L_s}\lambda_s) \end{cases} \tag{4.6}$$

Then

$$\begin{cases} v_{qr'} = r_r i_{qr} + \sigma L_r \frac{di_{qr}}{dt} \\ v_{dr'} = r_r i_{dr} + \sigma L_r \frac{di_{dr}}{dt} \end{cases} \tag{4.7}$$

The above expressions of $v_{qr'}$ and $v_{dr'}$ are differential equations in time domain, the expressions in s-domain are:

$$\begin{cases} v_{qr'} = r_r i_{qr} + \sigma L_r s i_{qr} = (r_r + \sigma L_r s) i_{qr} \\ v_{dr'} = r_r i_{dr} + \sigma L_r s i_{dr} = (r_r + \sigma L_r s) i_{dr} \end{cases} \tag{4.8}$$

Also, $v_{qr'}$ and $v_{dr'}$ could be designed by PI controllers as follows:

$$\begin{cases} v_{qr'} = (K_{p1} + \frac{K_{i1}}{s})(i^*_{qr} - i_{qr}) \\ v_{dr'} = (K_{p2} + \frac{K_{i2}}{s})(i^*_{dr} - i_{dr}) \end{cases} \tag{4.9}$$

Then the block diagram of the current-controlled system can be seen in Fig. 4.2.

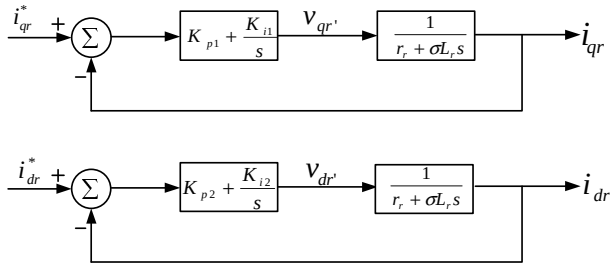

Figure 4.2. Schematic diagram of the controller for RSC in qd reference frame.

The open loop transfer function $l(s)$ of the system is (open loop transfer functions of the q-axis and d-axis are the same):

$$l(s) = (K_{p1} + \frac{K_{i1}}{s})\frac{1}{r_r + \sigma L_r s} \tag{4.10}$$

Then the closed loop transfer function $G(s)$ is:

$$G(s) = \frac{l(s)}{1 + l(s)} = \frac{1}{1 + s\frac{\sigma L_r s + r_r}{K_p s + K_i}} \tag{4.11}$$

In addition, the general closed-loop transfer function is:

$$G(s) = \frac{1}{1 + \tau_i s} \tag{4.12}$$

where τ is the time constant of the resultant closed-loop system. Then the parameters of the PI controller K_p and K_i can be calculated through τ_i:

$$\begin{cases} K_p = K_{p1} = K_{p2} = \frac{\sigma L_r}{\tau_i} \\ K_i = K_{i1} = K_{i2} = \frac{r_r}{\tau_i} \end{cases} \tag{4.13}$$

A smaller τ_i means faster control response. Typically, τ_i is in the range of 0.5-5ms.

To verify the design of PI parameters, an example is given. Here, the key parameters of the wind generator in [70] are listed in the following table. From the nominal power and

Table 4.1. Parameters of the simulated wind generator

nominal power	$1.678(MW)$
nominal voltage	$2.3(kV)$
rotor resistance r_r	$26(m\Omega)$
stator inductance L_s	$35.12(m\Omega)$
rotor inductance L_r	$35.12(m\Omega)$
magnetizing inductance L_m	$34.52(m\Omega)$

voltage, the base impedance Z_b is calculated as: $Z_b = \frac{V_b^2}{S_b} = \frac{(2.3*10^3)^2}{1.678*10^6} = 3.1525\Omega$. Then the per unit value of the resistance, inductance can be found. From L_m, L_s and L_r, σ can be

calculated as follows:

$$\sigma = 1 - \frac{L_m^2}{L_s L_r} = 1 - \frac{34.52 * 10^{-3}/3.1525}{35.12 * 10^{-3}/3.1525 * 35.12 * 10^{-3}/3.1525} = 0.034 \tag{4.14}$$

Then $K_p = \frac{\sigma L_r}{\tau_i} = \frac{0.034*35.12*10^{-3}/3.1525}{1.136*10^{-3}} \approx 333.33$, and $K_i = \frac{r_r}{\tau_i} = \frac{26*10^{-3}/3.1525}{1.136*10^{-3}} \approx 7.26$ where the time constant τ_i used here is $1.136ms$, the calculated K_p and K_i are very close the values used in [70].

The outer control loop of RSC is analyzed as follows: from the model of DFIG as described in (3.13), the stator voltage is calculated as:

$$v_s = r_s i_s + \frac{d\lambda_s}{dt} + j\omega\lambda_s \tag{4.15}$$

where

$$\lambda_s = L_s i_s + L_m i_r \tag{4.16}$$

Under steady-state, and ignoring the stator resistance, the stator voltage will be:

$$v_s = j\omega\lambda_s \tag{4.17}$$

From (4.16) and (6.7), the active and reactive power can be calculated:

$$P_s + jQ_s = \frac{3}{2} v_s i_s^* = \frac{3}{2} j\omega\lambda_s (\frac{1}{L_s}(\lambda_s - L_m i_r))^* \tag{4.18}$$

The basic control of DFIG is based on stator flux orientated control, where the d-axis is aligned with the stator flux, which means $\lambda_s = \lambda_{ds}$, $\lambda_{qs} = 0$. Hence,

$$P_s + jQ_s = -\frac{3}{2} j\omega\lambda_s \frac{L_m}{L_s} i_{qr} + j\frac{3}{2}\omega\lambda_s \frac{1}{L_s}(\lambda_s - L_m i_{dr}) \tag{4.19}$$

Then the active power and reactive are calculated through:

$$P_s = -\frac{3}{2} j\omega\lambda_s \frac{L_m}{L_s} i_{qr} \tag{4.20}$$

$$Q_s = \frac{3}{2}\omega\lambda_s \frac{1}{L_s}(\lambda_d s - L_m i_{dr}) \tag{4.21}$$

The above expressions of P_s and Q_s indicate that the rotor current component i_{qr} could be regulated through the stator active power P_s, while the d-axis component i_{dr} can be regulated through the stator reactive power Q_s. Hence, the outer power control loop could be designed to get the reference value of rotor current. PI controllers are also used in the outer loop control; the parameters of the outer loop PI controller is similar to the inner loop. The only difference is that the outer loop is much faster than the inner loop [71]. Therefore, the time constant τ_i of the outer loop is higher than the inner loop.

Hence, the whole RSC control loop can be shown in Fig. 4.3.

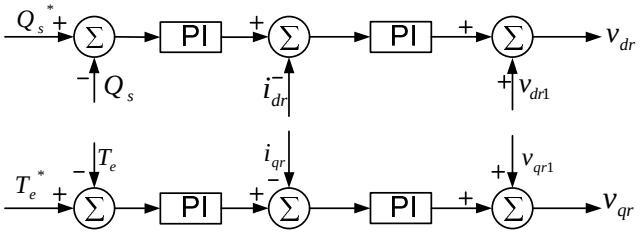

Figure 4.3. Control scheme for RSC: $v_{qr1} = -\omega_{slip}\sigma L_r i_{dr}$, $v_{dr1} = -\omega_{slip}(\sigma L_r i_{qr} + M/L_s\lambda_s)$.

4.3 Control Scheme for Grid-Side Converter (GSC)

Similar to the RSC, the GSC also has two cascaded control loops. The inner current control loops for the GSC could be designed using the same procedures as the RSC. The grid-side voltage could be obtained through the PI controllers and feedback loops.

From the equivalent circuit of the GSC as shown in Fig. 3.7, the q-axis and d-axis components of the GSC side voltage can be calculated as follows:

$$\begin{cases} v_{qg} = -R_g i_{qg} - \omega_s L_{tg} \frac{di_{qg}}{dt} - \omega_s L_{tg} i_{dg} + v_{qs} \\ v_{dg} = -R_g i_{dg} - \omega_s L_{tg} \frac{di_{dg}}{dt} + \omega_s L_{tg} i_{qg} + v_{ds} \end{cases} \tag{4.22}$$

If we define:

$$\begin{cases} v_{qg}^{'} = v_{qg} + \omega_s L_{tg} i_{dg} - v_{qs} \\ v_{dg}^{'} = v_{dg} - \omega_s L_{tg} i_{qg} - v_{ds} \end{cases} \tag{4.23}$$

Then

$$\begin{cases} v_{qg}^{'} = -R_g i_{qg} - \omega_s L_{tg} \frac{di_{qg}}{dt} \\ v_{dg}^{'} = -R_g i_{dg} - \omega_s L_{tg} \frac{di_{dg}}{dt} \end{cases} \tag{4.24}$$

In s-domain, the expressions of $v_{qg}^{'}$ and $v_{dg}^{'}$ are:

$$v_{qg}^{'} = -R_g i_{qg} - \omega_s L_{tg} s i_{qg} = -(R_g + \omega_s L_{tg} s) i_{qg} \tag{4.25}$$

$$v_{dg}^{'} = -R_g i_{dg} - \omega_s L_{tg} s i_{dg} = -(R_g + \omega_s L_{tg} s) i_{dg} \tag{4.26}$$

In addition, $v_{qg}^{'}$ and $v_{dg}^{'}$ could be designed by PI controllers as follows:

$$\begin{cases} v_{qg}^{'} = (K_{p3} + \frac{K_{i3}}{s})(i_{qg}^{*} - i_{qg}) \\ v_{dg}^{'} = (K_{p4} + \frac{K_{i4}}{s})(i_{dg}^{*} - i_{dg}) \end{cases} \tag{4.27}$$

Then the block diagram of the current-controlled system can be seen in Fig. 4.4.

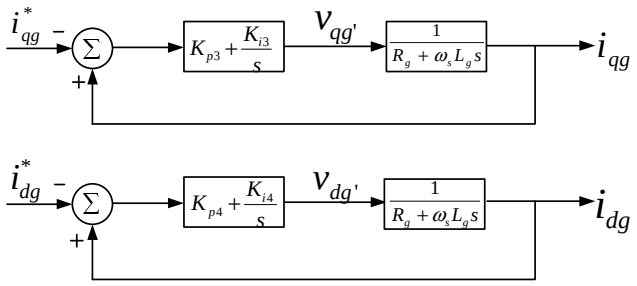

Figure 4.4. Schematic diagram of the controller for GSC in qd reference frame.

The open loop transfer function $l(s)$ of the system is (open loop transfer functions of the q-axis and d-axis are the same):

$$l(s) = (K_p + \frac{K_i}{s})\frac{1}{R_g + \omega_s L_{tg} s} \tag{4.28}$$

Then the closed loop transfer function $G(s)$ is:

$$G(s) = \frac{l(s)}{1 + l(s)} = \frac{1}{1 + s\frac{R_g + \omega_s L_{tg} s}{K_p s + K_i}} \tag{4.29}$$

The general closed-loop transfer function is:

$$G(s) = \frac{1}{1 + \tau_i s} \tag{4.30}$$

where τ is the time constant of the resultant closed-loop system. Then the parameters of the PI controller K_p and K_i can be calculated through τ_i:

$$\begin{cases} K_p = K_{p3} = K_{p4} = \frac{\omega_s L_{tg}}{\tau_i} \\ K_i = K_{i3} = K_{i4} = \frac{R_g}{\tau_i} \end{cases} \tag{4.31}$$

For the outer control loop, the dynamic expression of the dc-link between RSC and GSC is described through (3.21) in the previous chapter. When the terminal voltage phasor $\bar{v}_s$ of the DFIG is oriented at q-axis, the qd-axis voltages become: $v_{qs} = v_s$, $v_{ds} = 0$. Hence

the GSC power becomes: $P_g = real(v_s i_g^*) = v_{qs} i_{qg}$. Thus, the dc-link voltage dynamic equation can be expressed as:

$$CV_{dc}\frac{dV_{dc}}{dt} = v_{qs} i_{qg} - P_r. \tag{4.32}$$

Hence, the reference value of q-axis grid-side current i_{qg}^* could be generated by the PI controller as follows:

$$i_{qg}^* = (K_{p5} + \frac{K_{i5}}{s})(V_{dc}^* - V_{dc}) \tag{4.33}$$

On the other hand, the d-axis grid-current component i_{dg} responds to the grid-side reactive power Q_g. Hence, a similar PI controller could also be designed to get the reference value of i_{dg}:

$$i_{dg}^* = (K_{p6} + \frac{K_{i6}}{s})(Q_g^* - Q_g) \tag{4.34}$$

The whole control scheme of GSC is shown in Fig. 4.5. It is obvious that through GSC current control, the voltage of dc-link V_{dc} could be kept constant. As shown in (3.18), the stator terminal voltage could be controlled through i_{qg}.

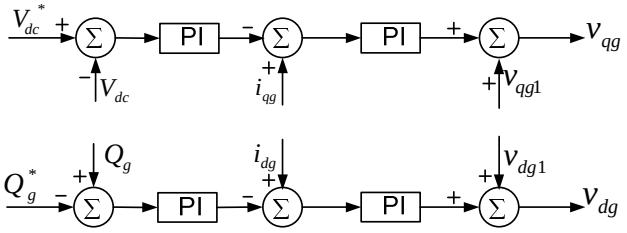

Figure 4.5. Control scheme for GSC: $v_{qg1} = v_{qs} - \omega_s L_{tg} i_{dg}$, $v_{dg1} = v_{ds} + \omega_s L_{tg} i_{qg}$.

The schematic diagram of the controllers for both RSC and GSC in qd reference frame is shown in Fig. 4.6.

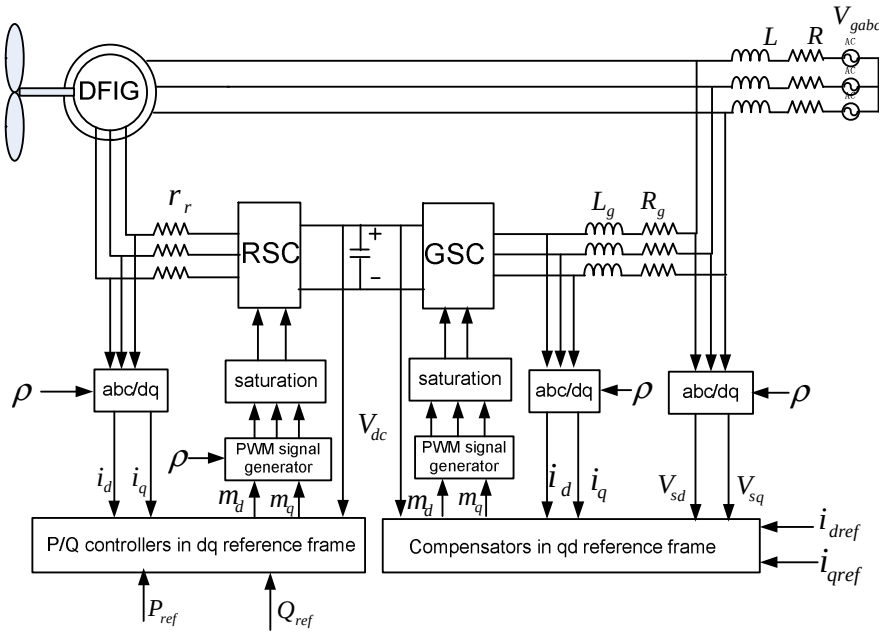

Figure 4.6. Simplified block diagram of the current control scheme for RSC and GSC.

4.4 Control of HVDC

To ensure stable and efficient operation, the HVDC system should be well controlled. This part introduces the basic control principle of the HVDC system. Considering the equivalent circuit of the HVDC link as shown in Fig. 4.7, the dc current flowing through the dc line is:

$$I_{dc} = \frac{V_{d0r}\cos\alpha - V_{d0i}\cos\beta}{R_{rec} + R_{dc} + R_{inv}} \tag{4.35}$$

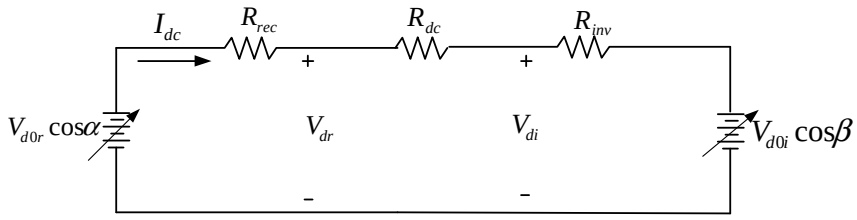

Figure 4.7. The equivalent circuit of an HVDC link [2].

It is obvious that the dc voltage and dc current could be regulated through the internal voltages($V_{d0r}\cos\alpha$ and $V_{d0i}\cos\beta$). Also, the internal voltages are controlled by the ignition angle α and β. Hence, the dc voltage and current could be controlled through adjusting the ignition angles. The basic control philosophy of HVDC system is constant current control for the rectifier and constant extinction angle control for the inverter. Fig. 4.8 shows the ideal V-I characteristics. The rectifier V-I characteristic is a vertical line, while the inverter V-I characteristic is a slightly slopped line. The intersection of the two lines is the operating point.

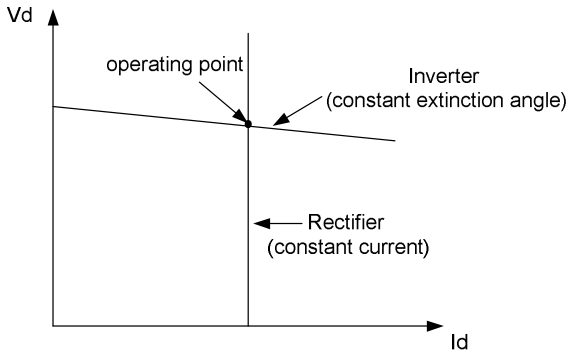

Figure 4.8. The ideal V-I characteristics of the HVDC system [2].

When a wind farm is connected to the grid through HVDC, the receiving end of the HVDC needs to absorb the generated wind power excluding the losses on the transformers and lines. The conventional control scheme of the rectifier of HVDC-link is constant power control as shown in Fig. 4.9. The current order is determined by the power order divided by the measured dc voltage. The computed current order is used as the input signal to the current control loop.

On the other hand, constant voltage control mode is normally used for the inverter. A closed-loop PI controller as shown in Fig. 4.10 is designed to keep the dc voltage constant.

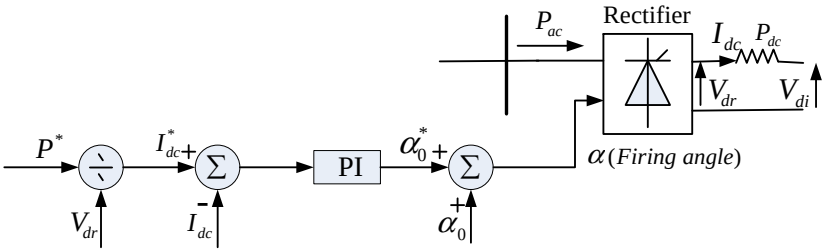

Figure 4.9. Constant power control diagram.

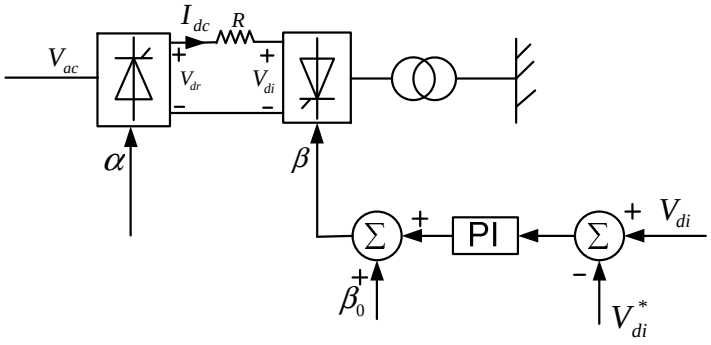

Figure 4.10. Constant voltage control diagram for the inverter.

CHAPTER 5

FAULT-RIDE THROUGH (FRT) OF DIRECT CONNECTED DFIG-BASED WIND FARM

This chapter has been published in Electric Power Systems Research and appears in this dissertation with Elsevier's permission.

Under unbalanced stator conditions, DFIGs will suffer rotor current harmonics and torque pulsations which can cause excessive shaft stress and winding losses. Currently, the control techniques to reduce the torque pulsation include rotor-side converter (RSC) injected voltage compensation [30, 31] and grid-side converter (GSC) compensation [32].

DC-link voltage fluctuation is also an important issue under unbalanced stator conditions. DC-link voltage pulsation represents the unbalanced power communication between RSC and GSC. In [31], the RSC control loop limits the DFIG torque oscillation, and the GSC compensates the DFIG stator active power oscillation to ensure zero oscillation in the dc-link voltage. Similar ride-through control of DFIG is also described in [34]. [72] gives detailed discussions about the dc-link voltage fluctuation issue during a balanced three-phase grid fault. Instantaneous rotor power feedback is proposed to limit the oscillation of the dc-link voltage.

Controls can be realized through current control loops [31, 33, 32, 35, 10, 34, 12], or through direct power control [36, 37]. The current controllers either adopt synchronous reference frame(qd^+) or both positive synchronous and negative synchronous reference frame(qd^+ and qd^-). The latter approach decomposes and extracts harmonics in rotor currents and control them separately [31]. A similar qd^+ and qd^- approach is used in [32], [34] and [12] to extract the negative sequence currents to the grid in qd^- reference

frame, and then adopt proportional and integral (PI) controllers to compensate the negative sequence current from grid-side converters.

The first approach in [30] and [73, 74] uses only one reference frame qd^+ and ultimately dealing with $2\omega_e$ frequency harmonics. In [30], the controller design requires careful tuning. While in [73, 74], proportional integral and resonant (PIR) controllers are adopted to eliminate the $2\omega_e$ frequency harmonics. The second approach in [31] and [32] requires two reference frames and filters to trap high frequency harmonics. More recently, for generalized grid converters, $\alpha\beta$ reference frame is used and proportional resonance controller is adopted [35].

The purpose of this chapter is to investigate negative sequence compensation techniques by RSC and/or GSC. The limitation of using either RSC or GSC is presented. A coordinated control technique with simplified structure is proposed here. Matlab/Simulink tests for a 2MW DFIG demonstrate the effectiveness of the control technique.

5.1 Analysis of DFIG Under Unbalanced Grid Voltage and Negative Sequence Compensation

The transients in rotor voltages due to stator voltage dip are analyzed in [75]. Under unbalanced grid voltage, the most severe operation problems are the torque ripple due to the negative sequence components in the stator and rotor currents and the dc-link voltage ripple [12]. The steady state components in the rotor currents and electromagnetic torque are analyzed in [76]. In this section, the rotor current components, the torque components are presented along with negative sequence compensation techniques via RSC or GSC and their consequence on dc-link voltage ripple.

5.1.1 Components in Rotor Currents and Electromagnetic Torque Under Unbalanced Grid Voltage

Table 5.1 shows the components in the three reference frames.

Table 5.1. Rotor current components observed in various reference frames

	stationary abc	qd^+	qd^-	$\alpha\beta$
Positive sequence	$s\omega_e$	0	$-2\omega_e$	ω_e
Negative sequence	$-(2-s)\omega_e$	$2\omega_e$	0	$-\omega_e$

Under unbalanced stator conditions, the torque can be decomposed into four components:

$$T_e = T_{e1} + T_{e2} + T_{e3} + T_{e4} \tag{5.1}$$

where T_{e1} is due to the interaction of $\bar{I}_{s+}$ and $\bar{I}_{r+}$, T_{e2} is due to the interaction of $\bar{I}_{s-}$ and $\bar{I}_{r-}$, T_{e3} is due to the interaction of $\bar{I}_{s+}$ and $\bar{I}_{r-}$, and T_{e4} is due to the interaction of $\bar{I}_{s-}$ and $\bar{I}_{r+}$. T_{e1} and T_{e2} are due to the interaction of the same harmonic order currents or mmfs. Hence these two are dc components. T_{e3} and T_{e4} are pulsating components with a frequency of $2\omega_e$. The frequencies of those components are listed in Table 5.2.

Table 5.2. Electromagnetic torque components

Component	T_{e1}	T_{e2}	T_{e3}	T_{e4}
Frequency	0	0	$2\omega_e$	$2\omega_e$

5.1.2 Negative Sequence Compensation Using One Converter and Its Limitation

To reduce the torque pulsation, negative sequence compensation is widely adopted in literature. Negative sequence compensation can be done by either RSC or GSC. In the following paragraphs, the compensation techniques are present along with their limitations.

5.1.2.1 Negative Sequence Compensation via GSC

[32] presents the negative sequence compensation technique through GSC. The main scheme behind the proposed method is to let the GSCs compensate the negative sequence current required in the network during unbalanced operation. As shown in the circuit model Fig. 5.1, the GSCs will provide the negative sequence components for the currents to the grid. Then the stator currents will not contain the negative sequence component.

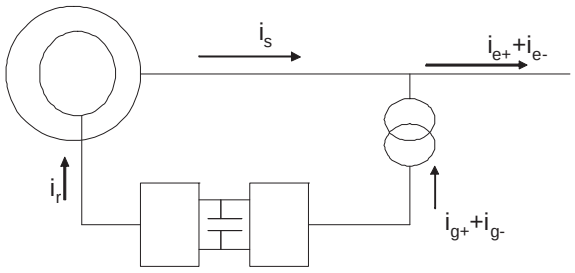

Figure 5.1. The control philosophy: negative sequence compensation through GSC: $i_{g-} = i_{e-}$.

In this negative sequence compensation method, the current controllers of GSC will sense the currents through the network, and provide negative sequence currents for compensation. Since the GSC provides the negative sequence current to the grid, the active power generated from the GSC has a dc component and a pulsating component with a frequency of $2\omega_e$. The dc-link voltage is determined by the two instantaneous active powers P_r and P_g:

$$CV_{dc}\frac{dV_{dc}}{dt} = P_g - P_r. \tag{5.2}$$

Since there is only negative sequence compensation from the GSC, and the rotor power P_r has only dc component, then the dc-link voltage will have two pulsating components at frequencies of $2\omega_e$ and $4\omega_e$ [77].

5.1.2.2 Negative Sequence Compensation via RSC

RSC could also be used to provide negative sequence compensation to reduce the torque pulsation [31]. From the steady-state circuit model as shown in Fig. 5.2, it can be found that injecting a negative sequence voltage from the RSC can compensate the negative sequence rotor current ($\bar{I}_{ar}^{-} = 0$). [31] presents the detailed derivation process of the rotor current reference values.

In this method, a negative sequence voltage will be injected to the RSC, which will introduce a second harmonic power component. The RSC active power is $P_r = real(V_r I_r^*)$. For interactions between the rotor current and voltage of the opposite sequence (+, -) or

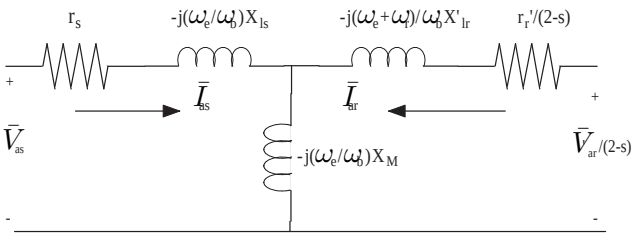

Figure 5.2. Steady-state induction machine circuit representation.

(-, +), the rotor power will have a pulsating component with frequency $2\omega_e$. Thus, the resultant power can also be decomposed into four components:

$$P_r = P_{r1} + P_{r2} + P_{r3} + P_{r4} \tag{5.3}$$

where P_{r1} is due to the interaction of $\bar{V}_{r+}$ and $\bar{I}_{r+}$, P_{r2} is due to the interaction of $\bar{V}_{r-}$ and $\bar{I}_{r-}$, P_{r3} is due to the interaction of $\bar{V}_{r+}$ and $\bar{I}_{r-}$, and P_{r4} is due to the interaction of $\bar{V}_{r-}$ and $\bar{I}_{r+}$. P_{r1} and P_{r2} are due to the interaction of the same harmonic order currents and voltages. Hence these two are dc components. P_{r3} and P_{r4} are pulsating components with frequency of $2\omega_e$.

The main drawback of this method is that the dc-link voltage will have ripples with two pulsating components at frequencies of $2\omega_e$ and $4\omega_e$. Because if there is only negative sequence compensation from the RSC, and we assume that the GSC power P_g has only dc component, then it will lead to dc voltage ripples.

5.2 Proposed Coordination Technique Under Unbalanced Grid Condition

As analyzed in the previous paragraph, ripples in the torque and dc-link voltages will be produced under unbalanced grid conditions. Hence, when there is unbalanced grid fault, the control objectives are obvious: 1) to suppress torque ripples; 2) to reduce the ripples in the dc-link voltages; 3) to reduce the magnitude of the rotor currents.

Various control techniques based on RSC and GSC have been introduced in the literature. In [33, 10], the RSC is used to eliminate the torque oscillations at double supply

frequency while the GSC is controlled to cancel the stator power pulsation. Therefore, the overall output power from the DFIG system is then kept constant. In [34, 12], the RSC is controlled to eliminate the torque oscillations while the GSC is designed to keep dc voltage constant. In [33, 10], the negative sequence current reference values of GSC are derived from the stator power measurements while in [34], the GSC negative sequence current reference values are computed from the rotor power measurement.

Objectives 1 and 3 are equivalent since reduction of the negative sequence of rotor current results in reduction of torque ripples. Instead of computing the reference values of the RSC negative sequence currents, the reference values are set to zero. The purpose of the negative sequence RSC current controller is to eliminate the negative sequence rotor current. Dual sequence controllers to separately control the positive sequence and negative sequence rotor current are applied in [34, 12]. Filters are applied to separate the currents after abc/qd transformation. Filters can introduce time delay and deteriorate control performance. Hence in [33, 10], the main controller dealing with the positive sequence is implemented without filter, only the auxiliary controller dealing with the negative sequence rotor currents have filters. The control structure can be simplified using proportional resonant (PR) controller. A PR controller can be considered an ac signal tracker just as a PI controller is a dc signal tracker [78]. A PR controller has been tested to eliminate the negative sequence rotor current by the authors in [79]. Here, the same rotor current control structure is adopted. The control loop is simplified.

The GSC is also controlled to keep the dc-link voltage constant. Instead of using dual current sequence controller similar to [33, 10, 34, 12], a technique in [72] to limit dc-link voltage fluctuation is adopted in GSC control. The key idea is that the current reference value should change to reflect the instantaneous power transfer through the dc-link. Thus the instantaneous rotor power is measured and used to obtain the current reference value. The method has been verified in [72] for symmetric voltage dip and it is found that the dc-link voltage fluctuation is effectively limited. In unbalanced grid conditions, the dc-link voltage also suffers fluctuation; the same method can be used to limit the fluctuation.

The details of the control of the GSC and RSC are given in the following subsections.

5.2.1 RSC Control

Under unbalanced stator conditions, the negative sequence stator currents form the clockwise rotating mmf in the machine air gap. This mmf will then induce a clockwise rotating flux in the gap, which in turn induces an emf in the rotor circuit with a frequency of $\omega_e+\omega_m$ or $(2-s)\omega_e$. Correspondingly, the interaction of stator current and rotor current will cause harmonics of electromagnetic torque.

The electromagnetic torque can be expressed as [33]:

$$T_e = T_{edc} + T_{ecos}\cos(2\omega_e t) + T_{esin}\sin(2\omega_e t), \tag{5.4}$$

where

$$\begin{cases} T^+_{edc} = K(\lambda^+_{qs+}I^+_{qr+} + \lambda^+_{ds+}I^+_{dr+} + \lambda^-_{qs-}I^-_{qr-} + \lambda^-_{ds-}I^-_{dr-}) \\ T^+_{ecos} = K(\lambda^+_{qs+}I^-_{qr-} + \lambda^+_{ds+}I^-_{dr-} + \lambda^-_{qs-}I^+_{qr+} + \lambda^-_{ds-}I^+_{dr+}) \\ T^+_{esin} = K(\lambda^+_{ds+}I^-_{qr-} - \lambda^+_{qs+}I^-_{dr-} - \lambda^-_{ds-}I^+_{qr+} + \lambda^-_{qs-}I^+_{dr+}) \end{cases} \tag{5.5}$$

and $K = \frac{3}{2}\frac{P}{2}\frac{M}{L_s}$.

To minimize the harmonics of the electromagnetic torque, [33], [12] and [34] set the harmonic parts to zero:

$$\begin{cases} T_{ecos} = 0 \\ T_{esin} = 0 \end{cases} \tag{5.6}$$

Then

$$\begin{cases} \lambda^+_{qs+}I^-_{qr-} + \lambda^+_{ds+}I^-_{dr-} + \lambda^-_{qs-}I^+_{qr+} + \lambda^-_{ds-}I^+_{dr+} = 0 \\ \lambda^+_{ds+}I^-_{qr-} - \lambda^+_{qs+}I^-_{dr-} - \lambda^-_{ds-}I^+_{qr+} + \lambda^-_{qs-}I^+_{dr+} = 0 \end{cases} \tag{5.7}$$

Thus, from the above two equations, the reference values of negative sequence rotor currents can be calculated. Except for the positive sequence control loop of RSC, another negative sequence control loop is also considered for the electromagnetic torque limitation.

However, calculation of I_{qr-}^{-} and I_{dr-}^{-} through (5.7) and (5.7) is complex, since λ_s should be decomposed into positive and negative sequence components. Hence, qd^{+} and qd^{-} reference frames conversions are necessary. On the other hand, low pass filters are also needed, which cause some delay.

If the rotor current harmonics are properly eliminated, the harmonics of T_e and P_r could also be limited. Hence a simple RSC control is proposed in Fig 5.3 to set I_{qr-}^{-} and I_{dr-}^{-} to zeros. In order to further simplify the control structure, the dual sequence control loop in qd^{+} and qd^{-} is replaced by proportional resonant (PR) control where $\alpha\beta$ reference frame is adopted. Positive sequence reference currents are transformed into $\alpha\beta$ reference frame. Since the negative sequence reference currents are set as zeros, reference currents in $alpha\beta$ contain only positive sequence information. The measurements are also transferred in $\alpha\beta$ frame and become ac variables with a frequency of ω_e. PR controllers are effective for ac signal tracking. Hence the controller will eliminate the negative sequence currents in the rotor.

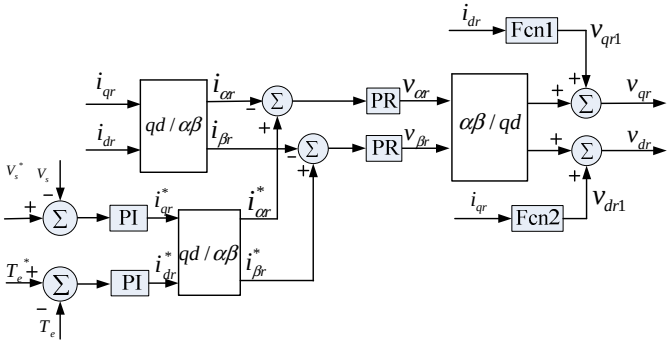

Figure 5.3. Proposed RSC control structure.

5.2.2 GSC Control

DC-link voltage fluctuation is an important issue under unbalanced grid voltage. It is essential to keep the dc-link voltage constant. According to the above analysis of rotor instantaneous power P_r and grid instantaneous power P_g, the harmonics difference between P_r and P_g causes the oscillation of the dc-link voltage. Constant dc-link voltage ensures balanced power communication between RSC and GSC.

In [33], GSC is used to compensate RSC transient power oscillation to ensure constant dc-link voltage. Under unbalanced grid voltage, voltage and current of RSC and GSC have positive and negative components as analyzed.

Hence the rotor power can be expressed as:

$$P_r = real(V_r^+ I_r^{+*}) = P_{rdc} + P_{rcos}\cos(2\omega_e t) + P_{rsin}\sin(2\omega_e t). \tag{5.8}$$

where

$$P_{rdc}^+ = V_{qr+}^+ I_{qr+}^+ + V_{dr+}^+ I_{dr+}^+ + V_{qr-}^- I_{qr-}^- + V_{dr-}^- I_{dr-}^- \tag{5.9}$$

$$P_{rcos}^+ = V_{qr+}^+ I_{qr-}^- + V_{dr+}^+ I_{dr-}^- + V_{qr-}^- I_{qr+}^+ + V_{dr-}^- I_{dr+}^+ \tag{5.10}$$

$$P_{rsin}^+ = V_{qr-}^- I_{dr+}^+ - V_{dr-}^- I_{qr+}^+ - V_{qr+}^+ I_{dr-}^- + V_{dr+}^+ I_{qr-}^- \tag{5.11}$$

The expression of grid power in qd^+ reference frame can be expressed in the same way:

$$P_g = real(V_g^+ I_g^{+*}) = P_{gdc} + P_{gcos}\cos(2\omega_e t) + P_{gsin}\sin(2\omega_e t). \tag{5.12}$$

According to the analysis of the dc-link voltage, to keep the dc-link voltage constant, P_{rcos}^+ should equal to P_{gcos}^+, and P_{rsin}^+ should equal to P_{gsin}^+. Hence, the reference values of I_{qg-}^- and I_{dg-}^- can be calculated from the two equations:

$$P_{rcos} = P_{gcos} \tag{5.13}$$

$$P_{rsin} = P_{gsin} \tag{5.14}$$

The calculation of negative sequence grid currents through (5.13) and (5.14) is very complex. Furthermore, the low pass filters used in dual control loops deteriorate controller performance. A simpler method is sought here.

As the grid current I_g is oriented in the q-axis, hence $I_{qg} = I_g$, $I_{dg} = 0$. The grid power becomes

$$P_g = real(V_g I_g^*) = V_{qg} I_{qg}. \tag{5.15}$$

Thus,

$$CV_{dc}\frac{dV_{dc}}{dt} = V_{qg} I_{qg} - P_r \tag{5.16}$$

Under unbalanced grid condition, the harmonics of the rotor power P_r is obvious as analyzed before. In order to keep the dc-link voltage constant, it is important to consider P_r effect. From (5.11),

$$I_{qg} = CV_{dc}\frac{dV_{dc}}{dt}/V_{qg} + P_r/V_{qg}. \tag{5.17}$$

Based on the GSC control loop, the reference value of I_{qg} should include the rotor power effect P_r/V_{qg}. The new proposed control technique of GSC is shown in Fig. 5.4.

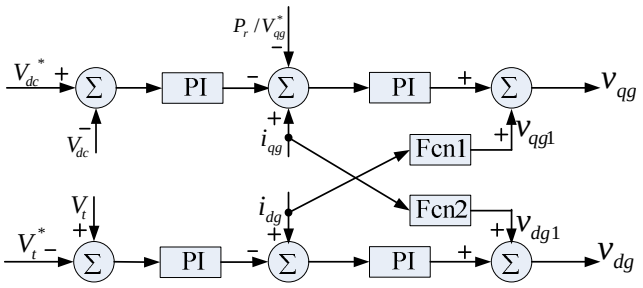

Figure 5.4. Proposed control technique for GSC.

5.3 Simulation Studies

Simulation studies with the proposed control design are carried out in Matlab/Simulink for a 2MW grid-tied DFIG. The parameters of the DFIG are given in Table 5.3. Three scenarios are tested: scenario 1, with only positive sequence control loops of GSC and RSC;

scenario 2, with negative sequence compensation control loops of GSC and RSC; scenario 3, with proposed control technique of GSC and RSC.

Table 5.3. Parameters of the 2MW DFIG

$r_s\ (pu)$	0.00488
$r_r\ (pu)$	0.00549
$X_{ls}\ (pu)$	0.09231
$X_{lr}\ (pu)$	0.09955
$X_M\ (pu)$	3.95279
$H\ (kg.m^2)$	3.5

The Phase A grid voltage will be subjected to a low voltage at 1s. At 1.5 seconds, the voltage will be recovered (as seen in Fig. 5.5).

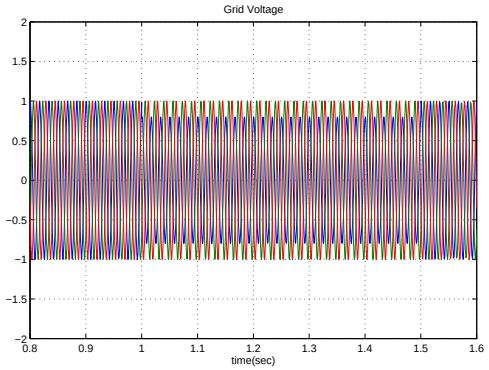

Figure 5.5. Grid voltage during the whole studied time.

During the unbalanced period, the grid and stator currents have positive sequence components (ω_e) and negative sequence components ($-\omega_e$) in stationary abc reference frame. The rotor currents will have a component with a frequency of $s\omega_e$ corresponding to the positive sequence and a component with a frequency of $-(2-s)\omega_e$ corresponding to the negative sequence. The electromagnetic torque is due to the interaction between the stator currents and the rotor currents. From the analysis in the above paragraph, during 1-1.5 s, T_e has a harmonic of a frequency of $2\omega_e$. The dynamic response of electromagnetic torque under the three scenarios are shown in Fig. 5.6 and Fig. 5.7. It is obvious that with a negative sequence compensation technique, the harmonics of electromagnetic torque are limited effectively.

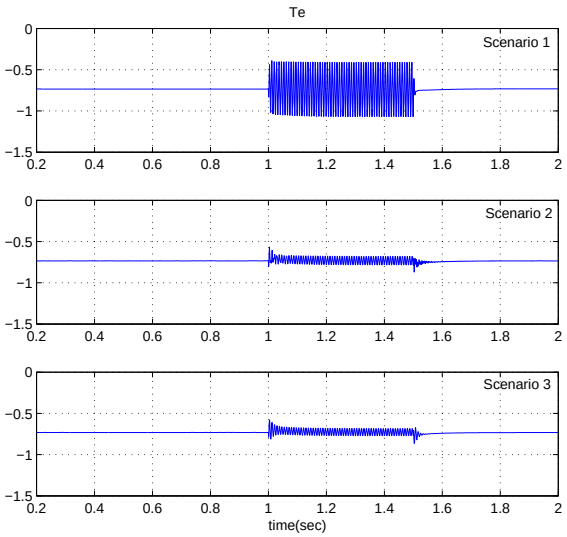

Figure 5.6. Dynamic responses of electromagnetic torque.

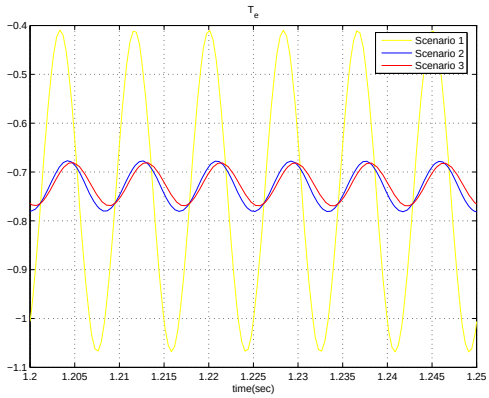

Figure 5.7. Dynamic responses of electromagnetic torque in the center of grid unbalance.

Simulation results of the active power under the above three scenarios can be seen in Fig. 5.8 and Fig. 5.9. Negative sequence compensation techniques suppress the oscillation of P_e compared with only positive sequence control strategy.

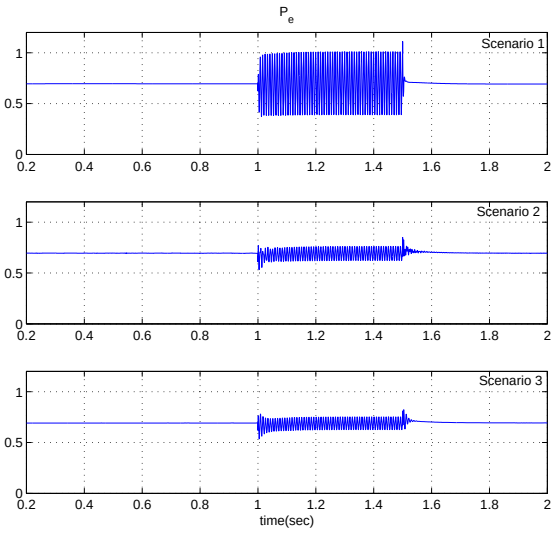

Figure 5.8. Comparison of the total active power from the DFIG.

According to the analysis in the previous section, the harmonics of the dc-link voltage is caused by the oscillation difference between rotor power and grid power. With the negative sequence power compensation technique, the harmonics of the dc-link voltage are greatly reduced compared with only positive sequence control loops.

With the new proposed control technique, through RSC, the rotor current harmonics are eliminated; correspondingly, the harmonics of T_e and P_r are limited. On the other hand, through GSC, the grid power P_g senses the variation of the rotor power P_r. So, the dc-link harmonics are well controlled and it is more effective than the negative compensation technique. The simulation results are shown in Fig. 5.10 and Fig. 5.11.

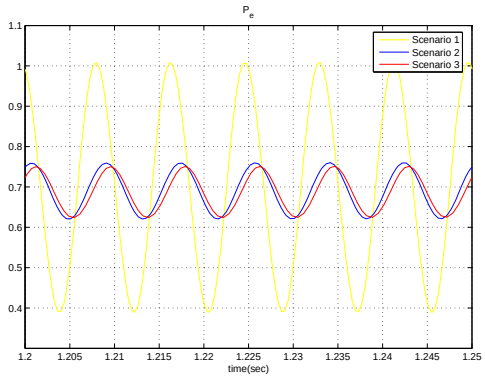

Figure 5.9. Comparison of the total active power plots under three scenarios in the center of grid unbalance.

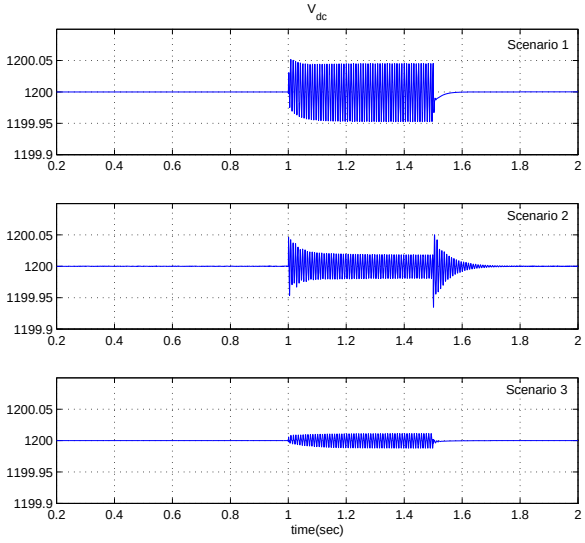

Figure 5.10. Response of dc-link voltage during the whole grid unbalance under three scenarios.

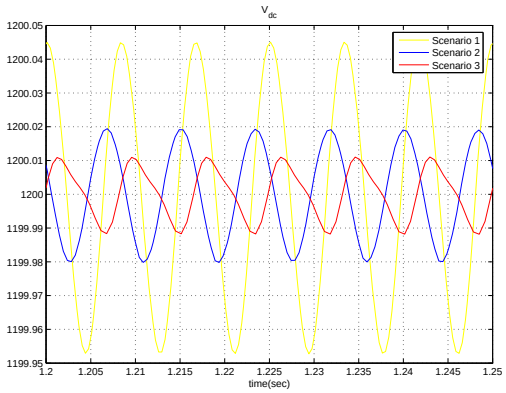

Figure 5.11. Response of dc-link voltage in the center of grid unbalance under three scenarios.

CHAPTER 6

ACTIVE POWER BALANCE

This chapter has been published in North American Power Symposium 2009 and appears in this dissertation with IEEE's permission.

One limitation of wind energy are the ever-changing characteristics of wind, which means the captured wind power is changing all the time. For wind farm with HVDC delivery, the transmitted dc power should balance the varying ac power from the wind farm. Any imbalance will cause stress on the system. Active power balance between a DFIG-based wind farm and HVDC has been discussed in [49, 14]. To ensure coordination between the DFIG-based wind farm and LCC-HVDC transmission, the dc voltage and dc current will decrease/increase according to the wind speed change. In this chapter, a coordination control for DFIG-based wind farm with LCC-HVDC transmission is presented. At the same time, the control part of DFIG is also modified.

6.1 Modified Control of DFIG

The basic control of DFIG is based on stator flux linkage orientated control. The stator flux linkage is oriented in d-axis, which means $\lambda_s = \lambda_{ds}$, and $\lambda_{qs} = 0$. The modified RSC control is based on stator flux linkage control rather than reactive power control, see Fig. 6.1.

From the equation of the stator voltage expression

$$\begin{cases} v_{qs} = r_s i_{qs} + \omega_s \lambda_{ds} + \frac{d\lambda_{qs}}{dt} \\ v_{ds} = r_s i_{ds} - \omega_s \lambda_{qs} + \frac{d\lambda_{ds}}{dt} \end{cases} \tag{6.1}$$

the angle of stator voltage is related to the ratio of v_{ds} and v_{qs}. During steady-state condition, $v_{ds}/v_{qs} = -\lambda_{qs}/\lambda_{ds}$. If the stator resistor is neglected, then the angle of v_s could be tracked if λ_s is well controlled. As the wind speed changes, the reference value of T_e will cause the change of i_{qr}. As a result, λ_{qs} will change. So, if λ_s is controlled, λ_{ds} will change in opposite compared with λ_{qs}. Hence, with λ_s control, the angle of the stator voltage could track the wind speed change.

The electromagnetic torque of DFIG in terms of stator flux linkage and current is shown as follows:

$$T_e = \frac{3}{2}\frac{P}{2}(\lambda_{ds} i_{qs} - \lambda_{qs} i_{ds}). \tag{6.2}$$

Considering $\lambda_{qs} = 0$, the expression of electromagnetic torque becomes

$$T_e = \frac{3}{2}\frac{P}{2}\lambda_{ds}(-\frac{M}{L_s} i_{qr}). \tag{6.3}$$

So the rotor current in q-axis is approximately proportional to the electromagnetic torque. Hence, controlling i_{qr} can help track T_e.

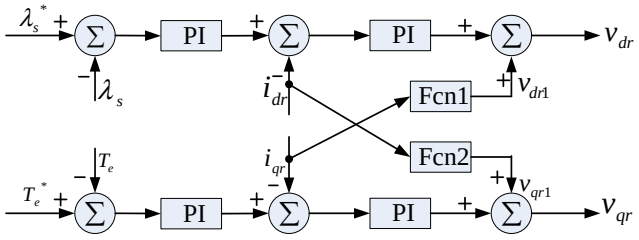

Figure 6.1. Modified control scheme for RSC.

The control scheme of GSC is shown in Fig. 6.2. It is obvious that through GSC current control, the voltage of dc-link V_{dc} could be kept constant. As shown in (3.18), the stator terminal voltage could be controlled through i_{qg}. The inner current control loop is derived from (3.19) and (3.20). The whole control loop of GSC is shown in Fig. 6.2.

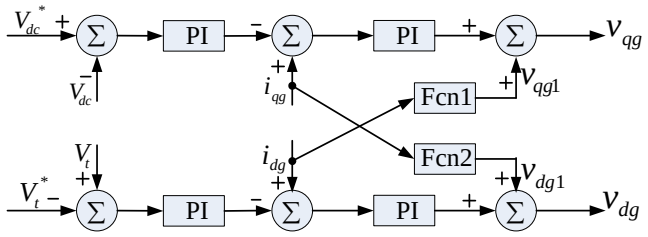

Figure 6.2. Control scheme for GSC: $v_{qg1} = v_{qs} - \omega_s L_{tg} i_{dg}$, $v_{dg1} = v_{ds} + \omega_s L_{tg} i_{qg}$.

6.2 Coordinated Control of LCC-HVDC

The coordination control philosophy of HVDC-link is to ensure cooperation of the DFIG and the HVDC-link, that is, to keep the power balance of ac/dc side as the wind speed changes. In other words, the dc voltage and dc current through the dc transmission line should increase or decrease according to the wind speed, since V_{dr} is related to the ac voltage and firing angle. On the other hand, it is desired to keep the ac voltage constant. So, a coordinated control loop is designed to adjust the firing angle of the rectifier through the bus voltage V_{ac}. The control diagram is shown in Fig. 6.3.

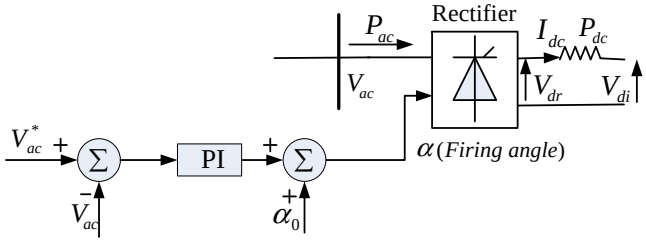

Figure 6.3. Coordinated control diagram of the HVDC-link.

As the wind speed decreases, the mechanic torque T_m will decrease. The difference between T_m and T_e becomes negative. According to the swing equation, $2H\frac{d\omega_m}{dt} = T_m - T_e$, ω_m will decrease, the operating point transfers from A to B as shown in Fig. 6.4. T_e^* is computed from MPPT (Maximum Power Point Tracking) loop and it will decline when the wind speed decreases. So, i_{qr} decreases due to the torque control loop. Since i_{qr} decreases, λ_{qs} decreases as well. Since $v_{ds} = -\omega_s \lambda_{qs}$, hence v_{ds} increases as shown in Fig. 6.5. Due to the control loop of GSC, the DFIG terminal voltage is kept constant, so v_{qs} will decrease.

As shown in Fig. 6.5, the original terminal voltage phasor is v_s; with wind speed decreases, the amplitude of the d-axis component increases, the new one is $V_s^{'}$. It is obvious that the angle δ between the stator voltage V_s and bus voltage V_{ac} will be reduced. Without changing the firing angle α, P_e ($P_e = \frac{V_s V_{ac}}{X} sin\delta$) will be kept constant, hence V_{ac} will increase if δ decreases. Based on this fact, we can design a feedback control loop shown in Fig. 6.3. When V_{ac} increases, the firing angle α increases, too; that is when the wind speed decreases, the firing angle α increases, P_{dc} decreases to achieve power balance.

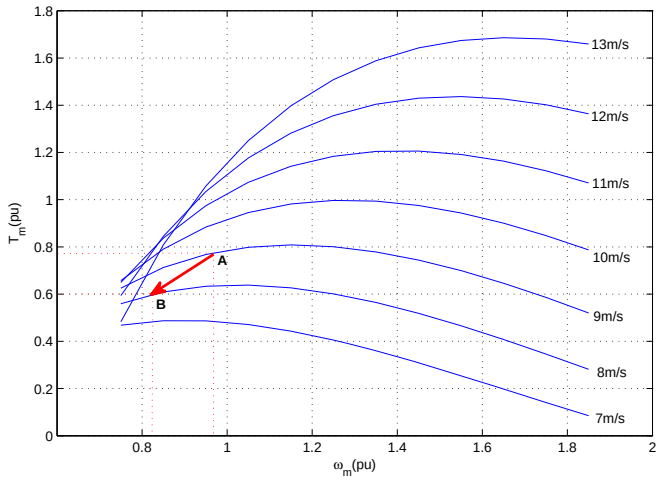

Figure 6.4. Torque-rotor speed characteristic.

6.3 Simulation Studies

6.3.1 Matlab/Simulink Test Case

Simulation studies with the proposed control design are carried out in Matlab/Simulink for an integrated 200MW wind farm with HVDC-link integration. The parameters of the DFIG and HVDC-link are given in Table 6.1 and Table 6.2.

As the wind speed decrease from 9m/s to 8m/s at 10s, Fig. 6.6 gives the plots of mechanical torque, electromagnetic torque, and rotor speed. Since the wind speed decreases, less mechanical power is generated, Tm will decrease correspondingly and ω_m will be reduced. It is obvious that the value of T_e decreases. According to the RSC control loop, i_{qr}

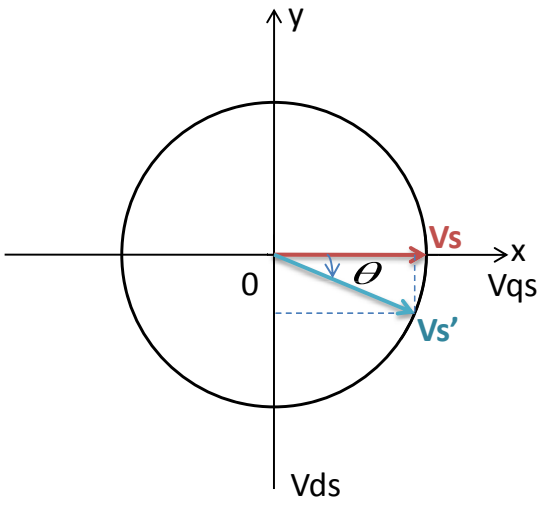

Figure 6.5. Stator voltage phasor.

Table 6.1. Parameters of the simulated DFIG

r_s (pu)	0.00488
r_r (pu)	0.00549
X_{ls} (pu)	0.09231
X_{lr} (pu)	0.09955
X_M (pu)	3.95279
H $(kg.m^2)$	3.5

Table 6.2. Parameters of the simulated HVDC-link

R (dc transmission line resistance)	$0.3595(pu)$
V_{di} (simplified receiving end of HVDC-link)	$0.5(pu)$

will decrease correspondingly. So, λ_{qs} causes the change of v_{ds}. The dynamic responses of the stator flux linkage are also shown in Fig. 6.7.

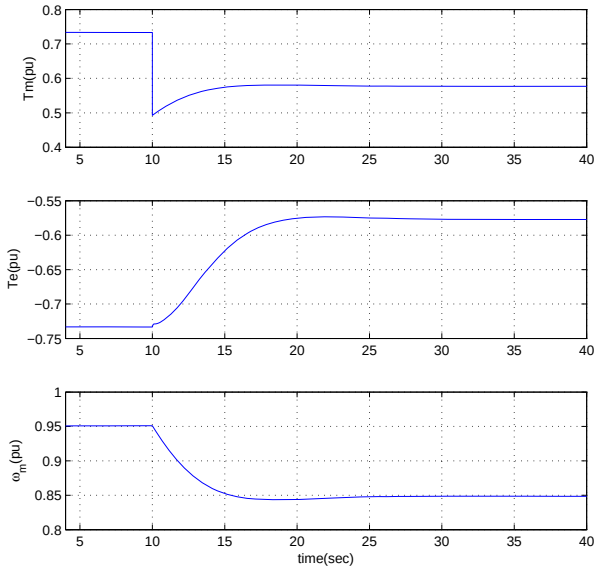

Figure 6.6. Mechanical torque (T_m), electromagnetic torque (T_e) and rotor speed (ω_m).

For comparison, simulation results of HVDC-link variables are given in two scenarios: with constant power control and coordinate control. Under constant power control, the dc current through dc transmission line will keep constant; so will dc voltage, thus constant power is kept. In this condition, the firing angle of the rectifier will increase, thus the bus voltage V_{ac} rises, so the current through ac line will decrease. The power loss P_{loss} through ac line impedance Z decreases. On the other hand, P_m declines because of the decrease of the wind speed. So P_{dc} is kept constant, the dc power of HVDC-link cannot track the variation of generated mechanical power.

With coordinated control, as the wind speed decreases, the firing angle of the rectifier increases. Since the bus voltage V_{ac} is kept constant. So the dc voltage V_{dr} and dc current I_{dc} at the sending end decrease to ensure power balance. The HVDC variables under above two scenarios are shown in Fig. 6.8 and the power relationship could also be seen in Fig. 6.9. As can be seen, under constant power control, the dc power through dc transmission

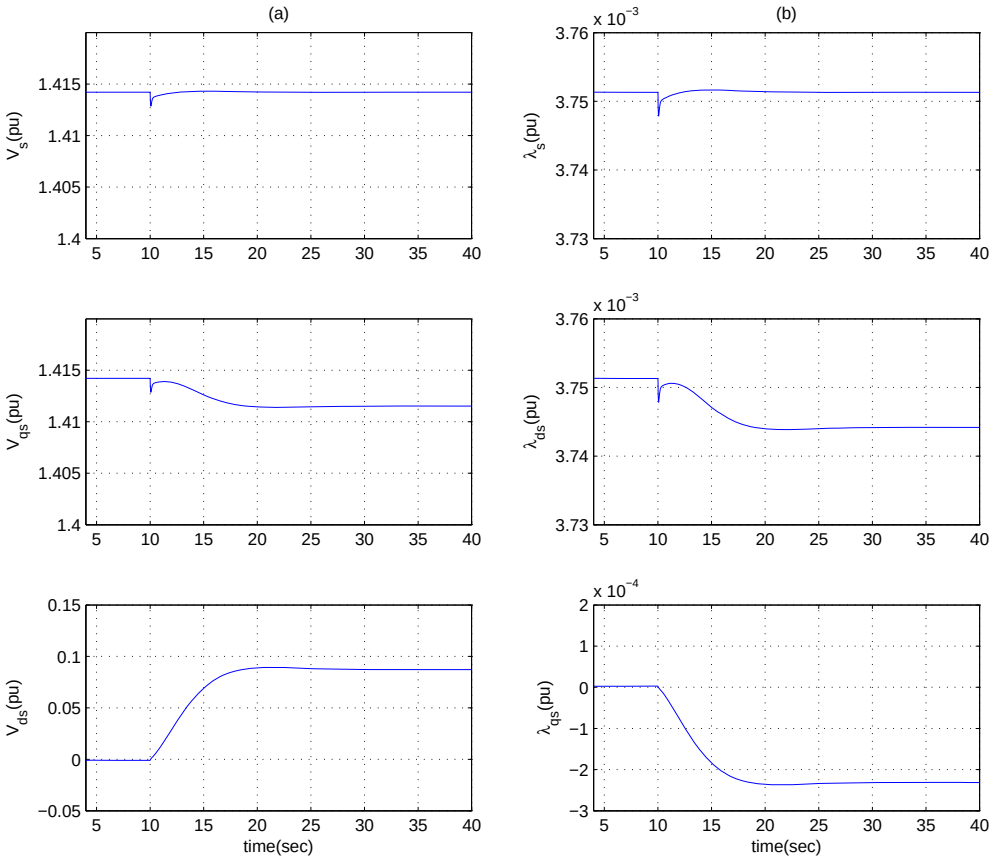

Figure 6.7. Stator voltage and flux linkage.

line cannot track the mechanical power variation. While with the coordinated control, the dc power can keep power balance. Because of some losses on the ac line resistance, dc power is less than mechanical power.

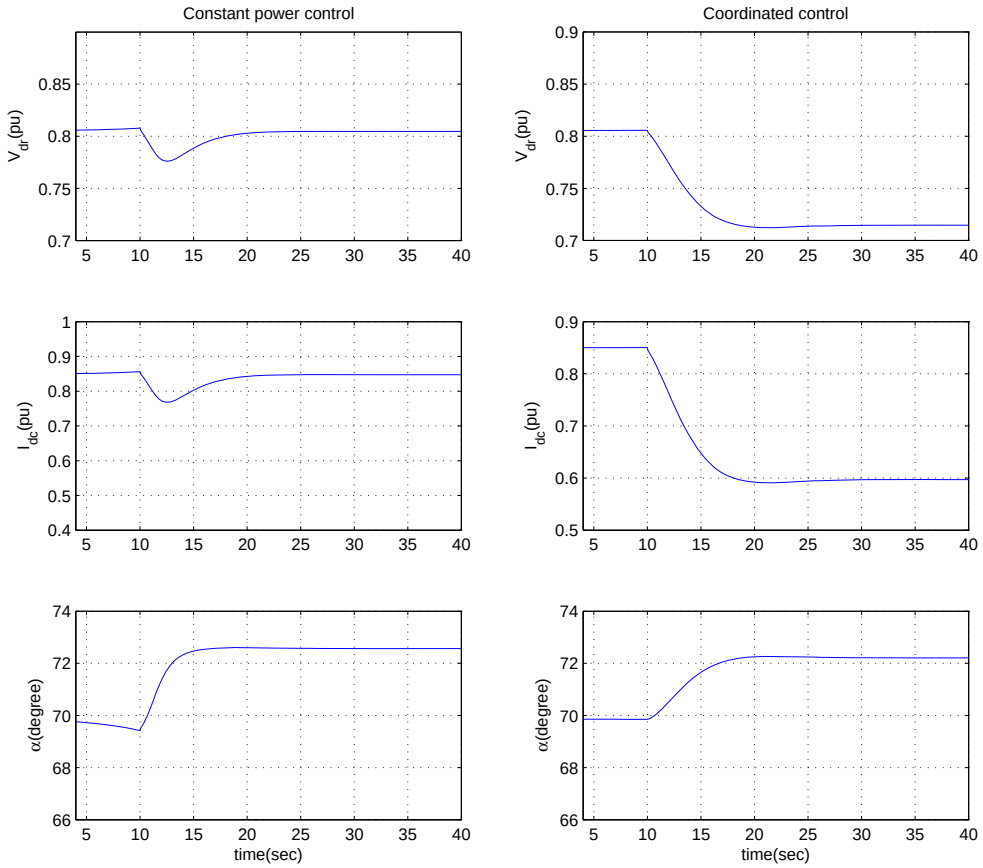

Figure 6.8. HVDC-link variables without and with coordinate control: dc voltage of HVDC rectifier (V_{dr}), dc current of HVDC (I_{dc}), firing angle of rectifier (α).

6.3.2 Matlab/SimPowerSystems Test Case

To verify the effectiveness of the proposed coordinate control strategy, a 1000MW wind farm with LCC-HVDC connection is built in Matlab/SimPowerSystems. The wind farm is an aggregate model of 666 averaged 1.5MW DFIG from the demo library with some modification. The parameters of the DFIG-based wind farm are shown in Table 6.3. The

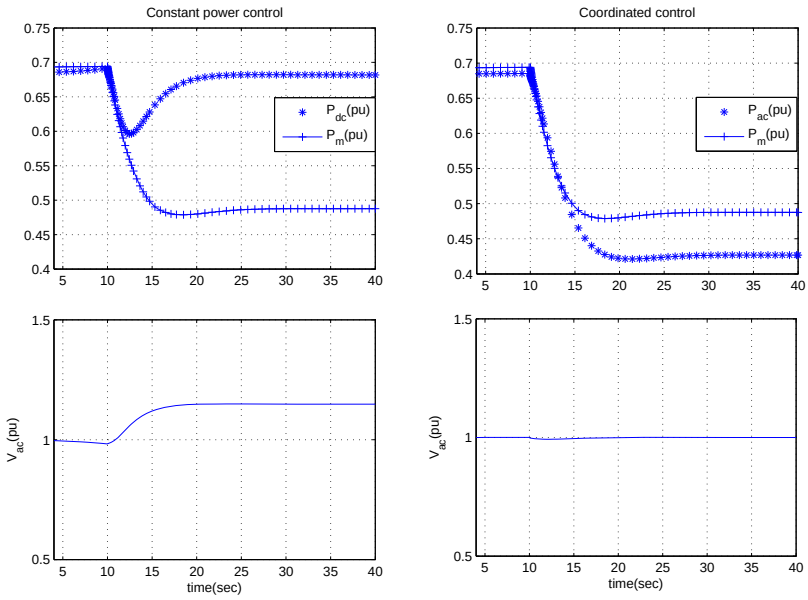

Figure 6.9. Mechanical power from wind turbine, dc power of HVDC-link and the bus voltage.

schematic diagram of the studied system can be seen as Fig. 6.10. The system frequency is 60Hz. The nominal voltage at the bus B575 is 575V. The nominal power of the wind farm step-up transformer is 1200MVA with voltage ratio 575V/500KV and the winding impedance is 0.12pu. The bus ac filters contain a capacitor bank with 150Mvar, 150Mvar double tuned low filter at the 11th/13th harmonic, 150Mvar high-pass filter at the 24th harmonic and 150Mvar C-type filter at the 3rd harmonic. The sending end of the HVDC is modeled as a 12-pulse rectifier, while the receiving end is a dc voltage source $E_0 = 500kV$. The HVDC rectifier side transformer is a three-phase transformer. Winding 1 and winding 2 connection is Y_g/Y, 500kV/200kV, the impedance is 0.0025pu. Winding 1 and winding 3 connection is Y_g/Δ, 500kV/200kV, 0.0025pu. Two vectors of 6 pulses are sent to the rectifier bridges. The pulse width of the 12-pulse generator is 40^0.

The power coefficient C_p characteristic of the studied wind turbine is shown in Fig. 6.11. With the pitch angle increasing by step of 2 degrees, the maximum C_p will decrease. When the wind speed is low, the pitch angle is set as 0, at this point, the maximum C_p is

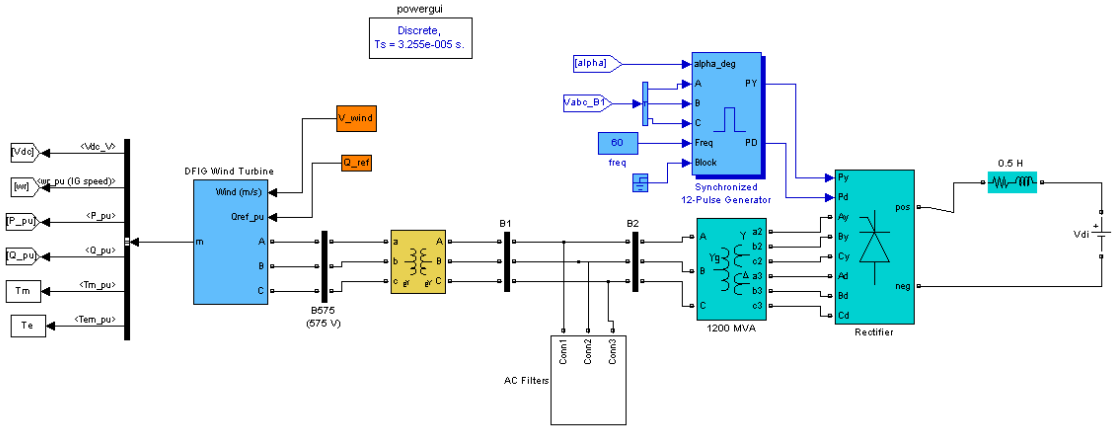

Figure 6.10. Schematic diagram of a wind farm with LCC-HVDC connection in Matlab/SimPowerSystems.

Table 6.3. Parameters of the DFIG wind farm

Total capacity	666*1.5MW
Nominal voltage	575V
Frequency	60Hz
r_s (pu)	0.023
r_r (pu)	0.18
X_{ls} (pu)	0.016
X_{lr} (pu)	0.16
X_M (pu)	2.9
H $(kg.m^2)$	0.685
F (pu)	0.01
p (poles)	3

about 0.5. When the wind speed is very high, the output power can be limited through the increased pitch angle.

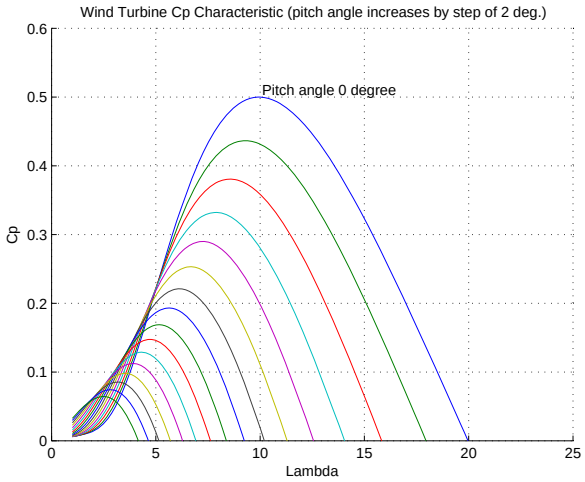

Figure 6.11. Power coefficient C_p characteristic of the wind turbine.

Detailed wind turbine characteristics are shown in Fig. 6.12. Under nominal rotor speed (1.2pu), the dynamics of the output power P, tip speed ratio Lambda and power coefficient C_p are presented. As can be seen, as the wind speed increases, the P increases, and Lambda decreases.

The dynamic response of the DFIG variables and HVDC link variables are monitored when the wind speed decreases from 15m/s to 10m/s at 15s. Dynamic responses of the mechanical torque, electromagnetic torque and rotating speed are shown in Fig. 6.13. As the wind speed decreases, the mechanical torque T_m decreases as well. According to the swing equation, the rotor speed ω_m will be reduced. Finally, the electromagnetic torque T_e decreases to achieve a new operating point.

The modified RSC control keeps the flux linkage constant as shown in Fig. 6.14. On the other hand, the rectifier of HVDC controls the ac side voltage V_{ac}. During steady-state, $V_{ac} = \lambda_s \omega_s$, hence, the grid frequency ω_s is well controlled at 60 Hz. The dynamic response of HVDC variables are also given in Fig. 6.15. The dc current I_{dc} decrease from 1pu to about 0.5pu as the wind speed decreases from 15m/s to 10m/s. Due to the voltage control

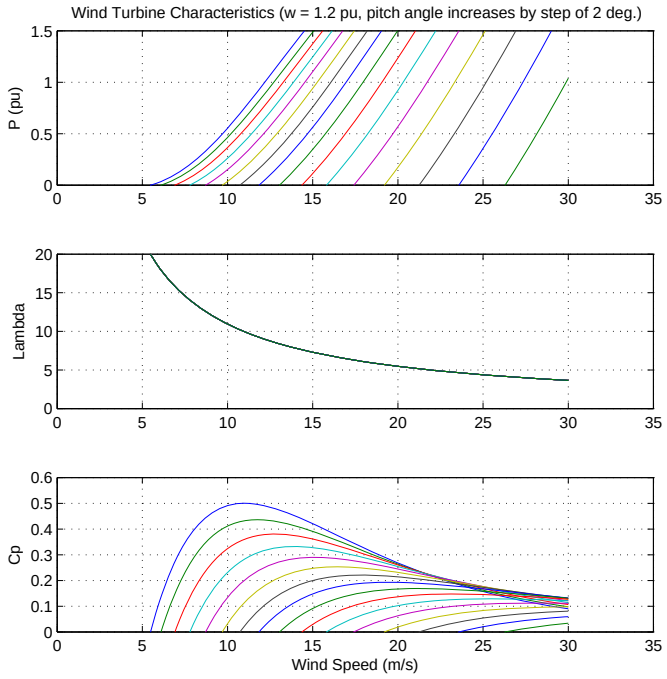

Figure 6.12. Wind turbine characteristics.

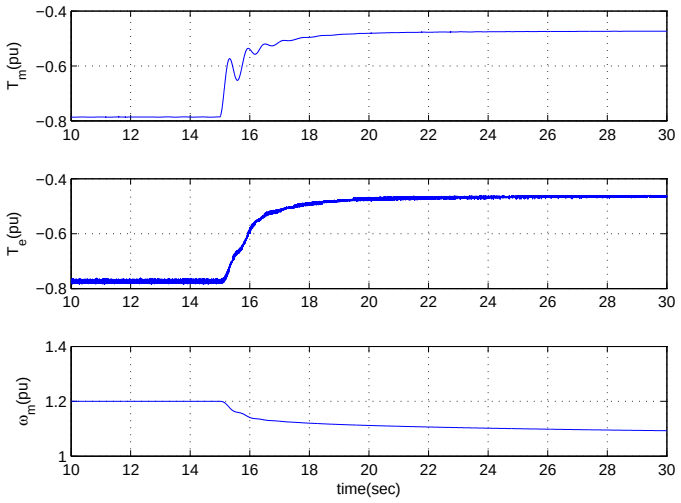

Figure 6.13. Dynamic responses of the mechanical torque (T_m), electromagnetic torque (T_e) and rotating speed (ω_m)(the wind speed decreases from 15m/s to 10m/s at 15s).

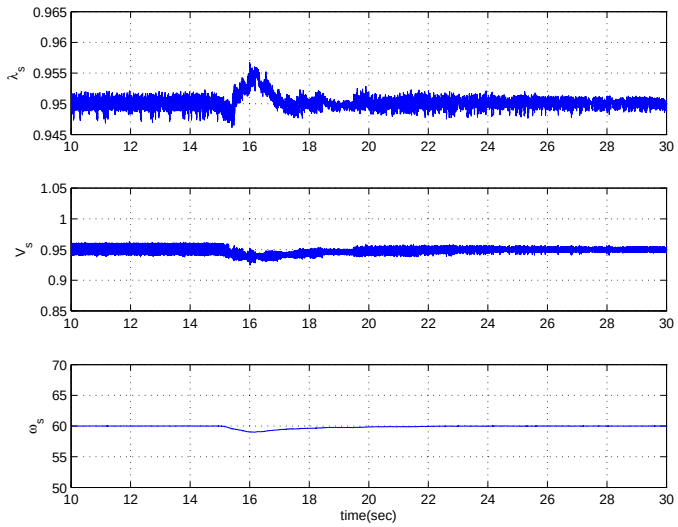

Figure 6.14. Dynamic responses of the stator flux, grid voltage and grid frequency (the wind speed decreases from 15m/s to 10m/s at 15s).

of the rectifier, the firing angle is adjusted under different wind speeds. Here, the firing angle increases from 20 degrees to about 24 degrees.

To verify the power balance capability of the proposed coordination method, power from the wind farm and dc power through dc transmission line are compared in Fig. 6.16. Previously, the output power from wind farm was about 1000MW when the wind speed is 15m/s. When the wind speed decreases to 10m/s, the dc power tracks the power well. Due to the switching operation of the rectifier, the dc power has characteristic harmonics.

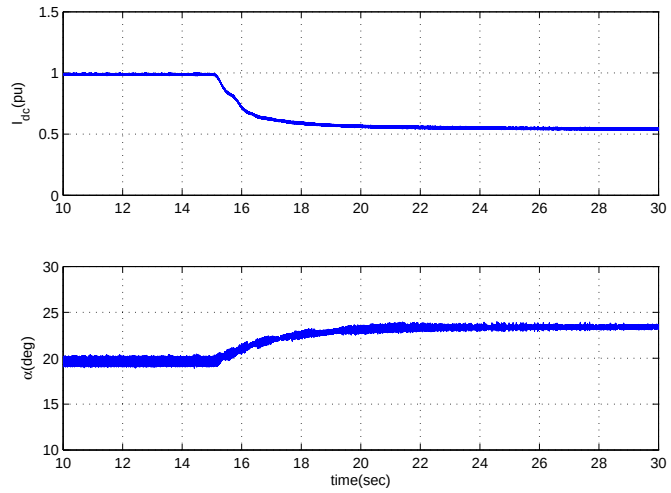

Figure 6.15. Dynamic responses of the HVDC variables: the dc current and firing angle (the wind speed decreases from 15m/s to 10m/s at 15s).

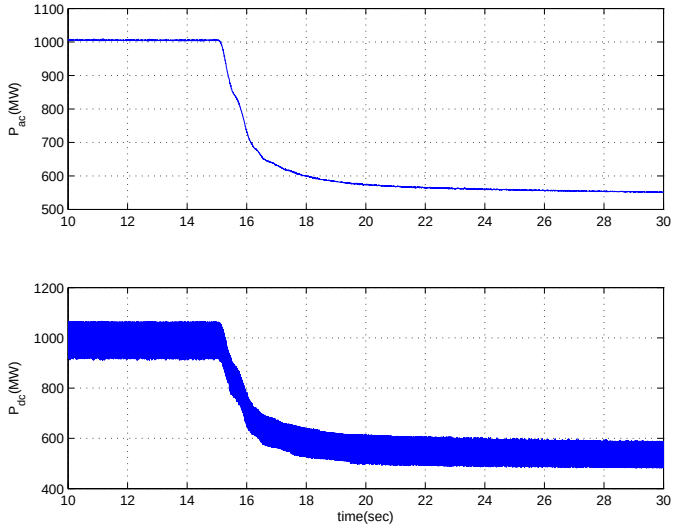

Figure 6.16. Dynamic responses of the generated ac power from the wind farm and the dc power transmitted by HVDC-link (the wind speed decreases from 15m/s to 10m/s at 15s).

CHAPTER 7

FAST POWER ROUTING THROUGH HVDC

7.1 Introduction

Fast power routing capability is the most desirable for future grids with a high penetration of renewable energy resources such as wind and solar. Due to their intermittent nature, power flow patterns in future grids will experience fluctuations more often. This poses challenges in system operation to manage congestion in a high speed manner. Flexible AC Transmission Systems (FACTS) and HVDC are two enabling technologies with fast power routing capabilities. HVDC has been an option to interconnect wind farms to ac grids [40, 13, 17]. There are currently voltage source converter (VSC)-HVDC for mid-voltage level transmissions [42] and LCC-HVDC for high-voltage level transmissions [15].

The objective of this chapter is to investigate the fast power routing capability of LCC-HVDC since LCC-HVDC is a mature technology in high power, high voltage transmission and has been used world-wide. Traditionally, LCC-HVDC is equipped with power order control at its rectifier side. Power delivered through HVDC can be scheduled. This research aims to examine a new way to enable fast power routing by HVDC. Power order control does not suit this aim since the power flow patterns keep changing and the power order should keep changing with them. Communication links are required to send the varying power order from wind farms to HVDC links. Additional computing time and communication time are needed. An HVDC is expected to respond quickly. Therefore, an automatic control using local measurements is expected.

The concept of infinite bus is implemented in designing this kind of automatic control. An infinite bus can absorb or generate whatever power the rest of the system needs. To emulate an infinite bus, the ac bus at the rectifier side of an HVDC should be controlled to have a constant voltage. Therefore, a voltage order control should replace the traditional power order control to realize fast power routing capability.

Compared with the existing literature on HVDC and wind farm power coordination, the aforementioned approach has the following advantages:

1. The control does not rely on additional devices such as STATCOM. STATCOM converters are used for wind farms with HVDC delivery to provide reactive power [14, 50, 80, 51]. The dc-link voltage of a STATCOM reflects the power unbalance between wind farms and an HVDC link. Hence the dc-link voltage is used as a feedback signal to adjust the HVDC rectifier current order. Here, since a hybrid ac/dc system is the study objective, a synchronous source is presented at the wind farm side. Therefore, STATCOM is not needed and none of its measurements is available for controls.

2. No change is required at the DFIG control side. In [49, 16], power balance between a DFIG wind farm and an HVDC is realized through frequency control. A frequency control is applied to give a current order in the rectifier control. Changes have to be made at DFIG controls. Instead of real/reactive power control, stator flux control is adopted.

7.2 Study System

The studied system is shown in Fig. 7.1. It consists of a 1000 MW synchronous generator, a 510 MW wind farm and an LCC-HVDC with a rated power at 1000 MW. The system is built in Matlab/SimPowerSystems [81]. The HVDC link and the synchronous generator are built based on the models from SimPowerSystems examples. A 1.5 MW DFIG is scaled up to represent a 510 MW DFIG wind farm. Power from the synchronous

generator and the wind farm is transmitted to a 50 HZ grid through an LCC-HVDC connection. AC filters on the two terminals of the HVDC are applied to eliminate the harmonics in the ac currents. They can also provide reactive power for HVDC converters. The size of the ac filter at both converter sides is 600 MVar including 150 MVar from a shunt capacitor, 150 MVar from an 11th harmonic filter, 150 MVar from a 13th harmonic filter and 150 MVar from a 24th harmonic filter. The HVDC is a 1000 MW (500 kV, 2 kA) dc link. The converters of HVDC are connected through a 300 km transmission line. Detailed parameters of the DFIG, synchronous generator, HVDC and transformers can be referred to in SimPowerSystems user's guide [81].

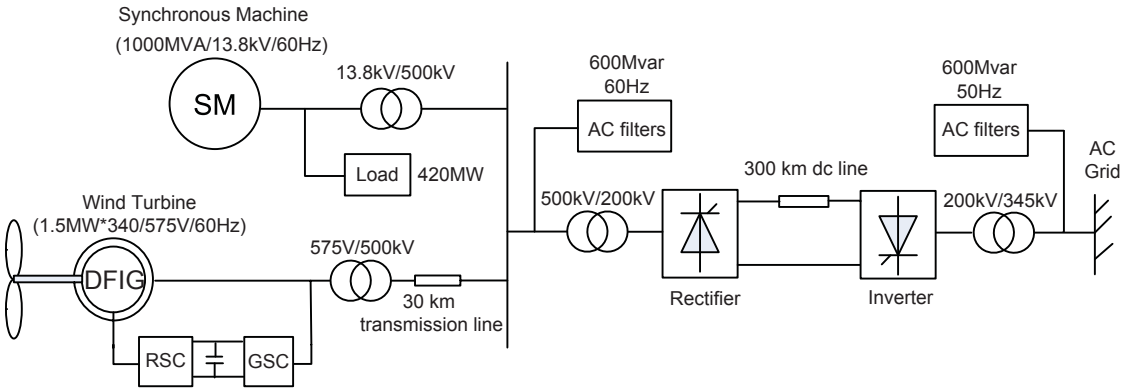

Figure 7.1. Study system.

7.2.1 Turbine-Governor Model of the Synchronous Generator

The schematic diagram of the turbine-governor model of the synchronous generator is shown in Fig. 7.2 [82]. It consists of a hydraulic turbine, a second-order servomotor system and power/frequency controls. $\Delta\omega$ is the speed deviation of the speed measurement with respect to the nominal value. The input of the PID controller is the sum of the speed error signal and the power error multiplied by a droop (5%). The output of the PID controller drives the servo motor to change the valve position of the hydraulic turbine. As the result of the power/frequency control, the synchronous generator can adjust its exporting power based on the frequency deviation and the power order.

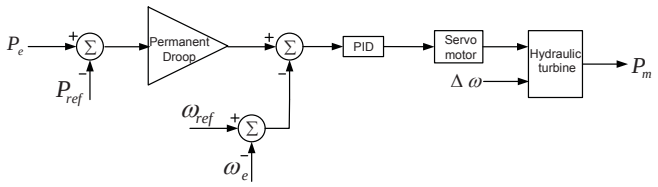

Figure 7.2. Turbine-governor.

7.2.2 Wind Turbine

A 9 MW wind farm model is included in an example of SimPowerSystems. For this project, the 9 MW wind farm model is scaled up to represent 340 DFIG wind turbines each at 1.5 MW. The wind farm is operated at maximum power point tracking mode when the wind speed is less than nominal. When the wind speed is above rated speed, pitch angle control will regulate the aerodynamic torque. In such conditions, the mechanical power is reduced to the rating (1 pu) through adjusting the pitch angle. A typical structure of pitch angle controller is shown in Fig. 7.3 [38]. The pitch angle is determined by the input variables: the rotor speed and the electric power.

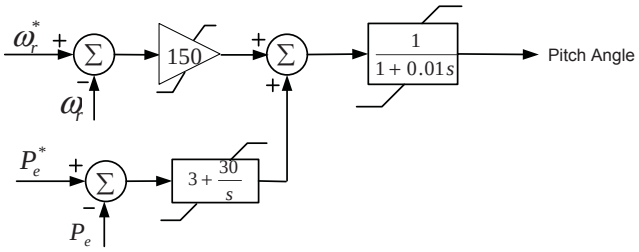

Figure 7.3. Wind turbine pitch angle controller.

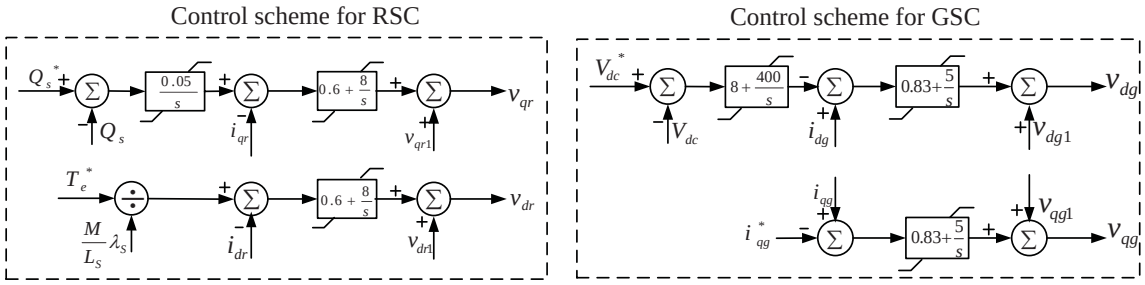

Figure 7.4. Control scheme for RSC and GSC.

7.2.3 Control of RSC and GSC

The control objectives of the RSC are to regulate the electromagnetic torque and the stator reactive power. The torque order is obtained from maximum power point tracking. There are two cascaded control loops: the inner loop is current control and the outer loop is power control. The rotor current component i_{dr} can be regulated through the electromagnetic torque T_e (P_s/ω) divided by λ_s. On the other hand, the d-axis component i_{qr} can be regulated through the stator reactive power Q_s. Hence, the outer power control loop can be designed to get the reference value of the rotor current. Through the GSC control, the dc voltage of the dc-link between the RSC and the GSC can be kept constant. The reactive power generated by the GSC could also be regulated. The RSC and GSC control loops are shown in Fig. 7.4, and $v_{qr1} = -\omega_{slip}\sigma L_r i_{dr}$, $v_{dr1} = -\omega_{slip}(\sigma L_r i_{qr} + M/L_s\lambda_s)$, $v_{qg1} = v_{qs} - \omega_s L_{tg} i_{dg}$, $v_{dg1} = v_{ds} + \omega_s L_{tg} i_{qg}$.

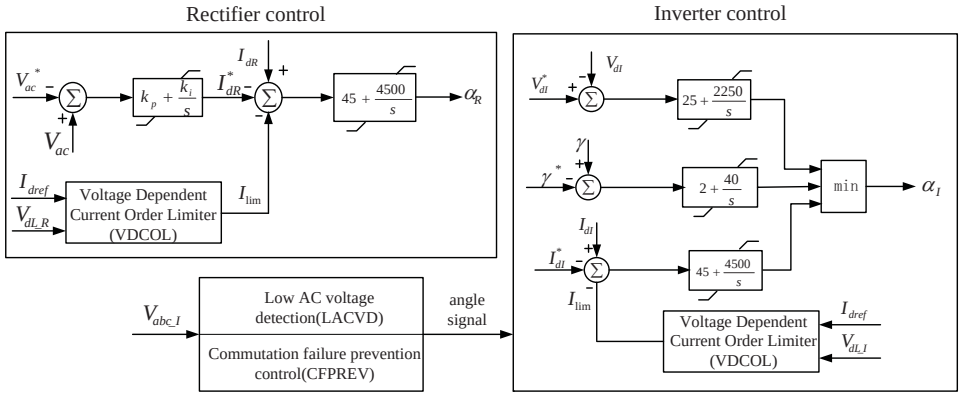

Figure 7.5. Control scheme for HVDC.

7.3 HVDC Control

The control diagram of the HVDC is shown in Fig. 7.5. Controls are implemented for both the rectifier and the inverter. For inverter control, there are three types of modes: constant dc voltage, constant extinction angle and constant dc current. PI controllers are implemented to regulate dc voltage, extinction angle or dc current. A voltage dependent current limiter (VDCL) will be enforced when the dc voltage drops due to disturbances

[2, 15]. For this study system, the HVDC inverter is operated at the constant voltage control mode at normal operating conditions.

The rectifier is normally operated at the constant current control mode where the dc current measurement is compared with a dc current order to generate the desired firing angle. In traditional HVDC rectifier control, this current order is generated by the dc power order divided by the dc voltage.

Here, a new rectifier control is proposed to realize fast power routing.

7.3.1 Proposed HVDC Rectifier Voltage Control

Compared with the conventional power control at the rectifier, the proposed control uses voltage control to generate dc current reference. The rms value of the ac voltage at the rectifier is measured and compared with a reference ac voltage V_{ac}^{*}. The error is sent to a PI controller to generate a dc current order I_{dR}^{*}. A positive feedback control is implemented for the voltage control in Fig. 7.5. Justification of the positive feedback control is presented as follows.

For the study system, a simplified circuit model is presented in Fig. 7.6. The synchronous generator is simplified as a voltage source V_G behind an impedance Z_G, while the aggregated wind farm is considered as a current source I_{WF} behind an impedance Z_{WF}. The HVDC could be simplified as a current source I_{HVDC}. The voltage at V_{ac} could be expressed as:

$$\frac{V_{ac}}{Z_G} = \frac{V_G}{Z_G} + I_{WF} - I_{HVDC}. \tag{7.1}$$

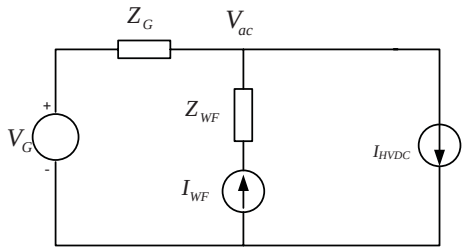

Figure 7.6. Circuit representation of the study system.

As the wind speed increases, I_{WF} will be raised. From the above expression, V_{ac} will increase correspondingly. Power and current through the HVDC are expected to increase to absorb wind energy. Hence a positive feedback is reasonable. When V_{ac} increases, the current order also increases. In turn, the firing angle will be reduced according to the control diagram. The power and the dc current delivered through the HVDC will then increase. The ac current flowing into the HVDC I_{HVDC} in turn will be increased. Consequently V_{ac} will reduce based on equation 7.1 and finally match its reference value.

7.4 Simulation Studies

To demonstrate the power routing capability of the HVDC, simulation studies are carried out in Matlab/SimPowerSystems [81]. The study system is shown in Fig. 7.1. The synchronous generator supplies power to the HVDC (at about 500 MW) and the local load (420 MW). The DFIG-based wind farm is an aggregated system rated at 510 MW. Four case studies are designed. Case study 1 tests the voltage control step response. Case study 2 tests HVDC's fast power routing capability when the wind speed changes. Case study 3 tests HVDC's fast power routing capability when there is a change in loads and when the synchronous generator picks up the load change. Case study 4 tests ac fault recovery of the HVDC system.

7.4.1 Case Study 1: Step Response of V_{ac} Setting

In this case, the reference value of the ac voltage V_{ac}^{*} is assumed to decrease from 0.985 pu to 0.95 pu at $t = 15s$. The voltage controller parameters are as follows: $K_p = 0.2$ and $K_i = 3.2$. Due to the positive feedback control, the dc current of the HVDC will increase and the firing angle will decrease. Power through HVDC will increase too (about 50 MW). Fig. 7.7 shows power from the synchronous generator, the DFIG-based wind farm and power through HVDC. The response time for the HVDC is only about 1 second. Due to the power control enforced in the wind farm, power from the wind farm varies

insignificantly. The ac grid should experience a frequency decrease and the synchronous generator generates more power to match the HVDC power increase.

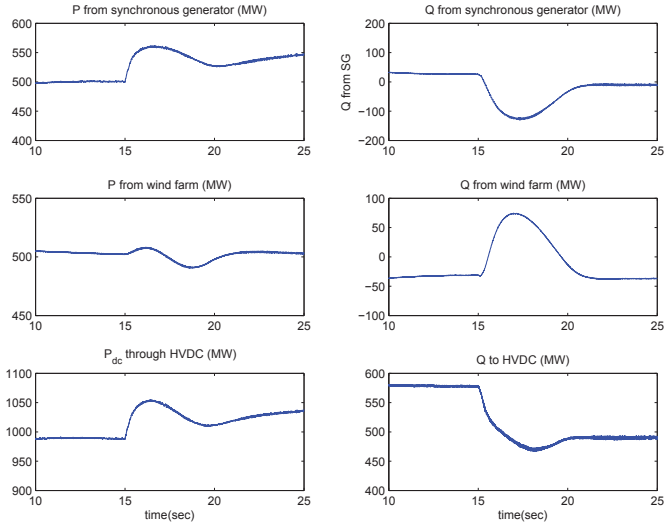

Figure 7.7. Dynamic responses in active and reactive power due to a step response in V_{ac}^{*}.

The reactive power absorbed by the HVDC rectifier reduces due to a decrease in the firing angle ($Q \propto \sin\alpha$). Reactive power from the wind farm is tightly controlled and does not vary at steady-state. The reduction of the absorbed reactive power by the HVDC rectifier is due to the reduction of reactive power generated from the synchronous generator and the reduction of reactive power supplied from the filters.

The dynamic responses of the rectifier and inverter variables are shown in Fig. 7.8. The dc currents increase and the rectifier firing angle decreases due to the step response. The relationship of the dc voltage and current is shown in Fig. 7.9. The inverter is at constant voltage control. While the original operating condition is at point A, due to the increase of the dc current, the operating point moves to B. Inverter dc voltage levels at A and B are kept the same. Extinction angle γ will decrease when the operating point moves from A to B. Hence in Fig. 7.8, we can also observe that γ decreases due to a reduction in the ac voltage reference value.

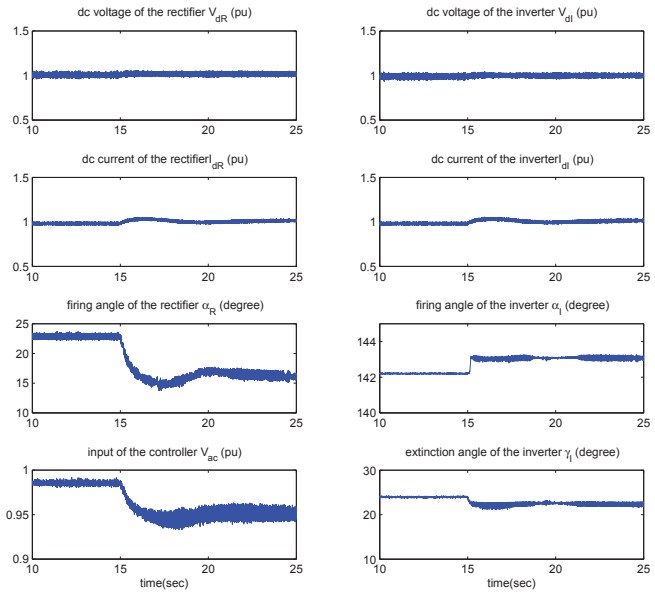

Figure 7.8. Dynamic responses of the HVDC system due to a step response in V_{ac}^{*}.

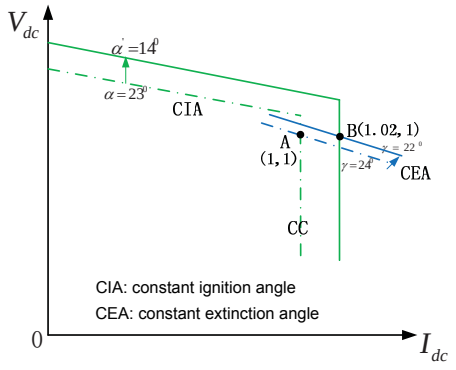

Figure 7.9. V-I characteristics of the HVDC.

7.4.2 Case Study 2: Wind Speed Change

A varying wind speed is the main characteristic of wind energy. In this case, the power routing capability of HVDC is tested for a varying wind speed. The voltage controller is the key for the HVDC to pick up power change under different wind speeds. However, different PI parameter settings can affect the power sharing of the DFIG, the synchronous generator and the HVDC. When the time constant of the voltage controller is small, the HVDC will pick up all the power change when the wind speed changes. When the time constant of the PI controller is large, the synchronous generator and HVDC will share the power change. Fig. 7.10 shows the comparison of two cases with different time constants. In (a), the parameters are $K_p = 0.5$, $K_i = 0.9$, and the time constant $\tau = 0.56$. The synchronous generator and the HVDC will pick up the power change from the DFIG together. The share of the synchronous generator is about 15 MW. In (b), $K_p = 0.2$, $K_i = 3.2$, and the time constant $\tau = 0.0625$. The HVDC acts fast enough to pick up all the power change from the wind farm.

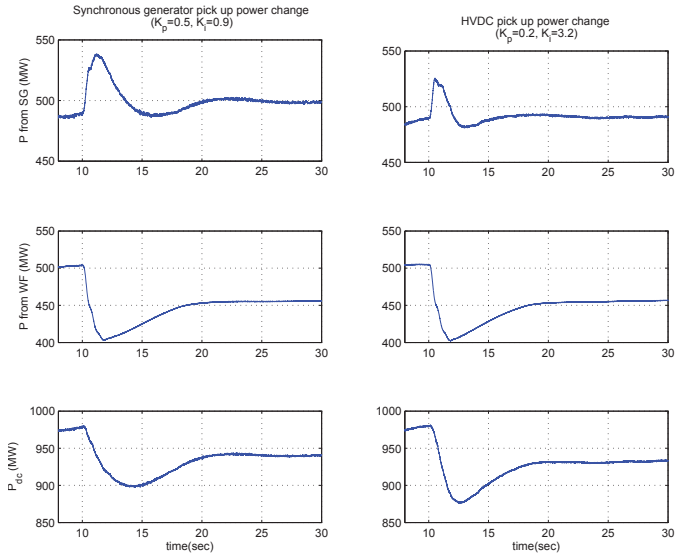

Figure 7.10. Dynamic responses of active power from synchronous generator, DFIG and through HVDC due to a change in wind speed under different PI controller settings.

A more complicated case is presented as follows. The chosen controller parameters are $K_p = 0.2$, $K_i = 3.2$. The wind speed drops from 15 m/s to 12 m/s at 10 seconds. It then increases from 12 m/s to 17 m/s at 20 seconds. Dynamic responses of the power from the generator, the wind farm and through the HVDC are given in Fig. 7.11. The generator speed and the mechanical power are shown in Fig 7.12. The input variable V_{ac} and output variable I_{dref} of the controller are shown in Fig. 7.12. The HVDC variables are shown in Fig. 7.13 and the DFIG system variables are shown in Fig. 7.14.

It is found that the HVDC can pick up the wind power change while the synchronous generator will experience transients. This is due to transients in frequency and the corresponding turbine-governor responses. The rectifier firing angle will increase due to a reduction in wind speed and decrease due to an increase in wind speed. The DFIG pitch angle will become zero when the wind speed reduces below the synchronous speed.

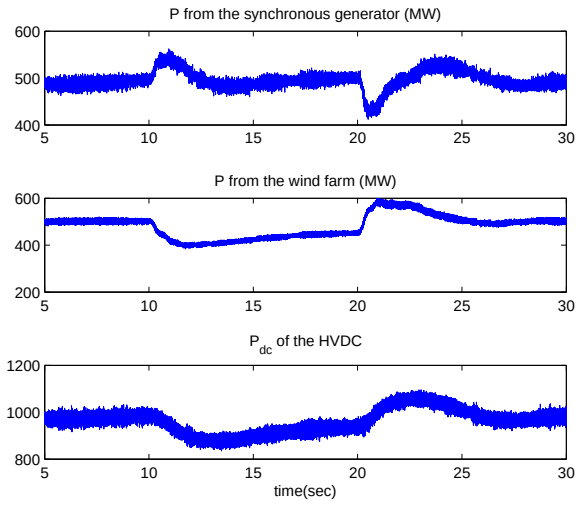

Figure 7.11. Dynamic responses of the real power from the synchronous generator (excluding the load), the wind farm and through the HVDC due to wind speed changes.

7.4.3 Case Study 3: Load Change

In case study 3, the load increases from 420 MW to 520 MW at 10s. The HVDC picks up the load change immediately since the response of the HVDC is faster than the

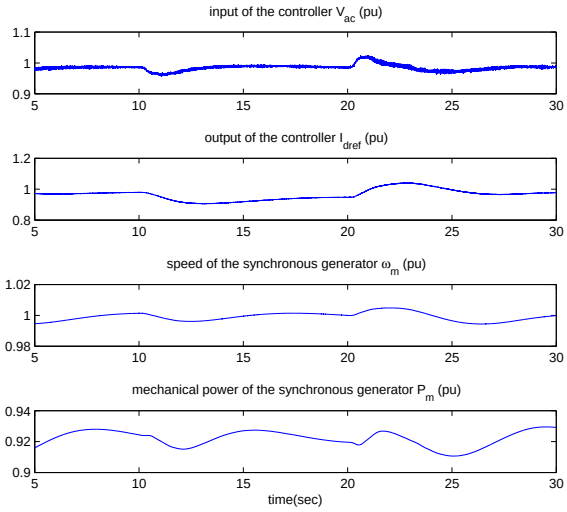

Figure 7.12. Dynamic responses of the voltage controller and the turbine governor due to wind speed changes.

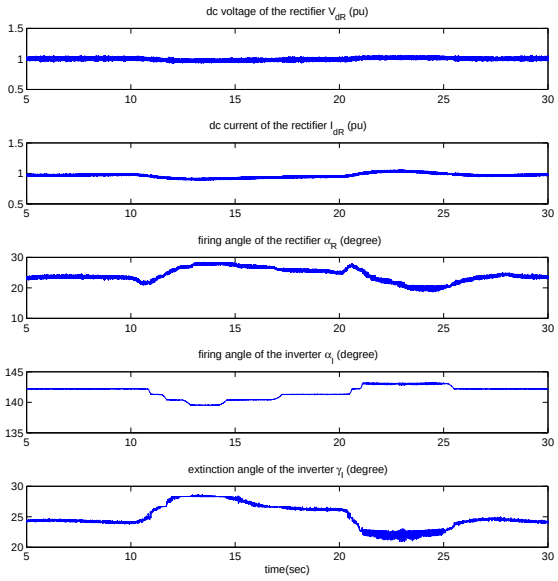

Figure 7.13. Dynamic responses of the HVDC due to wind speed changes.

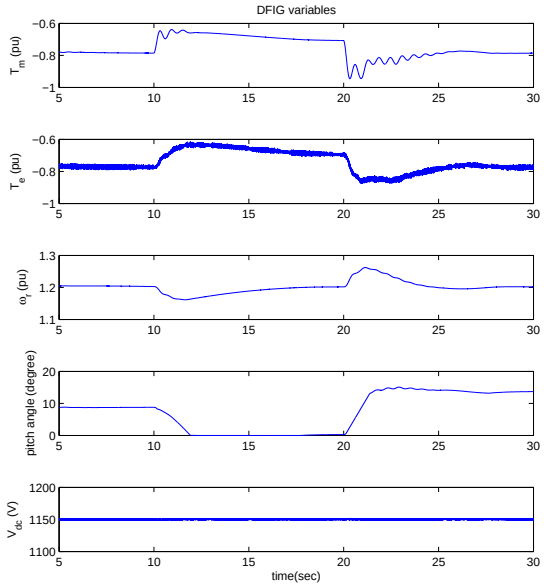

Figure 7.14. Dynamic responses of the DFIG wind farm due to wind speed changes.

synchronous generator. Due to the slow turbine governor response, a change in the reference power P_{ref} will be reflected in the generator power after about 30 seconds. In order to show the HVDC response in this simulation case, the mechanical power of the synchronous generator is assumed to have an increase of 100 MW at 15 seconds. The synchronous generator will increase its power output to pick up the load change. Consequently, the dc power will be reduced to its original level. Dynamic responses of the system are shown in Figs. 7.15 and 7.16.

The synchronous generator speed will decrease when the load increases and will increase when the synchronous generator increases its output power. Increased load however affects the system voltage level. V_{ac} will decrease. This in turn will trigger the voltage controller to decrease the dc current order and increase the firing angle. When the synchronous generator starts to pick up the load increase, the voltage level increases. The HVDC system will then ramp up its transporting power through decreasing the rectifier firing angle α.

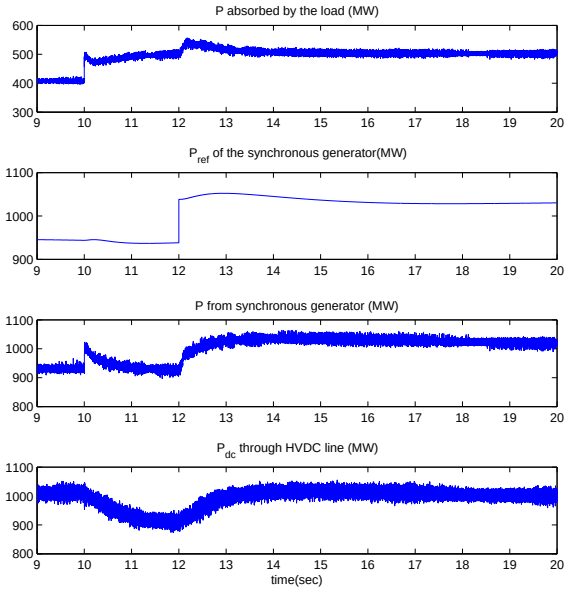

Figure 7.15. Dynamic responses of the active power from synchronous generator, load, DFIG and through HVDC due to load change.

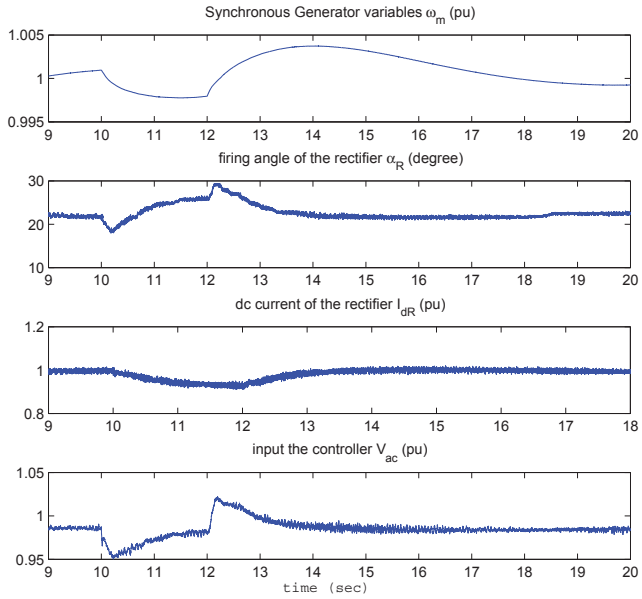

Figure 7.16. Dynamic responses of the generator speed, firing angle, dc voltage and V_{ac} due to load change.

7.4.4 Case Study 4: AC Fault Recovery

The operation of an HVDC is often affected by disturbances such as faults in the ac system. In case study 4, a single-line-to-ground (S-L-G) fault on the inverter ac system is studied. A S-L-G fault is applied on phase A at 10 s, and is cleared at 10.1 s. The fault will cause the reduction of the ac voltage and rise of the dc current as shown in Fig. 7.17. Due to the failure of the commutation from one valve to another before the commutating voltage reverses, commutation failure occurs at the very beginning of the fault. The commutation failure will lead to a short circuit across the valve group. The dc power is almost zero as shown in Fig. 7.18. After the fault is cleared, the system returns to normal operation after about 0.2 s.

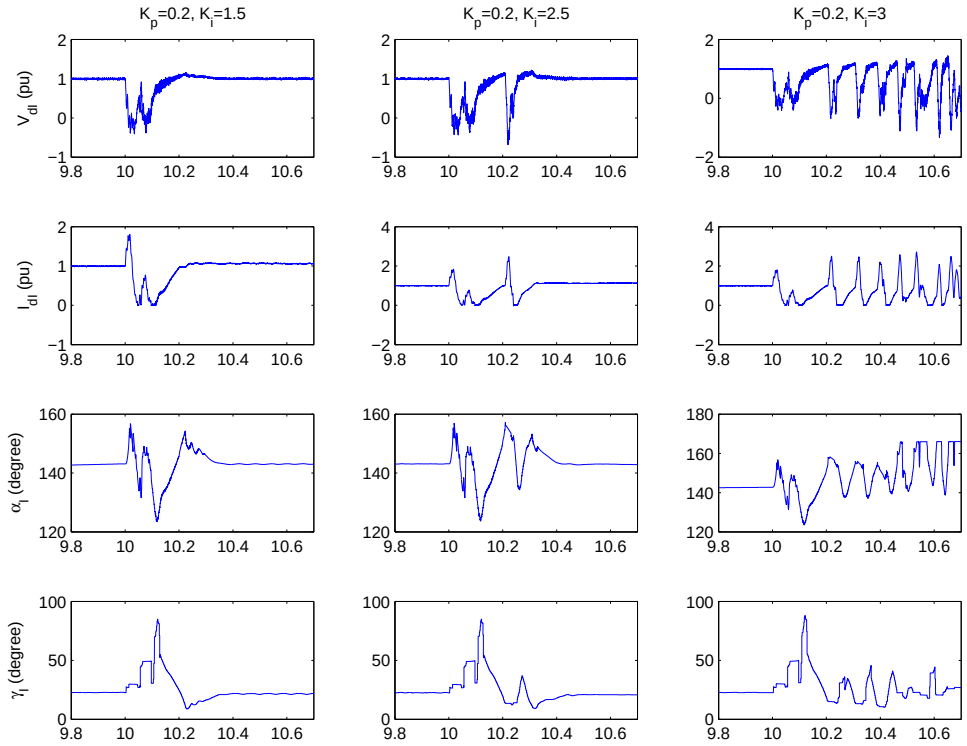

Figure 7.17. Dynamics of the inverter variables during A-L-G fault at the inverter side.

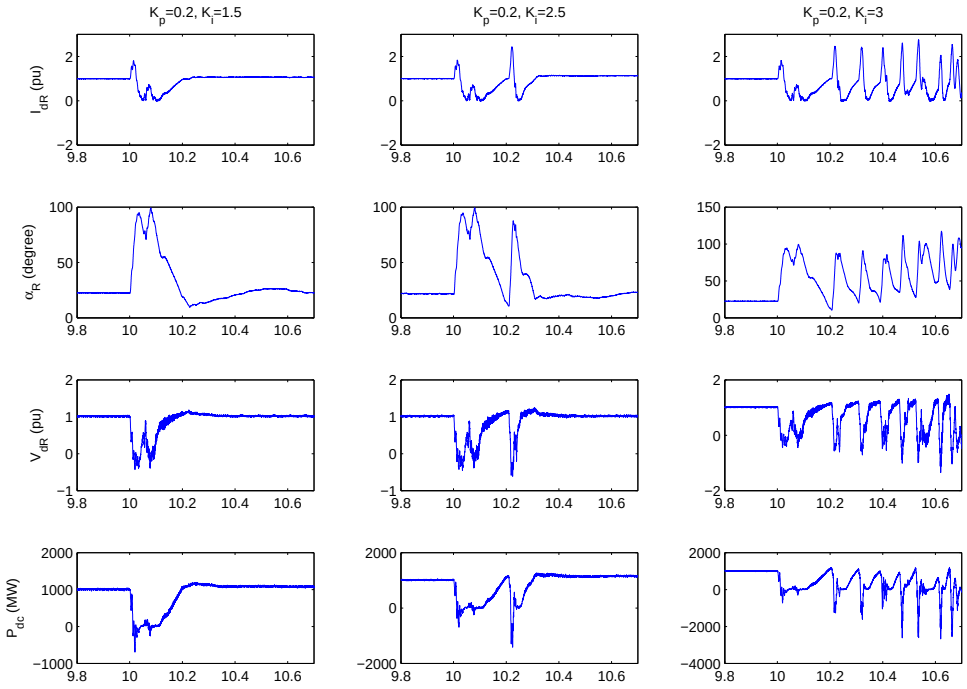

Figure 7.18. Dynamics of the rectifier variables during A-L-G fault at the inverter side.

As shown in case study 2, the parameters of the voltage control affect system dynamics. The impact of the PI parameters on ac fault recovery performance is also studied. If the integration constant K_i increases, the settling time of the system will increase [83]. Therefore, the dynamics of the dc current and firing angle of the rectifier will be affected under different integration constants. Figs. 7.17 and 7.18 show that when $K_i = 3$, the system cannot recover after the fault clearance. Therefore, the two other two sets of parameters $K_p = 0.2/K_i = 1.5$ and $K_p = 0.2/K_i = 2$ are better in terms of ac fault recovery.

In case study 2, a smaller time constant is demonstrated to be good for HVDC to do the fast power routing task. However, Case Study 4 shows that a smaller time constant for the PI controller may cause ac fault recovery problems. Therefore, the controller parameters have to be chosen and verified through various studies.

CHAPTER 8

REACTIVE POWER COORDINATION

This chapter has been published in Energytech 2011 and appears in this dissertation with IEEE's permission.

In Chapter 6, coordination between HVDC and DFIG-based wind farm considers active power coordination only [49]. The assumption here is that there is enough reactive power from the DFIG and the filter. DFIG wind farms however have limited capability in supplying reactive power. The capability is discussed in [53, 52, 54]. The goal of this chapter is to coordinate active power from a wind farm and the active power transported by the HVDC while considering the limiting factors of reactive power. A preliminary work [84] by the authors on active power coordination without considering any limiting factor has been published. In [84], the rectifier side ac voltage is controlled to be constant. The HVDC rectifier converter can be viewed as a voltage source in such control mode. Consequently, it can absorb whatever wind power is harvested.

Here, limiting factors such as reactive power will be taken into consideration. Since reactive power and voltage level are closely related, the limits of the reference voltage at HVDC rectifier converters will be investigated. As the first step of this research, an assumption is made that only DFIG's reactive power capability is considered while the ac filter's capability is not considered. The evaluation made in this chapter is thus more conservative than the practical case.

For reactive power coordination between DFIG and LCC-HVDC, the reactive power capability of DFIG should be given first. To make sure DFIG can always supply reactive power for LCC-HVDC as wind speed increases, the specific range of the rectifier ac bus voltage will be investigated. To make sure DFIG will work within its active/reactive power

operation region, a lower limit of the rectifier ac bus voltage is found. Furthermore, as the wind speed increases, the reactive power may not satisfy the reactive power requirements of LCC-HVDC, an upper limit of the ac bus voltage is also found.

8.1 Active and Reactive Power Characteristics of DFIG

The total active power of DFIG should be the sum of stator active power P_s and rotor active power P_r. The rotor active power P_r depends on the slip s of the induction machine. Usually the GSC works at unit power factor, therefore the total apparent power is the sum of stator apparent power and the active power from RSC or GSC. The total active power P_t and reactive power Q_t from DFIG can be obtained as follows [53]:

$$P_t = (1-s)\frac{X_M}{X_s}V_s cos(\theta) \tag{8.1}$$

$$Q_t = \frac{X_M}{X_s}V_s sin(\theta) - \frac{V_s^2}{X_s} \tag{8.2}$$

where $\bar{V}_s = V_s\angle 0$, and $\bar{I}_r = I_r\angle -\theta$.

Then

$$(\frac{P_t}{1-s})^2 + (Q_t + \frac{V_s^2}{X_s})^2 = (\frac{X_M}{X_s}V_s I_r)^2 \tag{8.3}$$

From (8.3), the P/Q operation region of DFIG under different wind speeds is plotted as shown in Fig. 8.1. The main factors for the P/Q region of DFIG are slip, rotor current and stator voltage. As the rotor speed increases, the region becomes larger. According to the lower control loop of RSC, as wind speed increases, i_{qr} increases due to the increased electromagnetic power. However, i_{dr} keeps constant because of the flux control as shown in Fig. 6.1. Hence, the rotor current angle θ will increase. In addition, Q_t will decrease according to the above expression of Q_t. The values of P_t and Q_t are marked in points A, B and C under different wind speeds as shown in Fig. 8.1

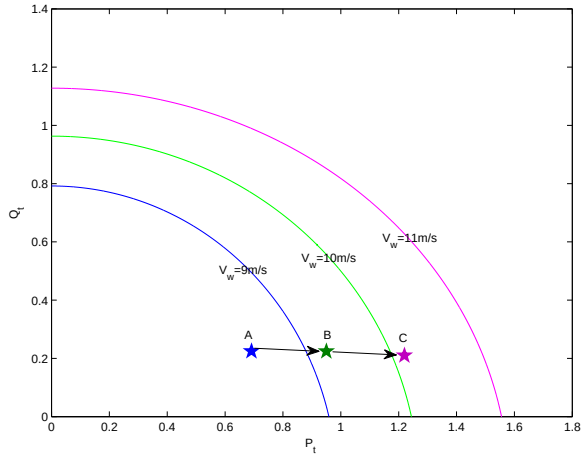

Figure 8.1. P Q limit and operating points of the DFIG under different wind speeds.

8.2 Limits of the Rectifier AC Voltage

8.2.1 Lower Limit of the Rectifier AC Voltage

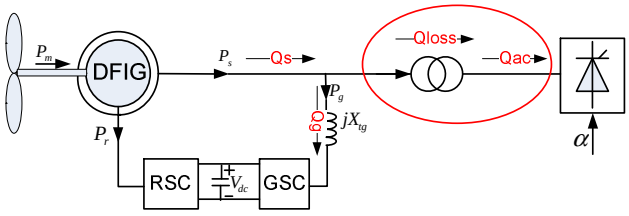

Figure 8.2. Reactive power flow.

If we simplify the red circled part of Fig. 8.2 as a radial system as shown in Fig. 8.3, where $\bar{V_s} = V_s \angle \delta$, $\bar{V_{ac}} = V_{ac} \angle 0$, then for the simplified radial system, the total active and reactive power from DFIG at the receiving end are expressed as follows:

$$P_t = \frac{V_s V_{ac}}{X_L} sin(\delta) \tag{8.4}$$

$$Q_t = \frac{V_s^2 - V_S V_{ac} cos(\delta)}{X_L} \tag{8.5}$$

Here, if we keep the stator voltage $V_s = 1$, then the relation of the total active and reactive power is obtained as:

$$P_t^2 + (Q_t - \frac{1}{X_L})^2 = (\frac{V_{ac}}{X_L})^2 \tag{8.6}$$

This above relation is expressed as a circle, which is the total operation curve of DFIG. The location of the operation curve depends on the ac bus voltage V_{ac}. Increased V_{ac} means larger radius.

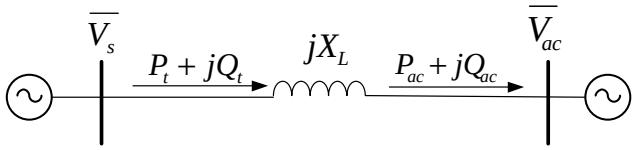

Figure 8.3. Simplified radial system.

Moreover, the MVA limit of the induction generator is fixed. Here, we consider it as 1pu. The feasible region of DFIG is defined as 125% of the induction generator rating, which means that $P_t^2 + Q_t^2 \leq 1.25^2$. Considering this limit, the actual operation curve of DFIG is only the part within the limit circle. Since the ac bus voltage is the only factor that affects the radius, if V_{ac} decreases, the radius decreases, too. Operation curves of DFIG under two different values of ac bus voltage V_{ac} are shown in Fig. 8.4. When $V_{ac} = 0.85$, there is no overlapping between the operation curve and the limit curve. DFIG is already out of its MVA limit. When $V_{ac} = 0.95$, only the overlapped thick part is the actual operating curve. Therefore, to ensure normal operation, V_{ac} has a lower limit 0.875.

8.2.2 Upper Limit of the Rectifier AC Voltage

For LCC-HVDC, the thyristor-based converter needs to consume reactive power to ensure its normal operation. First, because of the firing angle, the current delays the voltage, which means that reactive power will be absorbed by the converter. Furthermore, the commutation resistance also needs reactive power. For our studied system as shown in

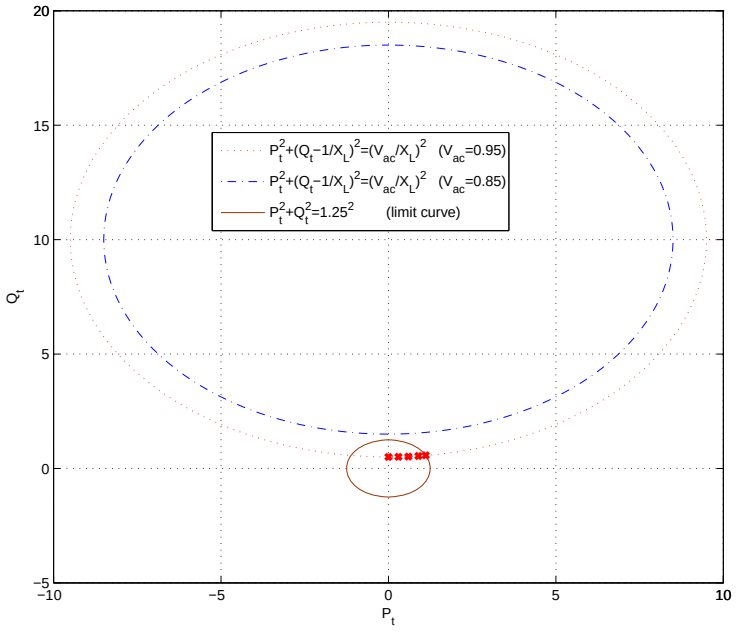

Figure 8.4. Operation region of DFIG.

Fig. 8.2, in order to provide reactive power for LCC-HVDC, $Q_s - Q_g - Q_{loss}$ should be at least larger than 0.

For the simplified radial system, the active and reactive powers at the receiving end are expressed as follows:

$$P_{ac} = \frac{V_s V_{ac}}{X_L} sin(\delta) \tag{8.7}$$

$$Q_{ac} = \frac{V_s V_{ac} cos(\delta)}{X_L} - \frac{V_{ac}^2}{X_L} = \frac{V_{ac}(V_s cos(\delta) - V_{ac})}{X_L} \tag{8.8}$$

To make sure $Q_{ac} > 0$, V_{ac} should be in the range: $0 < V_{ac} < V_s cos(\delta)$. Here, we keep the stator voltage to 1pu, then the terminal voltage V_{ac} should satisfy:

$$V_{ac} < cos(\delta) \tag{8.9}$$

Combined with (8.7), which is the same as (8.4), then (8.9) can be expressed as follows:

$$V_{ac} < \sqrt{1 - (\frac{P_t X_L}{V_{ac}})^2} \tag{8.10}$$

The specific region of V_{ac} related with the active power P_t is shown in Fig. 8.5. As mentioned before, there is an operation limit of DFIG, $\sqrt{P_t^2 + Q_t^2} < 1.25$, where P_t is the total active power and Q_t is the total reactive power. Hence, the active power P_t should be less than 1.25, which is shown as the red curve in Fig. 8.5. Therefore, the exact region of terminal voltage is found as $V_{ac} < 0.992$.

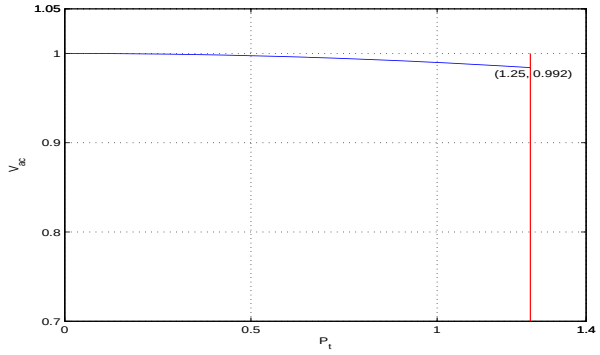

Figure 8.5. Operation region of the ac bus voltage.

As analyzed in above section, there is a lower limit of V_{ac}, therefore the final range of V_{ac} is $0.875 < V_{ac} < 0.992$ to ensure normal operation of the system. Case studies in following section will verify the exact region of the ac bus voltage V_{ac}.

8.3 Case Studies

Simulation studies with the proposed control design are carried out by Matlab/Simulink for an integrated 200 MW wind farm based on DFIG with an HVDC-link. The parameters of the DFIG and HVDC-link are given in Table 8.1 and Table 8.2.

Table 8.1. Parameters of the DFIG

r_s (pu)	0.00488
r_r (pu)	0.00549
X_{ls} (pu)	0.09231
X_{lr} (pu)	0.09955
X_M (pu)	3.95279
H $(kg.m^2)$	3.5

Table 8.2. Parameters of the network and simulated HVDC-link

X_L (inductance of the transformer)	j0.1(pu)
R (dc transmission line resistance)	0.3595(pu)
V_{di} (simplified receiving end of HVDC-link)	-1.64(pu)

8.3.1 Case 1: System Dynamics if V_{ac} is Out of the Range

As analyzed, in order to ensure the reactive power coordination between DFIG and LCC-HVDC, which means that the DFIG can always provide reactive power for the LCC-HVDC while the DFIG works in its operation limit, there is an operating region of the ac bus voltage. First, if V_{ac} is set as 0.87, a value lower than its lower limit, the active power, reactive power, and the apparent power at the ac bus are monitored under different wind speeds as shown in Fig. 8.6. The wind speed increases from 9m/s to 10m/s at 10s, and increases from 10m/s to 11m/s at 25s. As the wind speed increases, the active power delivery to the HVDC increases, too. In addition, the reactive power supplied to HVDC decreases. However, the total apparent power is already out of the limit of DFIG.

If the ac bus voltage V_{ac} is set out of its upper limit, as the wind speed increases, the reactive power supply to HVDC may be less than 0 as discussed in the previous section. When the ac bus voltage V_{ac} is set as 0.993, the dynamic responses of the active power, reactive power, and the apparent power at the ac bus are plotted in Fig. 8.7 under different wind speeds. As the wind speed increases to 11m/s at 25s, the reactive power supply to HVDC is already less than zero, so then the whole system will not work.

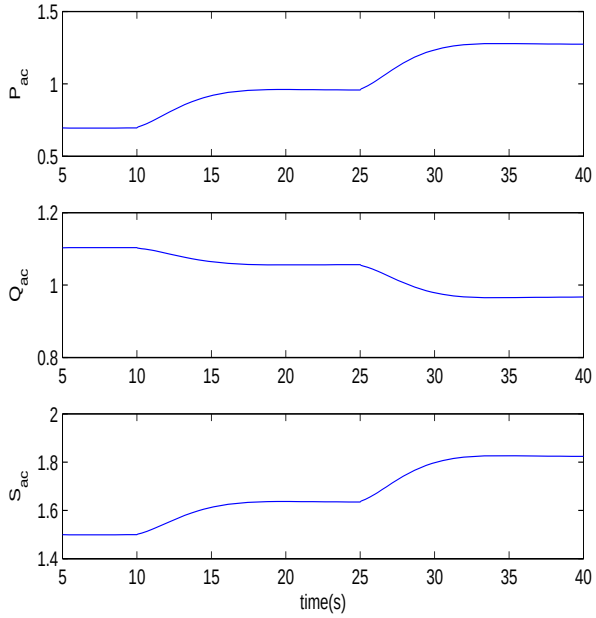

Figure 8.6. Dynamic responses of active power, reactive power, and apparent power at the ac bus under wind speed changes when $V_{ac} = 0.87$.

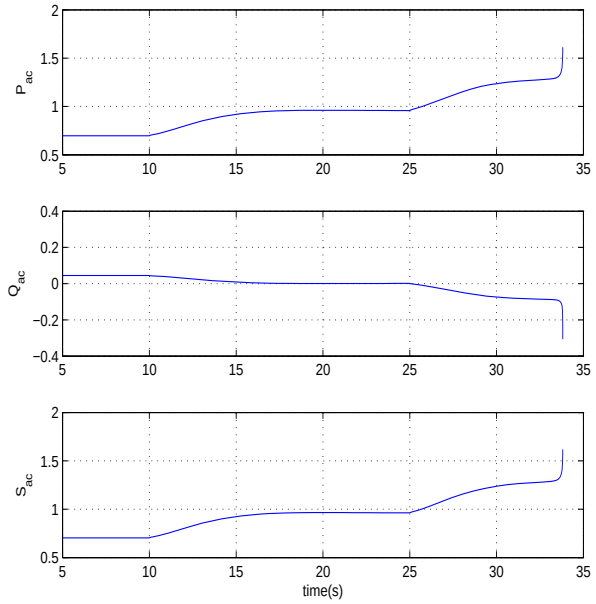

Figure 8.7. Dynamic responses of active power, reactive power, and apparent power at the ac bus under wind speed changes when $V_{ac} = 0.993$.

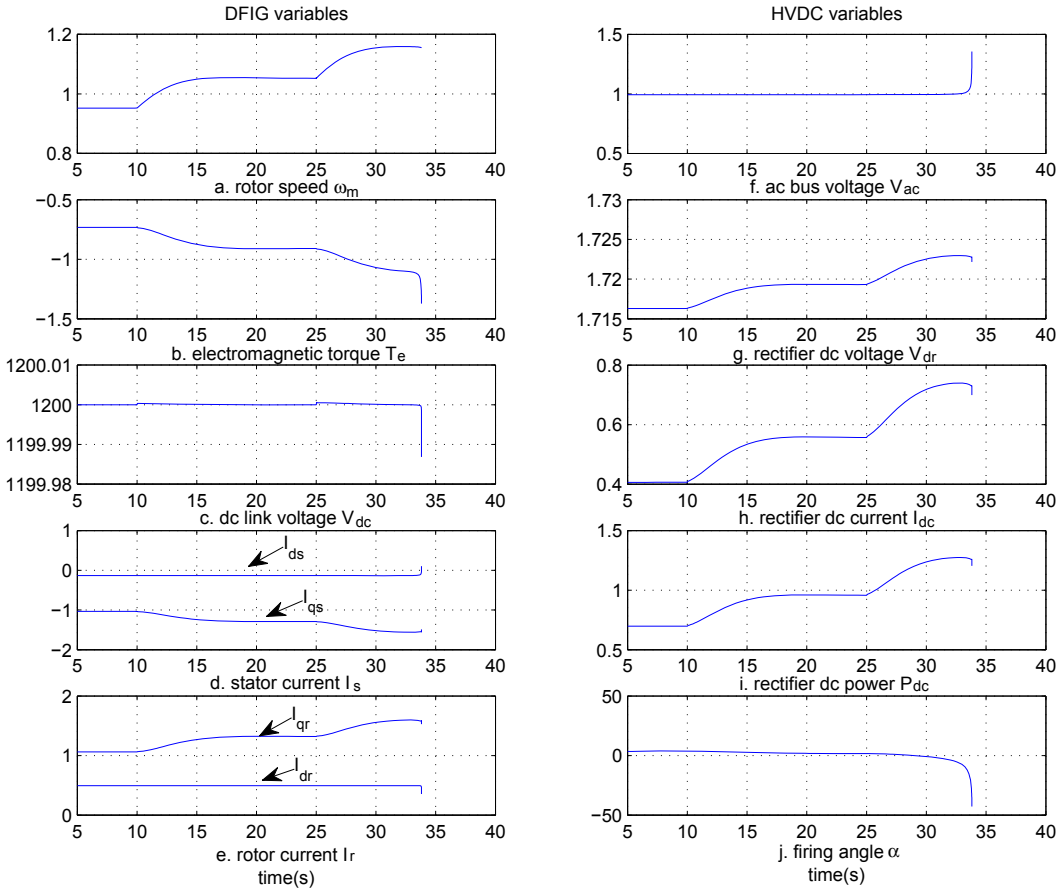

Figure 8.8. Dynamic responses of DFIG and HVDC variables, wind speed increases from 9m/s to 10m/s at 10s, and increases from 10m/s to 11m/s at 25s, when $V_{ac} = 0.993$.

8.3.2 Case 2: System Dynamics if V_{ac} is In the Range

To obtain normal operation of the studied system, the ac bus voltage should be higher than 0.875 to ensure the DFIG will not be out of its operating limit. In addition, the ac bus voltage should also have an upper limit of 0.992 to make sure that the reactive power supply to HVDC is larger than 0. In this case, the ac bus voltage V_{ac} is set within the range of 0.875-0.992. When $V_{ac} = 0.98$, Fig. 8.9 shows the dynamic responses of the active power, reactive power and total apparent power. The wind speed increases from 9m/s to 10m/s at 10s, and increases from 10m/s to 11m/s at 25s. The reactive power provided for HVDC is larger than 0 as wind speed increases.

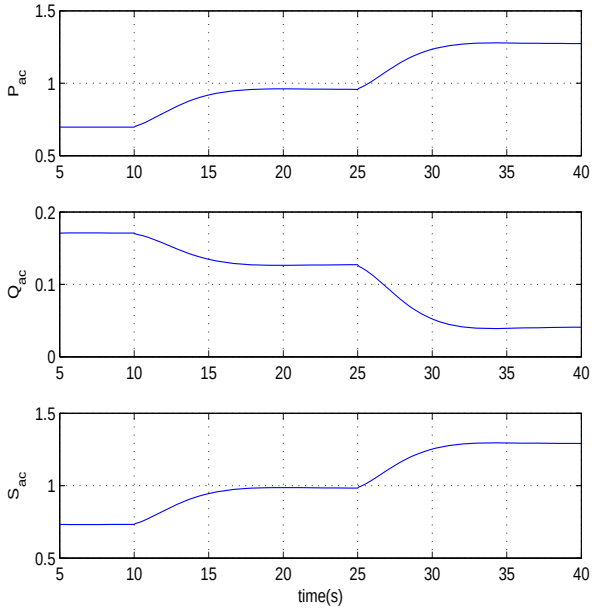

Figure 8.9. Dynamic responses of active power, reactive power, and apparent power at the ac bus under wind speed changes when $V_{ac} = 0.98$.

Dynamic responses of DFIG and HVDC variables are also plotted in Fig. 8.10. The rotor speed and electromagnetic torque increase due to increased wind speed. The dc voltage of dc-link between RSC and GSC keeps constant due to GSC control loop. The firing angle α of rectifier decreases, while the ac bus voltage keeps constant, consequently,

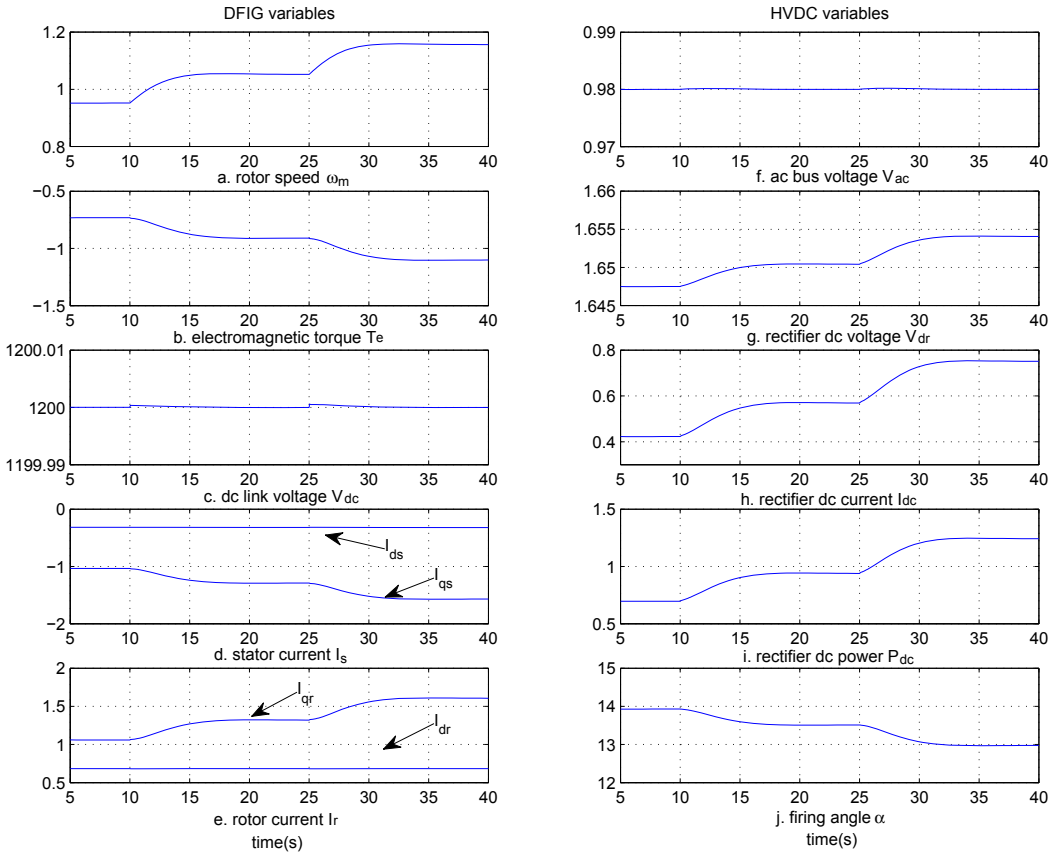

Figure 8.10. Dynamic responses of DFIG and HVDC variables, wind speed increases from 9m/s to 10m/s at 10s, and increases from 10m/s to 11m/s at 25s, when $V_{ac} = 0.98$.

the dc voltage V_{dr} of rectifier increases. Also, the dc power P_{dc} increases to keep the power balance.

CHAPTER 9

CONCLUSIONS AND FUTURE WORK

9.1 Conclusions

This dissertation contains five main parts.

First, modeling and control of DFIG-based wind energy with its HVDC delivery system are presented in Chapters 3 and 4. Modeling of the DFIG-based wind farm and LCC-HVDC are described in Chapter 3, including an average model and a detailed model built in Matlab/Simulink and Matlab/SimPowerSystems. Moreover, control strategies for both RSC and GSC are considered in Chapter 4. The design procedures of the PI controllers are also given. Basic control principles of HVDC are discussed.

The second part talks about FRT of an ac connected DFIG-based wind farm. Unbalanced grid conditions will cause current harmonics, torque pulsation, power oscillation, etc. A coordinated control technique with a simplified structure is proposed in Chapter 5. The RSC is controlled to suppress the torque ripple while a simple control technique considering the rotor power effect is proposed for GSC to suppress the dc link voltage fluctuation.

Active power balance is studied as the third part in Chapter 6. Based on modified control of DFIG, a coordinated control scheme is proposed for LCC-HVDC. The power delivered through HVDC follows the change of the wind power under different wind speeds. Test cases in Matlab/Simulink and Matlab/SimPowerSystems validate the effectiveness of the proposed control method.

The fourth part investigates the fast power routing capability of LCC-HVDC. A positive feedback control loop is introduced in the rectifier control to produce the dc current order. Matlab/SimPowersystems based simulation for an ac/dc system with wind power

penetration confirms the effectiveness of such a control scheme. In addition, ac fault recovery is investigated for an LCC-HVDC equipped with the proposed control scheme. The proposed technology can help realize fast power routing through LCC-HVDC in future grids with high penetrations of intermittent renewable energy resources.

The fifth part considers reactive power coordination between the DFIG-based wind farm and LCC-HVDC. When the wind farm is connected to LCC-HVDC, reactive power compensation needs to be provided. Reactive power characteristic of DFIG is presented in Chapter 8. Furthermore, the limiting range of the ac bus voltage is investigated since reactive power is closely related to voltage level. Simulation studies in Matlab/Simulink verify the analysis.

9.2 Future Work

The future work of this dissertation consists of the following parts.

First, dynamic analysis of the wind farm with HVDC delivery system will be done in the future. As described in Chapter 2, small signal analysis of wind farms have been used in [51, 56]. The contribution of this dissertation will be improved if eigenvalue analysis is considered.

Second, the reactive power coordination between the wind farm and LCC-HVDC will be verified based on the detailed system model built in Matlab/SimPowerSystems. A detailed system model will provide quantitative information of the reactive power from DFIG and the filters. Hence, the analysis of reactive power coordination in Chapter 8 will be validated further.

Last, the FRT of the wind farm with HVDC delivery will be studied. Control strategies for the HVDC under different fault types and fault locations will be proposed. Therefore, the dynamic responses of the whole system will be greatly improved.

REFERENCES

[1] "HVDC transmission for lower investment cost," ABB, Tech. Rep.

[2] P. Kundur, *Power System Stability and Control*. McGraw Hill, 1994.

[3] Wind force 12,. European Wind Energy Association. [Online]. Available: http://www.ewea.org

[4] "U.S. wind industry year-end 2010 market report," U.S. Department of Energy, Tech. Rep.

[5] "20% wind energy by 2030: Increasing wind energy's contribution to U.S. electricity supply," U.S. department of energy, Tech. Rep. [Online]. Available: http://www1.eere.energy.gov/windandhydro/pdfs/41869.pdf

[6] T. Bookman, "Wind energy's promise, offshore," *Technology and Society Magazine, IEEE*, vol. 24, no. 2, pp. 9–15, 2005.

[7] T. Ackermann, "Transmission systems for offshore wind farms," *Power Engineering Review, IEEE*, vol. 22, no. 12, pp. 23–27, 2002.

[8] "Thanet offshore wind farm," VATTENFALL, Tech. Rep. [Online]. Available: http://www.vattenfall.co.uk/en/thanet-offshore-wind-farm.htm

[9] S. Muller, M. Deicke, and R. De Doncker, "Doubly fed induction generator systems for wind turbines," *Industry Applications Magazine, IEEE*, vol. 8, no. 3, pp. 26–33, May/Jun. 2002.

[10] L. Xu, "Enhanced control and operation of DFIG-based wind farms during network unbalance," *Energy Conversion, IEEE Transactions on*, vol. 23, no. 4, pp. 1073–1081, Dec. 2008.

[11] L. Fan, S. Yuvarajan, and R. Kavasseri, "Harmonic analysis of a doubly fed induction generator," in *Transmission and Distribution Conference and Exposition, 2010 IEEE PES*, Apr. 2010, p. 1.

[12] Y. Zhou, P. Bauer, J. Ferreira, and J. Pierik, "Operation of grid-connected DFIG under unbalanced grid voltage condition," *Energy Conversion, IEEE Transactions on*, vol. 24, no. 1, pp. 240–246, Mar. 2009.

[13] L. Xu and B. R.Andersen, "Grid connection of large offshore wind farms using HVDC," *Wind Energy*, vol. 9, no. 4, pp. 371–382, Dec. 2005.

[14] S. Bozhko, R. Blasco-Gimenez, R. Li, J. Clare, and G. Asher, "Control of offshore DFIG-based wind farm grid with line-commutated HVDC connection," *Energy Conversion, IEEE Transactions on*, vol. 22, no. 1, pp. 71–78, 2007.

[15] V. K. Sood, *HVDC and FACTS Controllers:Applications of Static Converters in Power Systems*. Springer, 2004.

[16] R. Li, S. Bozhko, and G. Asher, "Frequency control design for offshore wind farm grid with LCC-HVDC link connection," *Power Electronics, IEEE Transactions on*, vol. 23, no. 3, pp. 1085–1092, May 2008.

[17] L. Xu, L. Yao, and C. Sasse, "Grid integration of large DFIG-based wind farms using VSC transmission," *Power Systems, IEEE Transactions on*, vol. 22, no. 3, pp. 976–984, 2007.

[18] T. Vrionis, X. Koutiva, N. Vovos, and G. Giannakopoulos, "Control of an HVdc link connecting a wind farm to the grid for fault ride-through enhancement," *Power Systems, IEEE Transactions on*, vol. 22, no. 4, pp. 2039–2047, 2007.

[19] J. Morren and S. de Haan, "Ridethrough of wind turbines with doubly-fed induction generator during a voltage dip," *Energy Conversion, IEEE Transactions on*, vol. 20, no. 2, pp. 435–441, Jun. 2005.

[20] T. Ackermann, *Wind Power in Power Systems*. Wiley, 2005.

[21] M. Mohseni, S. Islam, and M. Masoum, "Enhanced hysteresis-based current regulators in vector control of DFIG wind turbines," *Power Electronics, IEEE Transactions on*, vol. 26, no. 1, pp. 223–234, Jan. 2011.

[22] L. Xu and P. Cartwright, "Direct active and reactive power control of DFIG for wind energy generation," *Energy Conversion, IEEE Transactions on*, vol. 21, no. 3, pp. 750–758, Sept. 2006.

[23] R. Pena, J. Clare, and G. Asher, "Doubly fed induction generator using back-to-back PWM converters and its application to variable-speed wind-energy generation," *Electric Power Applications, IEE Proceedings* -, vol. 143, no. 3, pp. 231–241, May 1996.

[24] M. Tazil, V. Kumar, R. Bansal, S. Kong, Z. Dong, W. Freitas, and H. Mathur, "Three-phase doubly fed induction generators: an overview," *Electric Power Applications, IET*, vol. 4, no. 2, pp. 75–89, Feb. 2010.

[25] Y. Lei, A. Mullane, G. Lightbody, and R. Yacamini, "Modeling of the wind turbine with a doubly fed induction generator for grid integration studies," *IEEE Trans. Energy Convers.*, vol. 21, pp. 257–264, Mar. 2006.

[26] J. B. Ekanayake, L. Holdsworth, X. Wu, and N. Jenkins, "Dynamic modeling of doubly fed induction generator wind turbines," *IEEE Trans. Power Syst.*, vol. 18, pp. 803–809, Nov. 2003.

[27] S. Chondrogiannis and M. Barnes, "Stability of doubly-fed induction generator under stator voltage orientated vector control," *Renewable Power Generation, IET*, vol. 2, no. 3, pp. 170–180, Sept. 2008.

[28] L. Xu, D. Zhi, and B. Williams, "Predictive current control of doubly fed induction generators," *Industrial Electronics, IEEE Transactions on*, vol. 56, no. 10, pp. 4143–4153, Oct. 2009.

[29] E. Muljadi, T. Batan, D. Yildirim, and C. Butterfield, "Understanding the unbalanced voltage problem in wind turbine generation," in *Proc. Ind. Appl. Conf.*, vol. 2, 1999, pp. 1359–1365.

[30] T. Brekken and N. Mohan, "Control of a doubly fed induction wind generator under unbalanced grid voltage conditions," *Energy Conversion, IEEE Transactions on*, vol. 22, no. 1, pp. 129–135, Mar. 2007.

[31] L. Xu and Y. Wang, "Dynamic modeling and control of DFIG-based wind turbines under unbalanced network conditions," *Power Systems, IEEE Transactions on*, vol. 22, no. 1, pp. 314–323, Feb. 2007.

[32] R. Pena, R. Cardenas, and E. Escobar, "Control system for unbalanced operation of stand-alone doubly fed induction generators," *IEEE Trans. Energy Convers.*, vol. 22, no. 2, pp. 544–545, Jun. 2007.

[33] L. Xu, "Coordinated control of DFIG's rotor and grid side converters during network unbalance," *Power Electronics, IEEE Transactions on*, vol. 23, no. 3, pp. 1041–1049, May 2008.

[34] O. Gomis-Bellmunt, A. Junyent-Ferre, A. Sumper, and J. Bergas-Jan, "Ride-through control of a doubly fed induction generator under unbalanced voltage sags," *Energy Conversion, IEEE Transactions on*, vol. 23, no. 4, pp. 1036–1045, Dec. 2008.

[35] J. Hu and Y. He, "Modeling and control of grid-connected voltage-sourced converters under generalized unbalanced operation conditions," *Energy Conversion, IEEE Transactions on*, vol. 23, no. 3, pp. 903–913, Sept. 2008.

[36] D. Santos-Martin, J. Rodriguez-Amenedo, and S. Arnalte, "Direct power control applied to doubly fed induction generator under unbalanced grid voltage conditions," *Power Electronics, IEEE Transactions on*, vol. 23, no. 5, pp. 2328–2336, Sept. 2008.

[37] D. Santos-Martin, J. Rodriguez-Amenedo, and S. Arnaltes, "Providing ride-through capability to a doubly fed induction generator under unbalanced voltage dips," *Power Electronics, IEEE Transactions on*, vol. 24, no. 7, pp. 1747–1757, Jul. 2009.

[38] "Modeling of ge wind turbine-generators for grid studies," General Electric International, Inc, Schenectady, New York, Tech. Rep., Mar. 2005.

[39] K. Meah and S. Ula, "Comparative evaluation of HVDC and HVAC transmission systems," in *Power Engineering Society General Meeting, 2007. IEEE*, Jun. 2007, pp. 1–5.

[40] P. Bresesti, W. Kling, R. Hendriks, and R. Vailati, "HVDC connection of offshore wind farms to the transmission system," *Energy Conversion, IEEE Transactions on*, vol. 22, no. 1, pp. 37–43, 2007.

[41] B. Andersen, L. Xu, and K. Wong, "Topologies for VSC transmission," in *AC-DC Power Transmission, 2001. Seventh International Conference on (Conf. Publ. No. 485)*, 2001, pp. 298–304.

[42] N. Flourentzou, V. Agelidis, and G. Demetriades, "VSC-based HVDC power transmission systems: an overview," *Power Electronics, IEEE Transactions on*, vol. 24, no. 3, pp. 592–602, Mar. 2009.

[43] X. Koutiva, T. Vrionis, N. Vovos, and G. Giannakopoulos, "Optimal integration of an offshore wind farm to a weak AC grid," *Power Delivery, IEEE Transactions on*, vol. 21, no. 2, pp. 987–994, Apr. 2006.

[44] L. Zhang, L. Harnefors, and H.-P. Nee, "Interconnection of two very weak AC systems by VSC-HVDC links using power-synchronization control," *Power Systems, IEEE Transactions on*, vol. 26, no. 1, pp. 344–355, 2011.

[45] M. Joorabian, S. Seysossadat, and M. Zamani, "An algorithm to design harmonic filters based on power factor correction for HVDC systems," in *Industrial Technology, 2006. ICIT 2006. IEEE International Conference on*, 2006, pp. 2978–2983.

[46] P. Li and Q. Hao, "The algorithm for the parameters of AC filters in HVDC transmission system," in *Transmission and Distribution Conference and Exposition, 2008.D. IEEE/PES*, Apr. 2008, pp. 1–6.

[47] M. Zamani, M. Moghaddasian, M. Joorabian, S. Seifossadat, and A. Yazdani, "C-type filter design based on power-factor correction for 12-pulse HVDC converters," in *Industrial Electronics, 2008. IECON 2008. 34th Annual Conference of IEEE*, 2008, pp. 3039–3044.

[48] Y. Xiao, J. Zhao, and S. Mao, "Theory for the design of C-type filter," in *Harmonics and Quality of Power, 2004. 11th International Conference on*, 2004, pp. 11–15.

[49] D. Xiang, L. Ran, J. Bumby, P. Tavner, and S. Yang, "Coordinated control of an HVDC link and doubly fed induction generators in a large offshore wind farm," *Power Delivery, IEEE Transactions on*, vol. 21, no. 1, pp. 463–471, 2006.

[50] S. Bozhko, G. Asher, R. Li, J. Clare, and L. Yao, "Large offshore DFIG-based wind farm with line-commutated HVDC connection to the main grid: Engineering studies," *Energy Conversion, IEEE Transactions on*, vol. 23, no. 1, pp. 119–127, Mar. 2008.

[51] H. Zhou, G. Yang, and J. Wang, "Modeling, analysis, and control for the rectifier of hybrid HVdc systems for DFIG-based wind farms," *Energy Conversion, IEEE Transactions on*, vol. 26, no. 1, pp. 340–353, Mar. 2011.

[52] D. Santos-Martina, S. Arnaltesb, and J. R. Amenedob, "Reactive power capability of doubly fed asynchronous generators," *Electric Power Systems Research*, vol. 78, no. 11, pp. 1837–1840, Nov. 2008.

[53] T. Lund, P. Sorensen, and J. Eek, "Reactive power capability of a wind turbine with doubly fed induction generator," *Wind Energy*, vol. 10, pp. 379–394, Apr. 2007.

[54] S. Engelhardt, I. Erlich, C. Feltes, J. Kretschmann, and F. Shewarega, "Reactive power capability of wind turbines based on doubly fed induction generators," *Energy Conversion, IEEE Transactions on*, 2010.

[55] M. Montilla-DJesus, D. Santos-Martin, S. Arnaltes, and E. Castronuovo, "Optimal operation of offshore wind farms with line-commutated HVDC link connection," *Energy Conversion, IEEE Transactions on*, vol. 25, no. 2, pp. 504–513, 2010.

[56] L. Wang, K.-H. Wang, W.-J. Lee, and Z. Chen, "Power-flow control and stability enhancement of four parallel-operated offshore wind farms using a line-commutated HVDC link," *Power Delivery, IEEE Transactions on*, vol. 25, no. 2, pp. 1190–1202, Apr. 2010.

[57] S. Muyeen, M. Ali, R. Takahashi, T. Murata, J. Tamura, Y. Tomaki, A. Sakahara, and E. Sasano, "Transient stability analysis of wind generator system with the consideration of multi-mass shaft model," in *Power Electronics and Drives Systems, 2005. PEDS 2005. International Conference on*, vol. 1, 2005, pp. 511–516.

[58] P. Krause, *Analysis of Electric Machinery*. New York: McGraw-Hill, 1986.

[59] E. Uhlmann, *Power Transmission by Direct Current*. Springer-Verlag Berlin Heidelberg New York, 1975.

[60] E. W. Kimbark, *Direct Current Transmission*. Wiley-interscience, 1971.

[61] J. Arrillaga, *High Voltage Direct Current Transmission*. Institution of Engineering and Technology (IET), 1998.

[62] N. Rostamkolai, C. Wegner, R. Piwko, H. Elahi, M. Eitzmann, G. Garzi, and P. Tietz, "Control design of santo tome back-to-back HVDC link," *Power Systems, IEEE Transactions on*, vol. 8, no. 3, pp. 1250–1256, Aug. 1993.

[63] G.-C. Hsieh and J. Hung, "Phase-locked loop techniques. a survey," *Industrial Electronics, IEEE Transactions on*, vol. 43, no. 6, pp. 609–615, Dec. 1996.

[64] S.-K. Chung, "Phase-locked loop for grid-connected three-phase power conversion systems," *Electric Power Applications, IEE Proceedings* -, vol. 147, no. 3, pp. 213–219, May 2000.

[65] ——, "A phase tracking system for three phase utility interface inverters," *Power Electronics, IEEE Transactions on*, vol. 15, no. 3, pp. 431–438, May 2000.

[66] V. Kaura and V. Blasko, "Operation of a phase locked loop system under distorted utility conditions," *Industry Applications, IEEE Transactions on*, vol. 33, no. 1, pp. 58–63, Jan./Feb. 1997.

[67] L. Rolim, D. da Costa, and M. Aredes, "Analysis and software implementation of a robust synchronizing PLL circuit based on the pq theory," *Industrial Electronics, IEEE Transactions on*, vol. 53, no. 6, pp. 1919–1926, Dec. 2006.

[68] J. Svensson, "Synchronisation methods for grid-connected voltage source converters," *Generation, Transmission and Distribution, IEE Proceedings-*, vol. 148, no. 3, pp. 229–235, May 2001.

[69] A. Yazdani and R. Iravani, *Voltage-Sourced Converters in Power Systems*. Wiley, 2010.

[70] A. Ostadi, A. Yazdani, and R. Varma, "Modeling and stability analysis of a DFIG-based wind-power generator interfaced with a series-compensated line," *Power Delivery, IEEE Transactions on*, vol. 24, no. 3, pp. 1504–1514, Jul. 2009.

[71] R. Pena, J. Clare, and G. Asher, "Doubly fed induction generator using back-to-back pwm converters and its application to variable-speed wind-energy generation," *Electric Power Applications, IEE Proceedings* -, vol. 143, no. 3, pp. 231–241, May 1996.

[72] J. Yao, H. Li, Y. Liao, and Z. Chen, "An improved control strategy of limiting the DC-link voltage fluctuation for a doubly fed induction wind generator," *Power Electronics, IEEE Transactions on*, vol. 23, no. 3, pp. 1205–1213, May 2008.

[73] J. Hu and Y. He, "Modeling and enhanced control of DFIG under unbalanced grid voltage conditions," *Electric Power System Research*, vol. 79, no. 2, pp. 273–281, 2008.

[74] J. Hu, Y. He, L. Xu, and B. Williams, "Improved control of dfig systems during network unbalance using PI-R current regulators," *Industrial Electronics, IEEE Transactions on*, vol. 56, no. 2, pp. 439–451, Feb. 2009.

[75] J. Lopez, E. Gubia, P. Sanchis, X. Roboam, and L. Marroyo, "Wind turbines based on doubly fed induction generator under asymmetrical voltage dips," *Energy Conversion, IEEE Transactions on*, vol. 23, no. 1, pp. 321–330, Mar. 2008.

[76] L. Fan, S. Yuvarajan, and R. Kavasseri, "Harmonic analysis of a DFIG for a wind energy conversion system," *Energy Conversion, IEEE Transactions on*, vol. 25, no. 1, pp. 181–190, Mar. 2010.

[77] X. Wu, S. Panda, and J. Xu, "Analysis of the instantaneous power flow for three-phase pwm boost rectifier under unbalanced supply voltage conditions," *Power Electronics, IEEE Transactions on*, vol. 23, no. 4, pp. 1679–1691, Jul. 2008.

[78] R. Teodorescu, F. Blaabjerg, M. Liserre, and P. Loh, "Proportional-resonant controllers and filters for grid-connected voltage-source converters," *Electric Power Applications, IEE Proceedings* -, vol. 153, no. 5, pp. 750–762, Sept. 2006.

[79] L. Fan, R. Kavasseri, H. Yin, C. Zhu, and M. Hu, "Control of DFIG for rotor current harmonics elimination," in *Power Energy Society General Meeting, 2009. PES '09. IEEE*, Jul. 2009, pp. 1–7.

[80] S. Foster, L. Xu, and B. Fox, "Control of an lcc hvdc system for connecting large offshore wind farms with special consideration of grid fault," in *Power and Energy Society General Meeting - Conversion and Delivery of Electrical Energy in the 21st Century, 2008 IEEE*, Jul. 2008, pp. 1–8.

[81] Simpowersystems^{TM}. Mathworks. [Online]. Available: http://www.mathworks.com/help/toolbox/physmod/powersys/powersys_product_page.html

[82] Simpowersystems^{TM}- hydraulic turbine and governor. Mathworks. [Online]. Available: http://www.mathworks.com/help/toolbox/physmod/powersys/ref/hydraulicturbineandgovernor.html

[83] PID tutorial. The University of Michigan. [Online]. Available: http://www.engin.umich.edu/group/ctm/PID/PID.html#introduction

[84] H. Yin and L. Fan, "Modeling and control of DFIG-based large offshore wind farm with HVDC-link integration," in *North American Power Symposium (NAPS)*, 2009.

ABOUT THE AUTHOR

Haiping Yin was born in 1982 in Jiangsu, China. She obtained her Bachelor and Master degrees in Electrical Engineering from Nanjing Normal University, Nanjing China in 2005 and 2008. She received her Ph.D. degree in Electrical Engineering from the University of South Florida in December, 2011. Her research area is modeling and control of wind energy systems and electrical power systems.